

HYDROCARBON MICROSEEPAGE MAPPING VIA REMOTE SENSING FOR  
GEMRIK ANTICLINE, BOZOVA OIL FIELD, ADIYAMAN, TURKEY

A THESIS SUBMITTED TO  
THE GRADUATE SCHOOL OF NATURAL AND APPLIED SCIENCES  
OF  
MIDDLE EAST TECHNICAL UNIVERSITY

BY

EMRE AVCIOĞLU

IN PARTIAL FULFILLMENT OF THE REQUIREMENTS  
FOR  
THE DEGREE OF MASTER OF SCIENCE  
IN  
GEODETIC AND GEOGRAPHIC INFORMATION TECHNOLOGIES

SEPTEMBER 2010

Approval of the thesis:

**HYDROCARBON MICROSEEPAGE MAPPING VIA REMOTE SENSING  
FOR GEMRIK ANTICLINE, BOZOVA OIL FIELD, ADIYAMAN, TURKEY**

submitted by **EMRE AVCIOĞLU** in partial fulfillment of the requirements for the degree of **Master of Science in Geodetic and Geographic Information Technologies Department, Middle East Technical University** by,

Prof. Dr. Canan Özgen  
Dean, Graduate School of **Natural and Applied Sciences**

Assoc. Prof. Mahmut Onur Karşlıođlu  
Head of Department, **Civil Engineering**

Assoc. Prof. Dr. H. Şebnem Düzgün  
Supervisor, **Mining Engineering Dept., METU**

Prof. Dr. G. M. Vedat Toprak  
Co-Supervisor, **Geological Engineering Dept., METU**

**Examining Committee Members:**

Assoc. Prof. Dr. Zuhâl Akyürek  
Civil Engineering Dept., METU

Assoc. Prof. Dr. H. Şebnem Düzgün  
Mining Engineering Dept., METU

Prof. Dr. G. M. Vedat Toprak  
Geological Engineering Dept., METU

Dr. Erhan Gökçay  
Computer Engineering Dept., Atılım University

Dr. Erdem Yetkin  
Consultant

**Date:** 17.09.2010

**I hereby declare that all information in this document has been obtained and presented in accordance with academic rules and ethical conduct. I also declare that, as required by these rules and conduct, I have fully cited and referenced all material and results that are not original to this work.**

Name, Last name : Emre AVCIOĞLU

Signature :

## **ABSTRACT**

### **HYDROCARBON MICROSEEPAGE MAPPING VIA REMOTE SENSING FOR GEMRIK ANTICLINE, BOZOVA OIL FIELD, ADIYAMAN, TURKEY**

Avcıođlu, Emre

M.Sc., Department of Geodetic and Geographic Information Technologies

Supervisor: Assoc. Prof. Dr. H. Őebnem Düzgün

Co-Supervisor: Prof. Dr. G. M. Vedat Toprak

September 2010, 116 pages

Hydrocarbon (HC) microseepages can be indicator of possible reservoirs. For that reason, mapping the microseepages has potential to be used in petroleum exploration. This study presents a methodology for mapping HC microseepages and related clay mineral alteration in Gemrik Anticline, Adiyaman. For this purpose samples were collected from the potential seepage zones and tested by geochemical analysis. All samples were found to contain some HC. Then, an ASTER image of the region was obtained and a band combination was generated to map this particular region. To map related clay mineral alteration, firstly reflectance spectra of samples were measured using field spectrometer. Secondly, spectrally-known samples were analyzed in USGS Library to determine the reflectance spectra of the constitutional clay minerals in the samples. Lastly, the reflectance characteristics of selected end

members were represented as ASTER band combinations based on their spectral absorption characteristics and literature information. Crosta Technique was used to determine required principal components to map HC microseepage and related clay mineral alteration. Then, this methodology is applied to the whole ASTER image. Ground truth study showed that more than 65% of the revisited anomalies show similar prospects to that of the referenced anticline regardless of their geochemical content. In order to certify the ASTER band combination for mapping HC microseepages, anomalous and non-anomalous pixels were selected from the resultant HC map and given as training data samples to AdaBoost loop which is an image processing algorithm. It has been found that ASTER band combination offered for mapping HC microseepages is similar to that of AdaBoost Algorithm output.

Keywords: Remote sensing, geology, hydrocarbon, microseepages, AdaBoost, crosta, Bozova, Adiyaman, Turkey

## ÖZ

### UZAKTAN ALGILAMA İLE GEMRİK ANTİKLİNALİ (BOZOVA PETROL SAHASI, ADIYAMAN, TÜRKİYE) HİDROKARBON MİNİSİZİNTİLERİNİN HARİTALANMASI

Avcıođlu, Emre

Yüksek Lisans, Jeodezi ve Cođrafi Bilgi Teknolojileri Bölümü

Tez Yöneticisi: Doç. Dr. H. Şebnem Düzgün

Ortak Tez Yöneticisi : Prof. Dr. G. M. Vedat Toprak

Eylül 2010, 116 sayfa

Hidrokarbon (HK) minisizintıları olası haznelerin göstergeleri olabilmektedir. Bu nedenle HK minisizintılarının haritalanması, petrol arama faaliyetleri çerçevesinde kullanılma potansiyeline sahiptir. Bu çalışma, Gemrik Antiklinali'ndeki (Adıyaman) HK minisizintılarının ve ilgili yüzey kil mineral başkalaşmalarının haritalanmasına yöntem sunmaktadır. Bu amaçla, potansiyel HK minisizinti bölgelerinden örnekler toplanmış ve jeokimyasal incelemeye gönderilmiştir. Bu incelemeler sonucunda numunelerde HK içeriđi bulunmuştur. Çalışma alanına ait bir ASTER görüntüsü elde edilmiş ve HK içeren örneklerin bulunduğu bölgeyi en iyi haritalayan bir ASTER şerit bağdaşması türetilmiştir. HK minisizintılarının yüzey başkalaşım ürünlerinin belirlenmesi için ilk olarak numunelerin yansıma tayfları Saha İzgeölçeri kullanılarak

ölçülmüştür. İkincil olarak tayfi olarak tanımlanmış örneklerin tayf eğrileri Birleşik Devletler Jeoloji Araştırma Kütüphanesi verileri temel alınarak, bu kayaçları meydana getiren kil minerallerinin tayfları belirlenmiştir. Sonuçlar HK sebepli yüzey başkalaşım minerallerinin kaolinit, montmorillonit, illit, çöl cilası(desert varnish) ile dipyre olduğunu göstermiştir. Son olarak seçilen bu üyelerin yansıl karakterleri soğurma ve kaynakça verileri temel alınıp ASTER şerit bağdaşması olarak temsil edilmiştir. HK minisızıntıları ve ilgili yüzey göstergelerini haritalamak için gerekli temel bileşenler çözümlenmesi, Crosta Tekniği kullanılarak yapılmıştır. HK minisızıntılarını haritalamak için geliştirilen bu işlemsel süreç, tüm ASTER görüntüsüne uygulanmıştır. Geliştirilen HK minisızıntılama işleminin uygulanması sonucu edilen haritalardan türetilen yeni yer kontrol noktaları arazide ziyaret edilmiştir. Arazi çalışmaları sonucu anormallik gösteren alanların, jeokimyasal içeriği bilinmeksizin, %65'ten fazla oranlarda atfedilen alanla benzerlik taşıdığı gözlenmiştir. Ayrıca, elde edilen bu HK haritasının doğruluğunu test etmek için, MATLAB yazılımında kullanılan ve bir görüntü işleme algoritması olan AdaBoost döngüsü çalıştırılmıştır. Analiz çıktılarına göre AdaBoost döngüsü sonuçları ile, HK sızıntılarını haritalamak için geliştirilen yöntemin büyük oranda örtüştüğü saptanmıştır.

Anahtar kelimeler: Uzaktan algılama, jeoloji, hidrokarbon minisızıntı, AdaBoost, crosta , Bozova, Adıyaman, Türkiye

**TO MY L(w)IFE,  
THE SUPERB FAMILY OF ALL TIMES AND MY SUPER GRANDMA**

## ACKNOWLEDGMENTS

I wish to express my deepest gratitude to my supervisor Assoc. Prof. Dr. H. Şebnem DÜZGÜN and co-supervisor Prof. Dr. G. M. Vedat TOPRAK for their guidance, advice, criticism, encouragements and insight throughout the research. Their orientation against problem solving was really professional.

I would like to open a separate paragraph to my dear family members for their non-stop love, support, patience, orientation and motivation during my life; my mother Selma AVCIOĞLU, being one of the most successful primary school teachers in the world and my all time furious and sweet father Oğuz AVCIOĞLU who is the most genius father in the world. Hopefully, the most intelligent civil engineer in the universe, my merely brother Dr. Onur AVCIOĞLU, deserves special thanks for his extra brainstorming, intervention and contribution for this thesis study. I really learned a lot from the way he acts against problems.

The author also thank to TPAO for the opportunity which led this thesis work to be completed comprehensively. In accordance with that, I would like to express my gratitude to my manager Murat SARGINALP for his continuous support, share, teaching and patience during my thesis completion. Also i would like to thank to Nedim COŞKUNER, N. Serkan ÖZTAN, Tünay CESUR, Mustafa DEMİRCİ, Dr. Hayati KOYUNCU and Örsan AYTEKİN for their technical support, field orientation, handling, kindness, friendship and favor.

And finally, the stand-alone wonder of the world, my l(w)ife, Ms. Gökben AYKANAT, deserves very special appreciation for her presence on the world for me to breathe.

## TABLE OF CONTENTS

ABSTRACT .....	iv
ÖZ .....	vi
ACKNOWLEDGMENTS .....	ix
TABLE OF CONTENTS .....	x
LIST OF TABLES .....	xii
LIST OF FIGURES .....	xiii
LIST OF ABBREVIATIONS .....	xvii
CHAPTER .....	1
1. INTRODUCTION .....	1
1.1 Definition of Problem .....	1
1.2 Purpose and Scope .....	1
1.3 Study Area .....	3
1.4 The Work Flow .....	4
1.5 Outline of Organization .....	7
2. GEOLOGY of the STUDY AREA .....	8
2.1 Regional Geology .....	8
2.2 Geology of the Study Area .....	9
2.2.1 Germav Formation .....	10
2.2.2 Bozova Formation .....	12
3. FORMATION AND TYPES OF SEEPAGES .....	13
3.1 Seepage Formation Models .....	13
3.2 Seepage Examples from Turkey .....	20

4.PREVIOUS REMOTE SENSING STUDIES.....	22
5.RESEARCH METHODOLOGY .....	26
5.1 Selection of Study Area .....	26
5.2 Methodology.....	28
5.2.1 ASTER Data .....	30
5.2.2 Crosta Technique Applied to ASTER Image.....	37
5.2.2.1 Building the Masks .....	37
5.2.2.2 Crosta Technique .....	41
5.2.3 Field Data.....	64
5.2.3.1 Sample Collection and RockEval Pyrolysis.....	64
5.2.3.2 Analyses of Samples in SPECMIN Software .....	68
5.2.4 The AdaBoost Algorithm.....	73
6.RESULTS.....	76
7.DISCUSSIONS AND CONCLUSIONS.....	93
REFERENCES.....	96
APPENDIX A.....	103
APPENDIX B .....	107
APPENDIX C .....	116

## LIST OF TABLES

### TABLES

Table 1.1 Software used in this study.....	5
Table 5.1 ASTER image properties used in mapping the study area.....	34
Table 5.2 The positions of samples collected from the reference valley.....	65
Table 5.3 RockEval results showing TOC_RE, S1 and TMAX values.....	68
Table 5.4 SPECMIN Analysis for 8 samples. Bold prints are selected end members after the analyses.....	72
Table 6.1 Endmembers and related band combinations to map them.....	82
Table 6.2 AdaBoost weights computed.....	89

## LIST OF FIGURES

### FIGURES

Figure 1.1 Location maps of Gemrik Anticline and Ugurca Village (maps generated from Google Earth).....	4
Figure 2.1 The regional geology.....	9
Figure 2.2 Geology of study area.....	10
Figure 2.3 A section showing the surface of Germav Formation.....	11
Figure 2.4 Bozova Formation.....	12
Figure 3.1 Seepage due to stratigraphy (Schumacher, 1996).....	14
Figure 3.2 Various seepage types (H. Løseth et al., 2008).....	15
Figure 3.3 HC seepage routes and the surface alterations (Kahn, 2008).....	16
Figure 3.4 A stratigraphic boundary which acts as a potential conduit for migration of oil (Kahn, 2008) .....	17
Figure 3.5 Microseepage model and related anomalies on soils and sediments (Schumacher, 1996).....	18
Figure 3.6 Some of the surface manifestations owing to HC seepage (Yang et al., 2000).....	20
Figure 3.7 A seepage example from Cudi Mountain, Şirnak Region.....	21
Figure 4.1 Dark blue crosshairs are locations of measurements made outside of the spectral anomalies; light blue crosshairs are locations within the anomalies Staskowski (2004).....	24
Figure 5.1 The reference valley covering the selected study area.....	27
Figure 5.2 HC microseepage in detail.....	28
Figure 5.3 Flowchart of the study.....	30
Figure 5.4 Spectral signs of ASTER bands.....	31

Figure 5.5 Layer stacking window of ENVI 4.5.....	32
Figure 5.6 Comparison of Input Spectra from Original Image.....	33
Figure 5.7 ASTER image showing Gemrik Anticline.....	35
Figure 5.8 The final image illustrating Gemrik Anticline.....	36
Figure 5.9 NDVI applied to the study area .....	38
Figure 5.10 Water+cloud mask applied to the study area.....	39
Figure 5.11 Vegetation mask applied to the study area.....	40
Figure 5.12 Spectral Library Viewer in ENVI 4.5.....	43
Figure 5.13 ASTER bands shown on the spectral characteristic of illite3.....	44
Figure 5.14 Selection of appropriate bands to perform PCA.....	44
Figure 5.15 The statistics file showing the eigenvalues is displayed.....	45
Figure 5.16 Mean and standard deviation values of PC4.....	46
Figure 5.17 Interactive stretching .....	47
Figure 5.18 This map shows the distribution of Illite3 endmember.....	48
Figure 5.19 The Illite map of Gemrik Anticline.....	49
Figure 5.20 Eigenvalues for Kaosmec5. Green rectangle shows the highest opposite standings. PC4 is selected to map Kaosmec5 endmember.....	50
Figure 5.21 Statistics file of PC4 showing mean and standard deviation values belonging to kaosmec5 endmember.....	51
Figure 5.22 Kaosmectite map.....	52
Figure 5.23 Desert Varnish.....	53
Figure 5.24 Statistics show that PC4 has to be selected since it has the highest and negative values.....	54
Figure 5.25 The distribution of desert varnish3 over Gemrik Anticline.....	55
Figure 5.26 PC selections to map Dipyre Mineral.....	57
Figure 5.27 The Dipyre map over Gemrik Anticline.....	58

Figure 5.28 Statistics file of Montmor9 endmember.....	60
Figure 5.29 Montmorillonite mineral distribution over Gemrik Anticline.....	61
Figure 5.30 Hydrocarbon microseepage map of Gemrik Anticline.....	63
Figure 5.31 HC bearing samples over study area underlain by DEM.....	64
Figure 5.32 Basic parameters obtained by pyrolysis .....	66
Figure 5.33 Display of ViewSpec Pro Software .....	69
Figure 5.34 The SPECMIN PRO 3.0 user interface.....	70
Figure 5.35 Feature Search window of SPECMIN.....	70
Figure 5.36 Feature Selection Program (FSP) which is created for selecting training data for AdaBoost Algorithm.....	74
Figure 5.37 Weight values gathered for band 4 after 150 iterations.....	75
Figure 6.1 An anomalous HC accumulation close to Uğurca Village.....	77
Figure 6.2 A layered structure with HC content and calcite in Germav Formation. Circles show calcite infillings.....	78
Figure 6.3 Bleached red beds close to possible oil seepage zone .....	80
Figure 6.4 Thematic map of Gemrik Anticline.....	83
Figure 6.5 Mineral distributions on anomalous and non-anomalous regions (Kahn, 2006).....	84
Figure 6.6 Anomalous regions in the first stop of ground truth study.....	85
Figure 6.7 A river bed towards the second stop.....	86
Figure 6.8 A non-anomalous location which was supposed to be an anomalous zone regarding HC microseepage map.....	86
Figure 6.9 Another anomalous location was explored as one of the ground checking points visited.....	87
Figure 6.10 A location showing prospect close to reference valley.....	87
Figure 6.11 An outcropped layer in the location shown in the previous image.....	88
Figure 6.12 AdaBoost offered HC microseepage map.....	90

Figure 6.13 Zoom image to reference valley showing the HC map according to AdaBoost analysis.....91

Figure 6.14 Crosta Technique generated HC microseepage map versus AdaBoost Algorithm outputs showing the reference valley in the cross point.....92

## **LIST OF ABBREVIATIONS**

HC: Hydrocarbon

FSP: Feature Selection Program

PC: Principal Component

DN: Digital Number

AVG: Average

SD: Standard Deviation

VNIR: Visible Near Infra Red

NIR: Near Infra Red

SWIR: Short Wave Infra Red

TIR: Thermal Infra Red

NDVI: Normalized Difference Vegetation Index

USGS: United States Geological Survey

GPS: Global Positioning System

ASTER: Advanced Spaceborne Thermal Emission and Reflection Radiometer

Landsat TM: Landsat Thematic Mapper

UTM: Universal Transverse Mercator

WGS: World Geodetic System

ED: European Datum

# **CHAPTER 1**

## **INTRODUCTION**

### **1.1 Definition of Problem**

Oil exploration facilities need as much data as it can infer from nature since its rate of success is too low. Hydrocarbon (HC) microseepage is one of those critical information about possible reservoirs. Hence mapping HC seepages would be supportive information for exploring possible reservoirs. Remote sensing technology, which is developing day by day, would have contribution for mapping HC microseepages. Considering its efficiency and exactness, remote sensing would be useful for oil exploration facilities. In this study, an algorithm is developed for an ASTER Satellite image which maps the HC seepages in Bozova Oil Field, Adiyaman, Turkey.

### **1.2 Purpose and Scope**

The non-stop development of technology has contribution to various fields. Remote sensing studies can be considered among those. As a result, geological applications make use of these technological improvements since remote sensing technology has subscription to geological issues. One of the major issues of geology is oil exploration. These facilities require every single data since it is hard to find the location of an oil reservoir. HC seepage terminology can be a useful indicator for a possible reservoir since reservoirs leak.

HC seepage can stand out in three ways:

1- Makroseepage form

2- Microseepage form

3- Surface alterations related to HC seepage.

Macroseepages generally occur where oil found a place to leak to surface. They would be observed locally in river beds, through fault zones or lineaments. Microseepages, on the other hand, would show a non-scale distribution on the soil. Depending on the concentration, they would alter the soil yielding some surface manifestations which indicate its presence. Surface alterations related to HC seepage would be realized by its reductional zone created by hydrocarbons. These can be clay mineral alteration, bleaching of red beds due to removal of iron, geobotany, etc.

The main purpose of this study is to develop a methodology for mapping HC microseepages with its related surface clay mineral alteration using ASTER Image in Bozova Oil Field, Adiyaman. Other purposes include offering spectral data to literature about new absorption signatures of hydrocarbons and satisfying the demand in literature for developing the success rate of feature mapping by using image processing algorithms which make use of spatial information. There are several reasons for choosing HC microseepage mapping in this field. Oil exploration facilities in Adiyaman have become consistent in the past decades than it had previously. Also petroleum companies operate in the area to discover new reservoirs and to develop certain fields. In addition to this, tectonic dominancy in Adiyaman has increased the possibility of reservoirs to leak. This is another reason for selecting this place for studying.

The scope of the study contains two applications which are used for mapping HC microseepages and their related clay mineral alteration in the ASTER Image. Firstly, Crosta Technique is applied for mapping the features. Secondly, AdaBoost, the image processing algorithm is applied to the HC microseepage maps generated from Crosta Technique to improve the results further in mapping the area.

### **1.3 Study Area**

The main focus of this study is Gemrik Anticline. It is in the close vicinity of Uğurca Village which is in South East Anatolia (Figure 1.1). In particular, Uğurca Village locates between the borders of Şanlıurfa and Adiyaman. The location has been affected by tectonism since it is close to the East Anatolian Fault zone. In accordance with that, the area is full of anticlines and synclines in which Gemrik Anticline is the one for the area of interest.

Gemrik Anticline is surrounded by Ataturk Dam Site in the north east side and bounded by Bozova Fault in the south west side. Akpınar Town and Bozova Town are the main settlement areas in the surrounding region. The axis of Gemrik Anticline extends from north west to south east and covers approximately 20 km<sup>2</sup>. It is included within 1:25.000 scale map section.

The reason for choosing this area is that it is mainly composed of Bozova and Germav Formations which are mainly composed of marl lithology on which almost no vegetation occurs. For this reason, performing the studies would be easier on bare soil where mapping of the area and ground truth applications are carried out comprehensively.

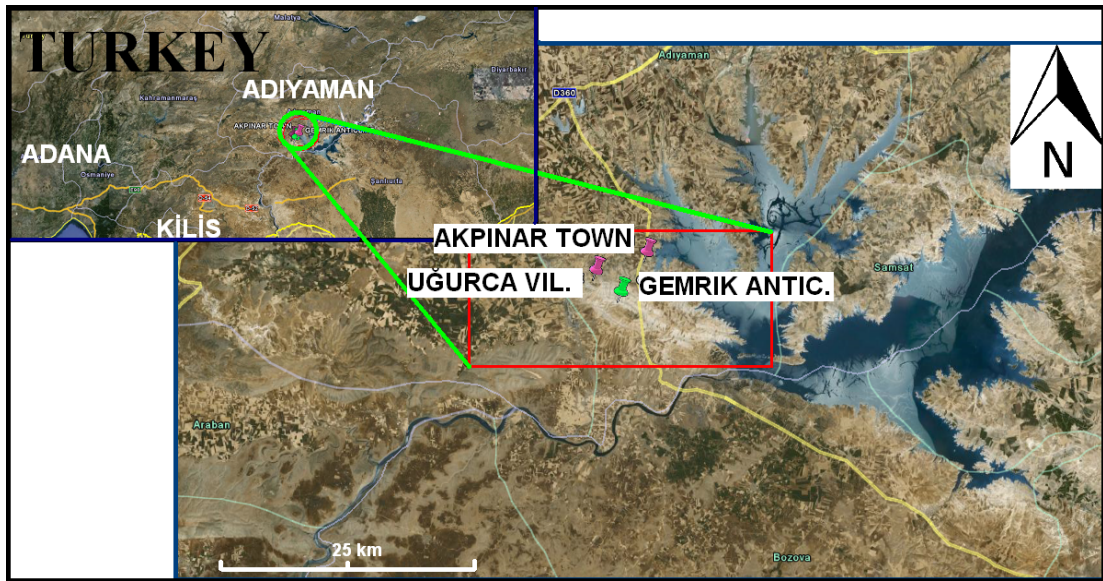


**Figure 1.1** Location maps of Gemrik Anticline and Ugurca Village (maps generated from Google Earth).

#### **1.4 The Work Flow**

There are basically four steps that compose this thesis study.

The first step includes literature information research. The general applications and usage of remote sensing techniques in geology is scanned and discriminated.

The second step of work involves selecting of the field of study. Obviously the field selection takes some time since it is not easy to find a field that has HC microseepage. Following process was field data collection. The collected samples were analyzed both in spectroscopic and geochemical point of view. The spectroscopic measurements were performed in MTA (General Directorate of Mineral Research and Exploration) labs with ASD (Analytical Spectral Devices) Field Spectrometer. The spectral curves generated by the spectrometer was verified and displayed in ViewSpec Pro Software. The geochemical analyses of the samples were conducted in TPAO (Turkish Petroleum Company) geochemistry laboratories using RockEval machine.

The third step of the thesis is composition, analysis and production of data under specific software. Initially the 1/25.000 scaled Digital Elevation Model (DEM) of the study area is generated in Mapinfo Professional 7.5. The controlling and correction of digitized features were performed in ArcMap 9.3. Simultaneously, the spectroscopic results were analyzed via SPECMIN PRO 3.0 Software. The preprocessing of acquired ASTER (Advanced Spaceborne Thermal Emission and Reflection Radiometer) level 3A image, Crosta Technique which makes it possible to map hydrocarbons with their prominent clay mineral alteration and all of the related computations were performed in ENVI 4.5. The HC map generated by Crosta Technique became the training sample (inputs) for AdaBoost algorithm in MATLAB Software. The feature selection matrices in AdaBoost algorithm output the maximum weighted ASTER bands which independently indicate the most appropriate bands for mapping HC microseepages. A final field reconnaissance is organized for field verification of previous ASD Spectrometer measurements and prospect points that are produced from Crosta analyses. These spectroscopic measurements are gathered using a different type of spectrometer, SVC-HR Field Spectrometer.

The last step involves gathering of all the data and yielding the results. The composition of text that documents this study is completed in this step. Table 1.1 shows software used in this thesis.

**Table 1.1** Software used in this study.

<b>SOFTWARE</b>	<b>PURPOSE</b>
MAPINFO PROFESSIONAL 7.5	Digitizing of Gemrik Anticline
SPECMIN 3.0	Spectral unmixing of samples
ARCGIS 9.3	Corrections Analyses related to elevation, slope and aspect DEM generation Overlay analysis (with ASTER image and ENVI maps)
ENVI 4.5	Preprocessing of ASTER image PCA Thematic map generation Feature analyses
MATLAB 2009A	AdaBoost algorithm execution
FEATURE SELECTION PRO.	Selecting of positive and negative features (training samples for AdaBoost algorithm)
ASD FIELD SPEC. PRO. & SVC HR-1024	Displaying and analyzing of; ASD and SVC type spectrometer measurements, separately

## **1.5 Outline of Organization**

Chapter 1 starts with the definition of problem. Considering the study area, the purpose and scope is given. Work flow is stated and organization outline finishes first chapter. Chapter 2 separately explains the geology of the region and the geology of the area in detail. Chapter 3 shows the formation of seepages, how they outcrop and the role of remote sensing technology in this consideration. Some seepage examples from Turkey are also given. Chapter 4 includes remote sensing studies related to HC microseepage. Chapter 5 explains the study area, data used and the methodology of the study. Chapter 6 shows the analyses performed using Crosta Technique and the AdaBoost algorithm with the results gathered. Chapter 7 focuses on discussions, conclusions and recommendations for further. Appendix A contains all spectral measurements done within this study. Appendix B illustrates the figures of the samples collected from field.

## **CHAPTER 2**

### **GEOLOGY of the STUDY AREA**

This chapter documents the geology of the region and the geology of the selected study area, respectively.

#### **2.1 Regional Geology**

Information given about the geology of the region and study area was synthesized from the reports by Tok (2003) and by Yilmaz (2000). The region is in South East Anatolia which in particular locates between the borders of Şanlıurfa and Adiyaman. The location was intensely affected by tectonism since it is close to the East Anatolian Fault zone. In accordance with that, lithological variance is observed. North and East part of the region is bounded mostly by East Anatolian Fault, in which clastical type deposits outcrop. Considering the southern and the western parts, carbonates show dominance. The geological map of the region is displayed in Figure 2.1.

There are basically two formations in our area of interest. The first one is Germav Formation which consists of shale, sandstone, marl and limestone. The other is Bozova Formation which has marl content (Yılmaz, E., and Duran, O., 1997). The hegemonic surface structures are east-west oriented anticlines and synclines due to the compressional regime of active tectonism.

The folded morphology becomes smoother in south region. Some of the dominant tectonic structures in the region are Adiyaman, Harmancik and Bozova Faults (Tok, N., 2003).

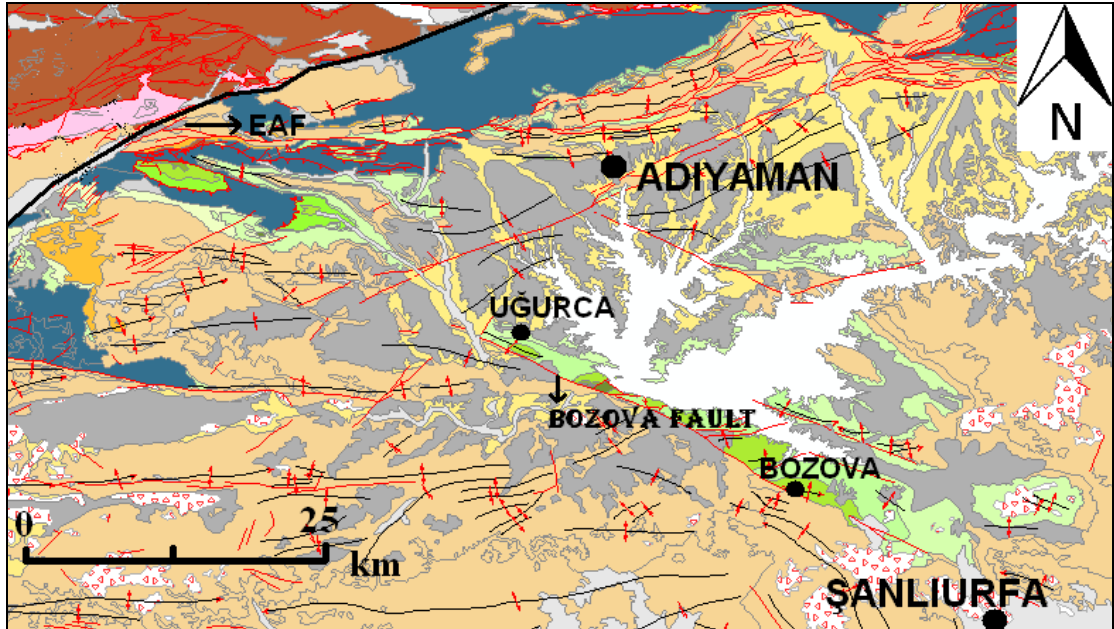


**Figure 2.1** The regional geology (from TPAO 1/500.000 scaled map of South East Anatolia). East Anatolian Fault (EAF) sources the active tectonism in the area. The location of Uğurca Village is also demonstrated.

## 2.2 Geology of the Study Area

The main focus of this study is Gemrik Anticline. Uğurca Village lies on the structure which is in the close vicinity of Akpınar Town, Adiyaman. The study area is surrounded by Ataturk Dam in the north-east and Bozova Fault in the south-west.

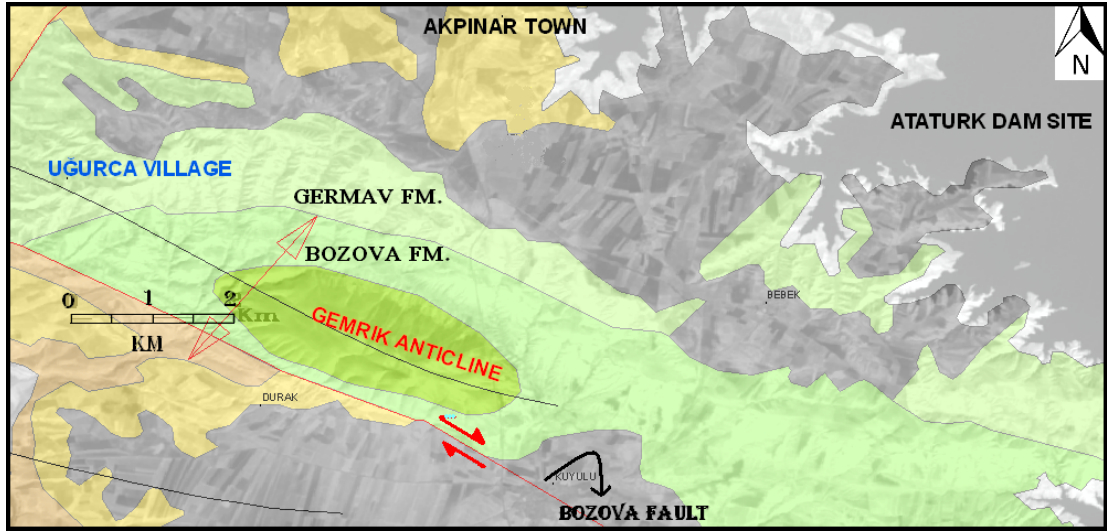


**Figure 2.2** Geology of study area showing considered formations, Gemrik Anticline with its fold axis and the strike of Bozova Fault (from TPAO 1/500.000 scaled map of South East Anatolia which is underlain by the DEM of the study area generated).

The area is covered by several outcropping formations such as Germav Formation, Bozova Formation, Sayindere Formation, Gaziantep Formation and Şelmo Formation. Basically, the interested formations are Germav Formation and Bozova Formation (Figure 2.2). The reason for this is the possession of considered hydrocarbon microseepage inside them. The reason probably comes up from the organic material content and occasional sandstone layering inside these formations which somehow form the conditions for oil generation and migration.

### **2.2.1 Germav Formation**

Upper Maastrichtian to Paleocene aged Germav Formation was deposited in the sea environment. The color distribution of the formation varies from gray to greenish gray (Figure 2.3). The lithological content of the Germav formation is composed of shale, marl and sandstone. In the content of these lithologies, pyrite accumulations, rarely glauconite and silicification, clay and clay minerals are present.

Besides, foraminiferal, algal, planctonic fossils are found in the marl and in rare limestone lithology. Germav Formation is divided into 2 geological members named as Upper Germav Member and Lower Germav Member.

Upper Maastrichtian aged Lower Germav is underlain by oil producing rock Mardin Limestone in the study area. In addition to this, there a reservoir level came across in the base of Lower Germav which is unconformably in contact with Karababa Formation (Tok, N., 2003). Karababa Formation is a member of Mardin Group Limestone. Upper Germav is deposited in Paleocene time and it is represented by clayey limestone, marl and shale since it formed in deep sea environment.



**Figure 2.3** A section showing the surface of Germav Formation.

### ***2.2.2 Bozova Formation***

The age of Bozova Formation is Late Campanian to Early Miocene (Çoruh, 1991). The formation is deposited in deep sea environment. The thickness of the formation in Gemrik Anticline is 190 meters (Güven et al., 1991). The color varieties are light bluish grey, green, grey, greenish grey, white, dirty white and whitish grey. The lithologic composition of Bozova Formation is basically marl, clayey limestone with rare cherty intercalations and shale (Yılmaz, E., and Duran, O., 1997). But the hegemonic lithology is marl and clayey limestone. The section is rarely pink, pinkish grey and ash-grey in color (Figure 2.4.).



**Figure 2.4** Bozova Formation.

## CHAPTER 3

### FORMATION AND TYPES OF SEEPAGES

This section includes background information linked to seepages and discusses examples from Turkey.

#### 3.1 Seepage Formation Models

Hydrocarbon microseepage is *"the surface expression of a migration pathway, along which petroleum is currently flowing, driven by buoyancy from a sub-surface origin"* (Clarke & Cleverly 1991). These surface features are evidence of the presence of oil and/or gas reservoirs below, even though they may not be enough to classify an area as economically interesting (Thompson et al. 1994, Schumacher 2002).

There are several materials such as oil, water, H<sub>2</sub>S, CO<sub>2</sub> and many other that seep from its reservoir. Oil seeps would be offshore or onshore. Considering the fact that traps leak either they are stratigraphical or structural, and there are several ways that drive seepage mechanism and there are certain clues related to them. Firstly our deal is HC seepage paths. Then HC Microseepage Hypothesis which includes surface manifestations due to HC seepages is explained briefly.

The pushing mechanisms sourced from differences in density and tectonic effects are some examples which cause HC to seep (Horvitz, 1969).

Stratigraphy may also lead to seepage accumulation in a particular place. Figure 3.1 shows some of the possible oil migration pathways due to some variation in stratigraphic conditions onshore.

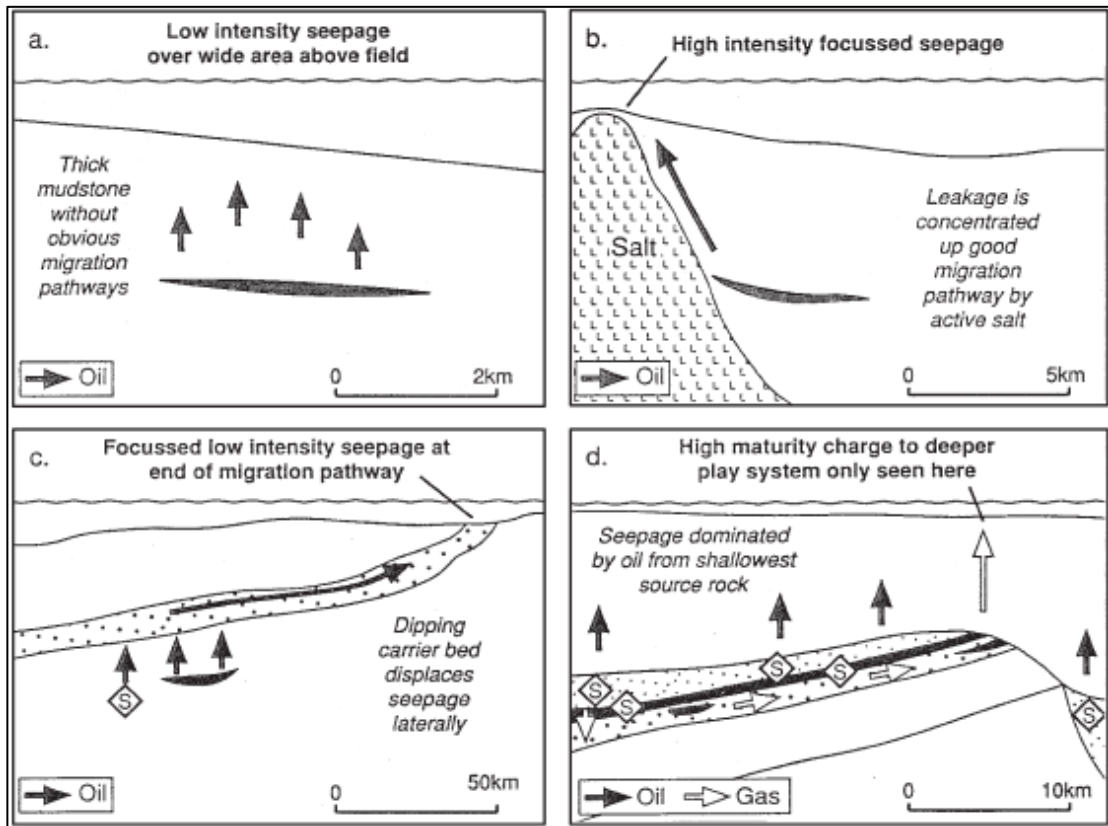


**Figure 3.1** Seepage due to stratigraphy (Schumacher, 1996). In the first case (a), the seepage is not dominant at the surface due to its low intensity over wide area. The second case (b), on the other hand, has accumulation in a specific portion at the surface since the salt dome sums and diverts seepage to a local concentration. The third case (c) shows the displacement of seepage due to dipping carrier beds which results in a low surface print. The last case (d) shows the seepage dominated from the source rock near to surface.

Like HC seepage does on the land surface, it would happen in offshore. Figure 3.2 demonstrates seepage conditions in offshore due to stratigraphic and structural reasons.

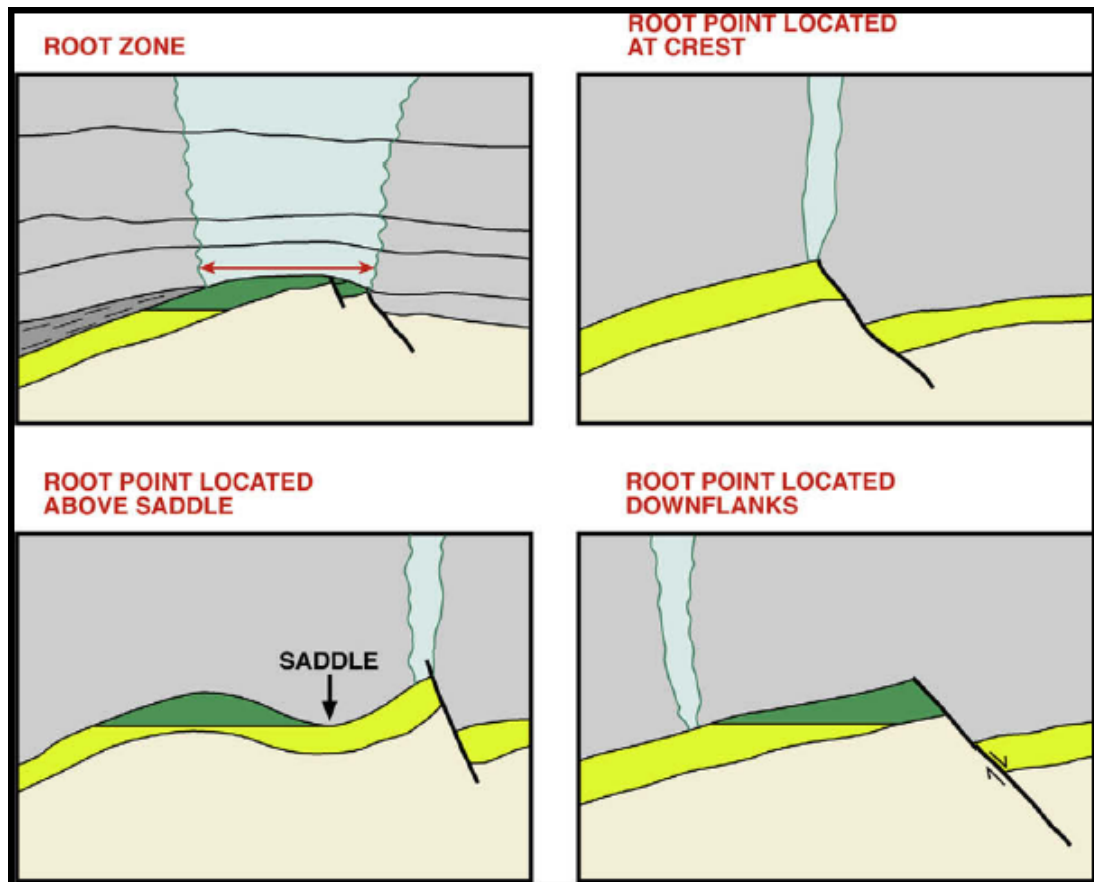


**Figure 3.2** Various seepage types can be observed due to different type of roots. It can be inferred from figures that seepage would be wider or narrower due to different conditions (H. Løseth et al., 2008).

One may infer from these explanations that reservoirs can leak into a certain extent and they would be used as indicators for HC exploration. A scheme in Figure 3.3 clearly illustrates the seepage paths and surface alterations. At this point, remote sensing technology is a useful tool in recognizing those possible surface manifestations due to microseepage of natural hydrocarbons.

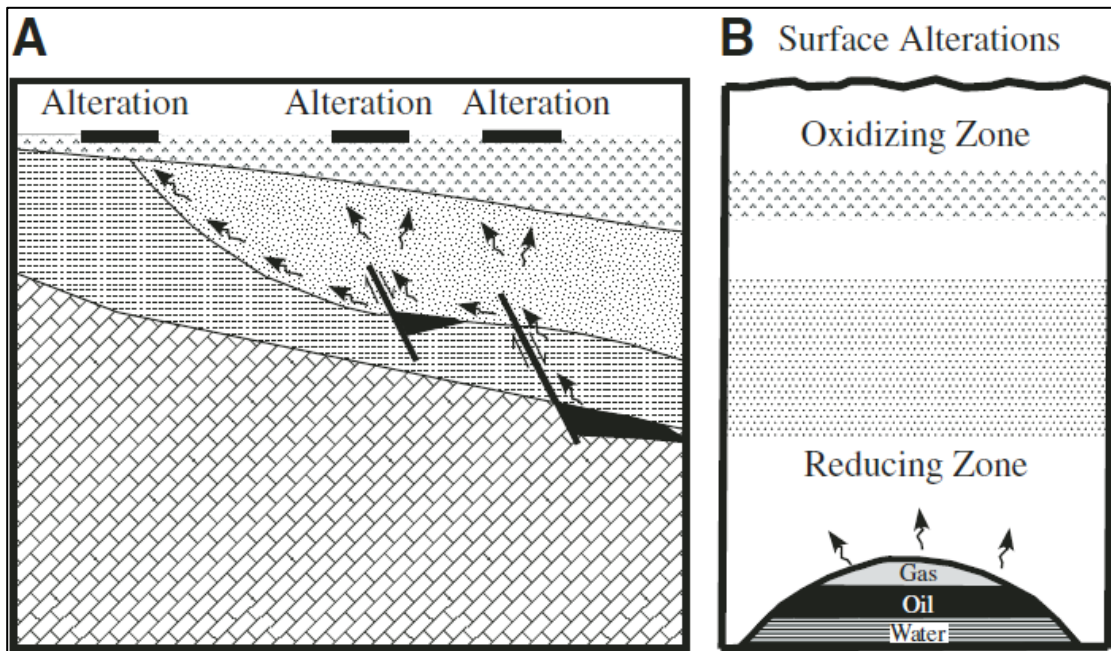


**Figure 3.3** HC seepage routes and the surface alterations (Kahn, 2008).

Another seepage model from Patrick Draw explains a stratigraphic trap (Figure 3.4.). Note that the seeps change direction due to the impervious property of overlying formation. At the surface, hydrocarbons moving along this surface create an anomalous zone of alteration in the overlying soils and sediments, which can be detected remotely (Kahn, 2008).

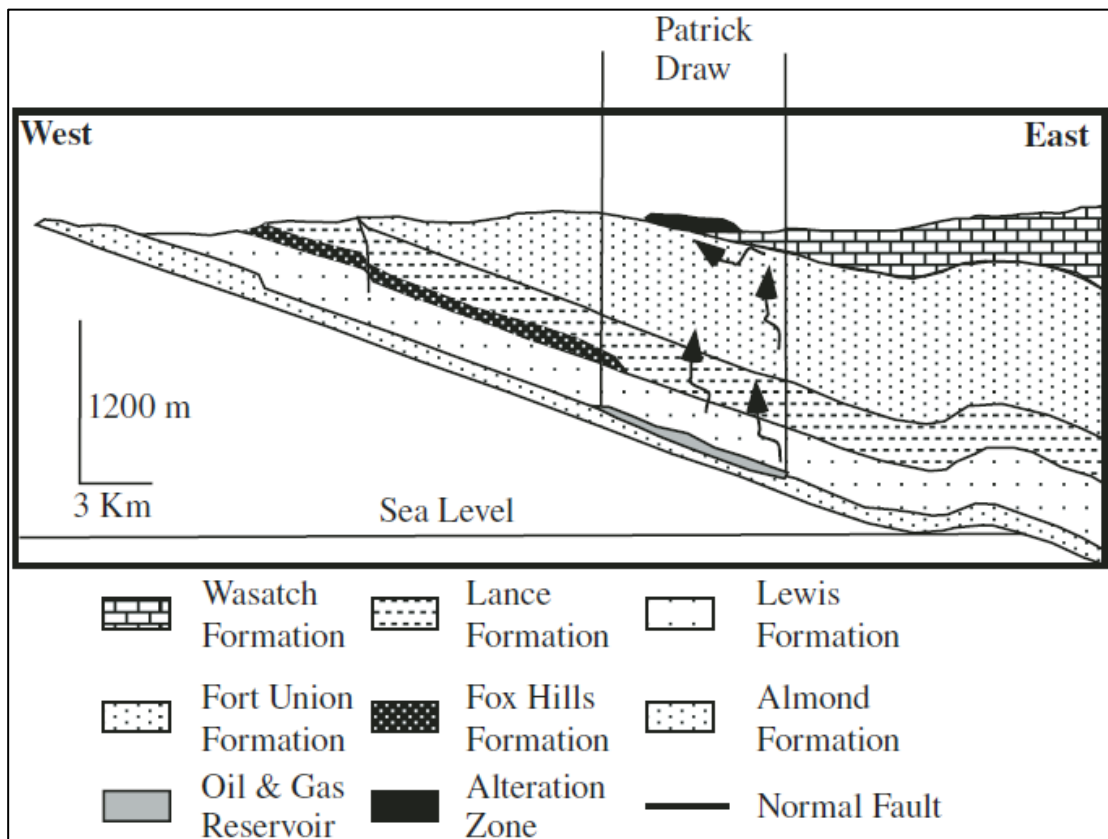


**Figure 3.4** A stratigraphic boundary which acts as a potential conduit for migration of oil (Kahn, 2008).

The explained properties of seepages and their formation show that seepages could be indicative for possible oil reservoirs. Knowing the fact that they are not directories at the decision making point every time but they would courage exploration facilities and provide supportive information for wildcats. Hence, the role of remote sensing technology in detecting oil reservoirs has to be considered. Hydrocarbon Microseepage Hypotheses assumes all near-surface geochemical exploration techniques is that hydrocarbons are generated and/or trapped at depth and leak in varying but detectable quantities to the surface. The surface meaning of HC seeps is best observed in areas with numerous well developed migration pathways and an active petroleum system. It can be concluded, or at least implied, that the anomaly at the surface can be reliably related to a petroleum accumulation below the surface (Figure 3.5.).

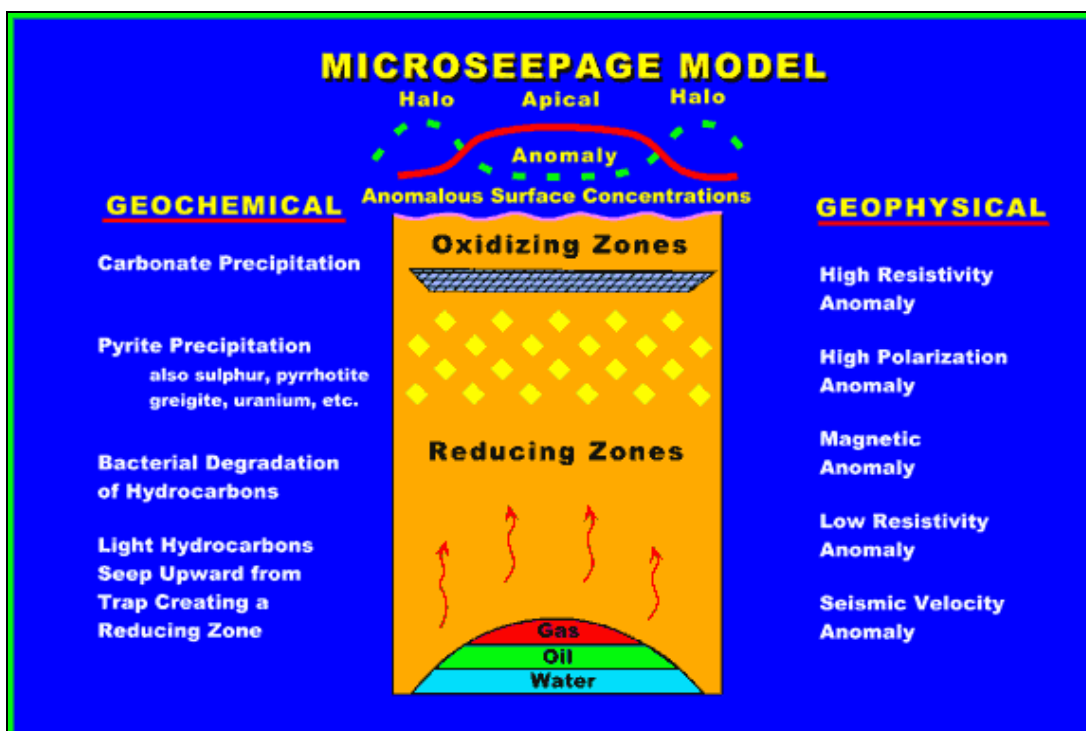


**Figure 3.5** Microseepage model and related anomalies on soils and sediments (Schumacher, 1996)

*“Bacteria and other microbes play a profound role in the oxidation of migrating hydrocarbons, and their activities are directly or indirectly responsible for many of the diverse surface manifestations of petroleum seepage. These activities, coupled with long-term migration of hydrocarbons, lead to the development of near-surface oxidation-reduction zones that favor the formation of this variety of hydrocarbon-induced chemical and mineralogical changes. This seep-induced alteration is highly complex and its varied surface expressions have led to the development of an equally varied number of geochemical and geophysical exploration techniques. Some detect hydrocarbons directly in surface and seafloor samples, others detect seep-related microbial activity, and still others measure the secondary effects of hydrocarbon-induced alteration”* (Schumacher, 1996 and Saunders et al., 1999).

The surface geochemical anomalies of petroleum seepage can take many forms (Figure 3.6.):

- (1) Anomalous hydrocarbon concentrations in sediment, soil, water, and even atmosphere,
- (2) Microbiological anomalies and the formation of "paraffin dirt",
- (3) Anomalous non-hydrocarbon gases such as helium and radon,
- (4) Mineralogical changes such as the formation of calcite, pyrite, uranium, elemental sulfur, and certain magnetic iron oxides and sulfides,
- (5) Clay mineral alterations,
- (6) Radiation anomalies,
- (7) Geothermal and hydrologic anomalies,
- (8) Bleaching of red beds,
- (9) Geobotanical anomalies,
- (10) Altered acoustical, electrical, and magnetic properties of soils and sediments.

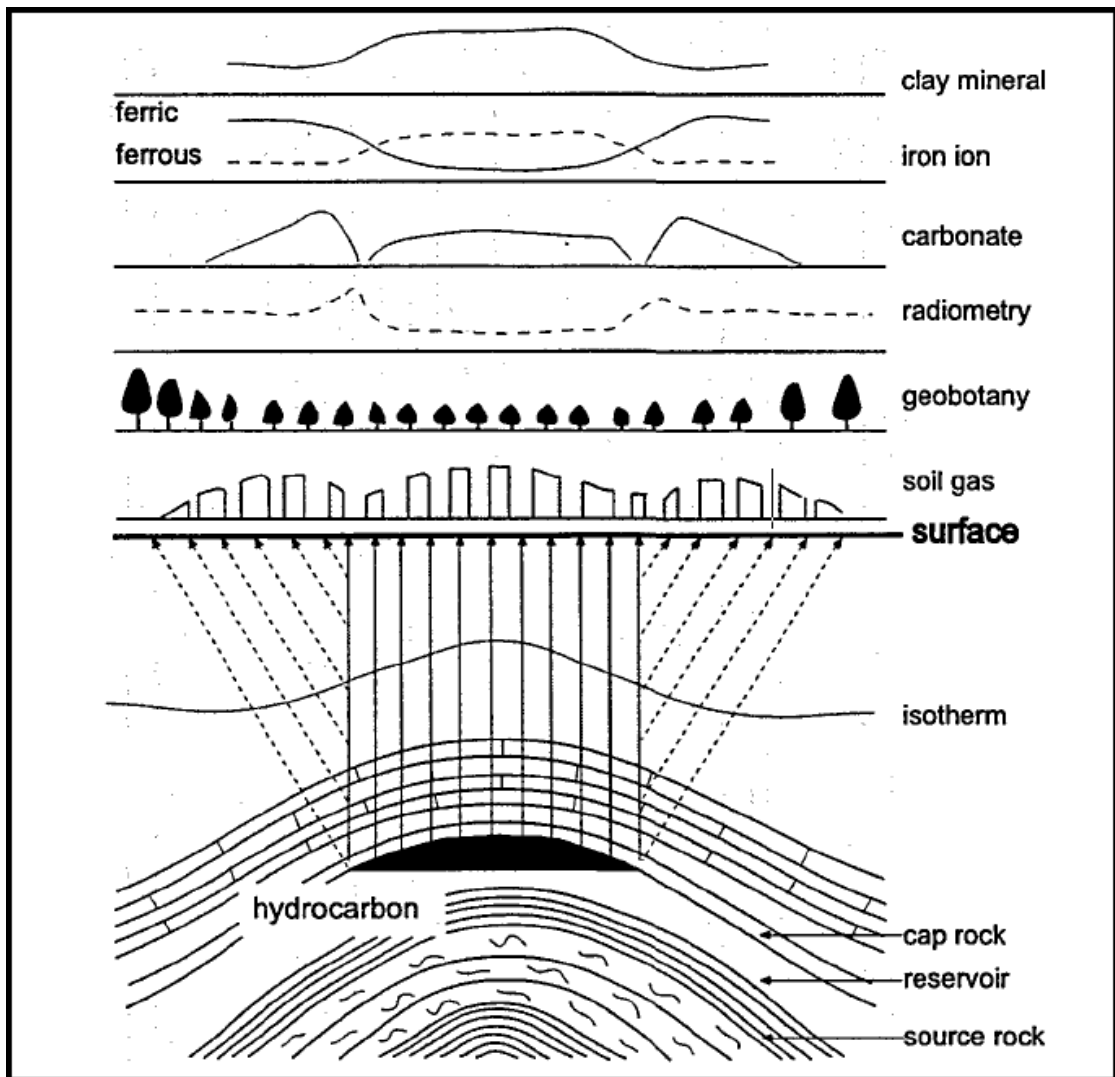


**Figure 3.6** Some of the surface manifestations owing to HC seepage (Yang et al., 2000).

### 3.2 Seepage Examples from Turkey

There are several places that HC seepages are reported. One example can be given in Hatay region which seepages occur inside ophiolites. Visiting the region, it is possible to realize the soil gas sourced from the seepages due to its high content in air. Besides, the largest seepages can be observed in Şirnak Region. Harbul, Silip, Ispindoruk, Rutkekurat, Uludere, Karatepe and Nivekara are some of the veins documented (Şengüler, 2007). Besides, these seepages are currently used for heating purposes in the area, particularly in the documented places (Figure 3.7).



**Figure 3.7** A seepage example from Cudi Mountain, Şirnak Region. Lower left image is an example of a sample (photographed by Emre Avcioğlu).

## CHAPTER 4

### PREVIOUS REMOTE SENSING STUDIES

This chapter includes the remote sensing studies performed on HC seepage hypothesis, HC induced surface alterations and related spectral works considered in the literature.

Kahn and Jacobson (2008) tested the hypothesis that chemical and mineralogical alterations in rocks and soils are related to hydrocarbon microseepages above some of the major oil fields. Their mineralogical, geochemical, and carbon isotope supportive field data is mapped by Hyperion image sensors in which alterations that appear to be associated with hydrocarbon microseepages in the Patrick Draw area of Wyoming.

Lammoglia et al. (2008) tried to characterize HC microseepages in Brazil, using geostatistical analysis of regional hydrocarbon geochemical data yielded from soil samples and digital processing of Enhanced Thematic plus (ETM+/Landsat7 satellite) and Advanced Spaceborne Thermal Emission and Reflection Radiometer imagery (ASTER/Terra satellite). They focused on indirect indicators of HC microseepage and developed band algorithms and applied classification methods to the satellite images to detect anomalies. Results show that ASTER data possesses excellent potential in onshore exploration of hydrocarbons in Brazil.

Petrovic et al. (2008) tried to determine the affects of diverse arrays of chemical and mineralogical changes in rocks and soils due to HC microseepages. To investigate sandstone color alteration patterns, spectroscopy, and ASTER multispectral remote sensing and Synthetic Aperture Radar (SAR) data were used as well as geochemical

analyses of selected samples. Using ASTER satellite images and SAR data, the altered areas were identified and mapped.

Fu et al. (2007) mapped HC-induced mineral alteration using ASTER data. Results demonstrated that band ratios of 2 / 1 and 4 / 8 can discriminate bleached red beds and secondary carbonate minerals due to HC seepage.

Van der Werff et al (2007), showed the results of two pixel-based classifications, namely minimum distance to class means (MDC) and spectral angle mapper' (SAM), that have been carried out on hyperspectral imagery acquired over seepage areas. They found that at best, only 48% and 29% of the pixels that respectively contain crude oil and seepage-related bare soil could be detected, with the inclusion of many false anomalies. Confusion mainly results from the physical characteristics of the anomalies, as these are not unique to seepages. It is concluded that remote sensing of natural hydrocarbon seepages can be improved by image processing algorithms that make use of spatial information. This was one of the key articles that led image processing algorithms to be used in this study.

Zhang et al (2007) worked on Identifying HC leakage induced anomalies such as red bed bleaching, ferrous iron enrichment and clay mineral alteration using Landsat-7 /ETM+ data processing techniques in the west slope of Songliao basin in China. They basically applied three enhancement methods; Principle Component Analyses (PCA), band ratio and false color composition to the images and the distribution of tone anomaly of images is consistent with the field data in most area.

Another study has developed spectral and geochemical ground truth techniques to identify and map alterations caused by HC microseepages and to determine their relationships to the underlying geology in the Patrick Draw area of Southwest Wyoming. Kahn (2006) were successful in determining anomalous zones by training the classification of satellite imagery with spectral inputs of samples collected over previously defined areas of HC microseepage. The result of this study showing the clay mineral distribution over anomalous zone supported this thesis' outputs and became a milestone towards the completion of this study.

Zhang (2006) found out that there are many surface indicators of HC bearing materials at the surface to study mapping of HC microseepages and their prominent alteration utilizing hyperspectral and multispectral remote sensing technology. The study is performed to evaluate uranium mineralizing process and look for new prospect area of uranium deposits.

De Jong and Van der Meer (2004) studied on developing a contextual algorithm for detection of mineral alteration halos with hyperspectral remote sensing. They concluded that the combination of spectral and spatial information in remote sensing images can be considered as a successful method.

Staskowski (2004) made a study to test ASTER utility in HC detection with its related mineral alteration. It is documented that ASTER is a cheap and efficient tool for mapping geochemical anomalies related to hydrocarbon seepage (Figure 4.1).

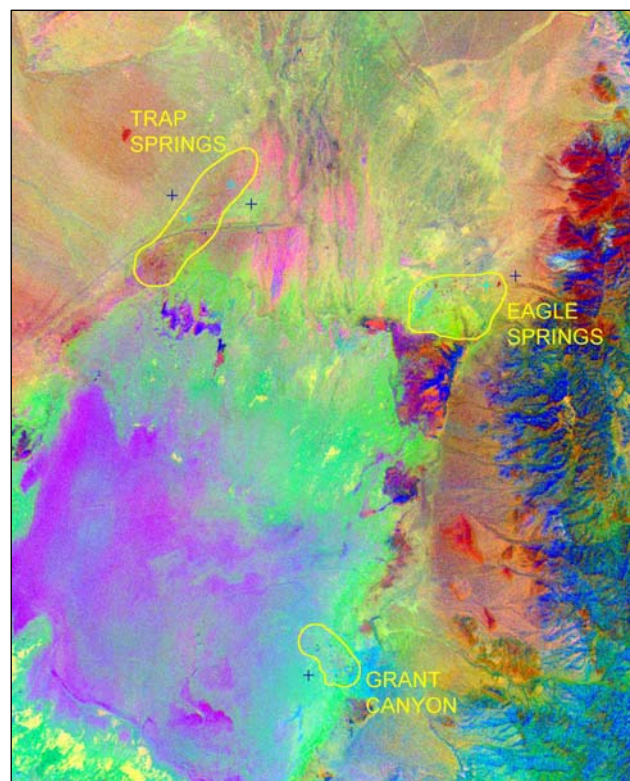


**Figure 4.1** Dark blue crosshairs are locations of measurements made outside of the spectral anomalies; light blue crosshairs are locations within the anomalies Staskowski (2004).

Kuhn et al. (2002) made a study on indexing an algorithm for hyperspectral detection of hydrocarbons. The study demonstrated that the generated algorithm can be used for efficiently detecting HCs. Tests also showed that the HC index derived from the absorption feature 1.73  $\mu\text{m}$  processes even if this feature appears only weakly in the pixel spectra. Besides, HC-bearing materials and oil contaminated ground could be detected and located using HC index images.

Most researchers working in the field have used 2.31  $\mu\text{m}$  for hyperspectral remote sensing of detecting hydrocarbons. The 1.73  $\mu\text{m}$  feature is very close to a major water absorption maximum but Höring et al. (2001) showed the potential of the 1.73  $\mu\text{m}$  feature for direct detection of HC bearing materials.

Yang et al. (2000) studied on direct detection of onshore hydrocarbon microseepages by remote sensing techniques. They stated that hydrocarbon-induced surface alterations of soil and sediments and associated anomalous vegetation that can be identified from remote sensing imagery are reduction of ferric iron (red bed bleaching), conversion of mixed-layer clays and feldspars to kaolinite, increase of carbonate content and anomalous spectral reflectance of vegetation.

Clutis (1989) stated spectral signatures of hydrocarbon bearing materials have characterized absorption at 1.73 and 2.31  $\mu\text{m}$ . This article composed the basis of HC mapping process in this thesis study since it presents unique absorption features for HC material.

## **CHAPTER 5**

### **RESEARCH METHODOLOGY**

In this chapter, research methodology is explained. Study area selected, methodology used, field data and the AdaBoost algorithm are the issues covered within the chapter.

#### **5.1 Selection of Study Area**

As stated previously, there are basically three places in Turkey that HC microseepage can be observed. The first one is in Şırnak region. Considering its remoteness and topographical condition, this area is not selected. The second one is in Hatay region. Seeps in Hatay are not wide enough to be detected by satellite imagery and they are located within ophiolites which has no significance for oil exploration facilities. The study area, which is the third appropriate place among the seepage locations, is chosen where microseepage can obviously be observed. In addition to that, the area is close to urban and topographical properties are suitable. The study area selected is shown in Figure 5.1.



**Figure 5.1** The reference valley covering the selected study area.

Figure above indicates the HC microseepages show distribution throughout the reference valley. The intersection of grayish blue colour (anomalous region) and yellowish brown colour (red beds and bleached zone indicating non-anomalous region) is the boundary of HC microseepage. The microseeps can be observed in the basement of the valley since the river intensely eroded the soil. Figure 5.2 shows the hydrocarbon microseepages at the valley bottom.

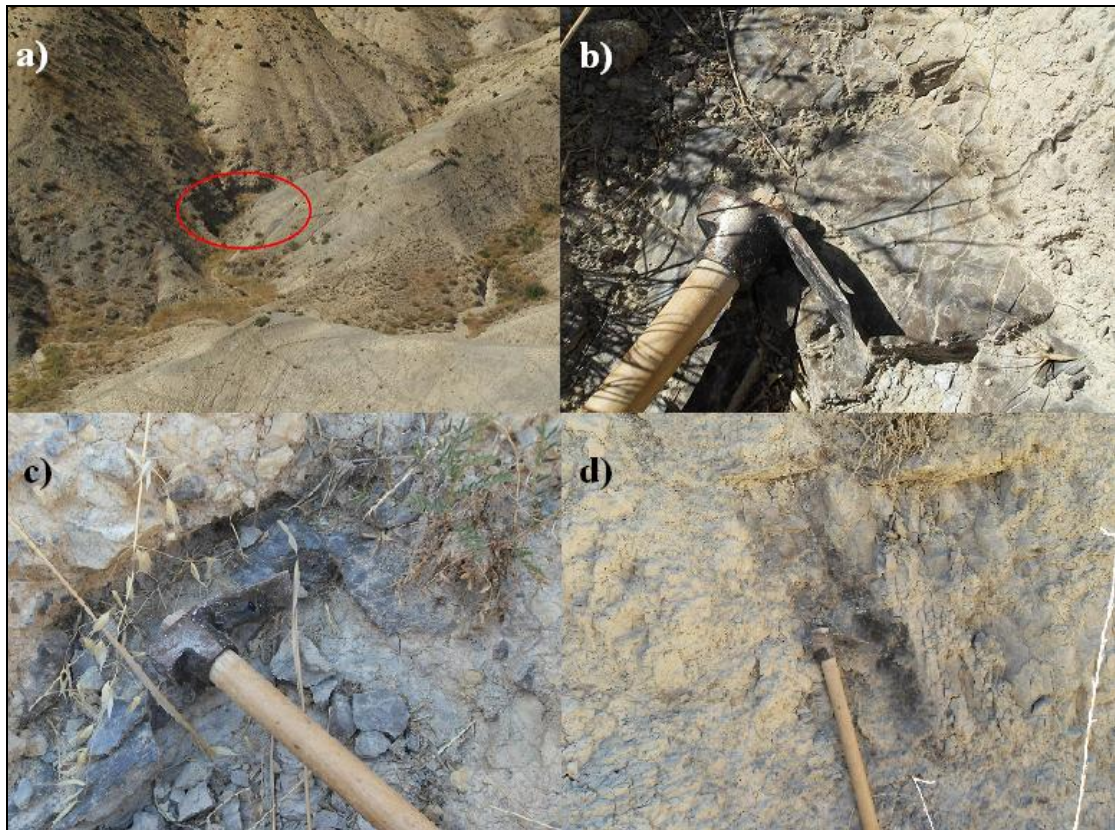


**Figure 5.2** HC microseepage in detail. a) Red circle shows the selected portion of the river bed, b) Microseepages inside the river bed, c) A scene from the meandering side of the river, d) HC shows when the bank of the river is dug by hammer.

## 5.2 Methodology

The flowchart in figure 5.3 illustrates the steps carried out from beginning to end. The short descriptions of steps are explained below as two major branches and the details are presented in the further pages in this chapter.

Firstly, samples are collected from field and their spectral reflectances are measured using field spectrometer. Following, these samples were analyzed considering their geochemical content in which results showed that all of the eight hand specimens were found to have hydrocarbon ingredient.

Secondly, the gathered ASTER granule with AST3A1\_0603280820100810120032 id is preprocessed after the stacking of VNIR and SWIR bands. Here, atmospheric correction and masking operations were performed. Then literature review is completed before performing Crosta Technique in order to generate feature maps. During literature review, spectral properties of some clay minerals and their applications were synthesized. But one of the most important contributions of literature survey was gathering unique hydrocarbon absorption features and applications of HC mapping studies.

Crosta technique is based on Principle Component Analysis (PCA) which includes selecting the appropriate principle components according to eigenvectors to map the target feature. After trial and error process for mapping the features, the most appropriate band combinations for specific features were determined based on field data and literature information. At this point, HC map was generated based on unique absorption characteristics of HC bearing materials gathered from literature. After application of the successful band combinations to the whole image which generate feature maps, ground truth was performed. The AdaBoost algorithm, whose training samples were collected from Crosta generated HC map, was applied in order to test and improve the accuracy of Crosta Technique in mapping HC microseepages and to determine the most appropriate bands which is suitable for mapping HC microseepages. By doing this, an algorithm is developed under the consideration of suggesting the most suitable bands for mapping a particular feature. Finally, the accuracy assessment study was conducted by comparing the results of Crosta generated HC microseepage map with that of AdaBoost yielded.

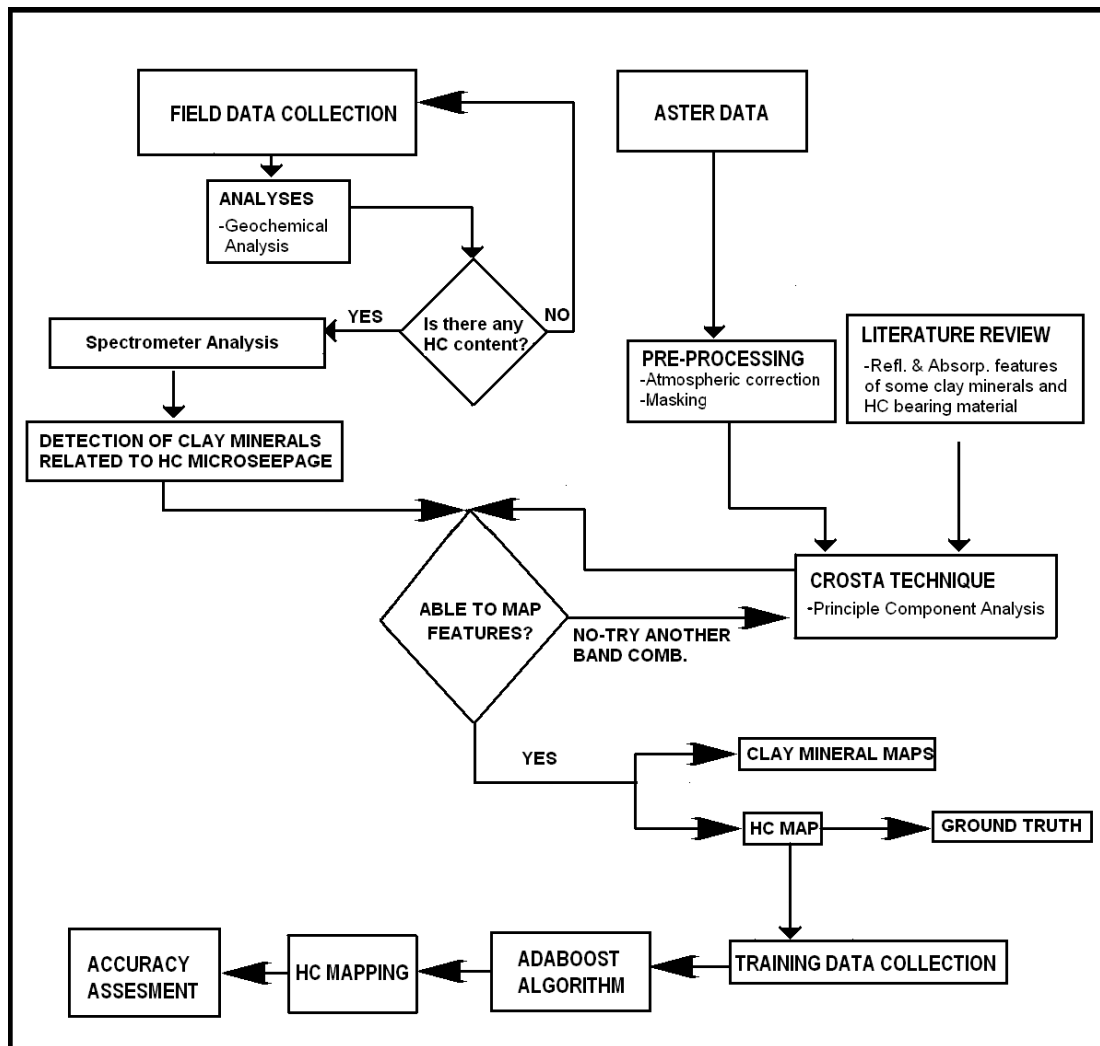


**Figure 5.3** Flowchart of the study.

### 5.2.1 ASTER Data

ASTER (Advanced Spaceborne Thermal Emission and Reflection Radiometer) is an advanced multispectral sensor that is a facility instrument selected by NASA to fly on the Terra polar orbiting spacecraft in December 1999, and covers a wide spectral region from visible to thermal infrared with 14 spectral bands with high spatial, spectral and radiometric resolution. The Terra spacecraft is operated in a circular, near polar orbit at an altitude of 705 km. The orbit is sun-synchronous with a local time of 10:30 a.m. The repeat cycle is 16 days. The wide spectral region is covered

by three telescopes, three VNIR (Visible and Near Infrared Radiometer) bands with a spatial resolution of 15 m, six SWIR (Short Wave Infrared Radiometer) bands with a spatial resolution of 30 m and five TIR (Thermal Infrared Radiometer) bands with a spatial resolution of 90 m. In addition one more telescope is used to see backward in the near infrared spectral band (band 3B) for stereoscopic capability that will produce a base-to-height ratio of 0.6 (ASTER User's Guide, 2007). Figure 5.4 shows the spectral response profiles of all bands as a function of the wavelength and the detailed information about the spectral and spatial characteristics of ASTER bands.

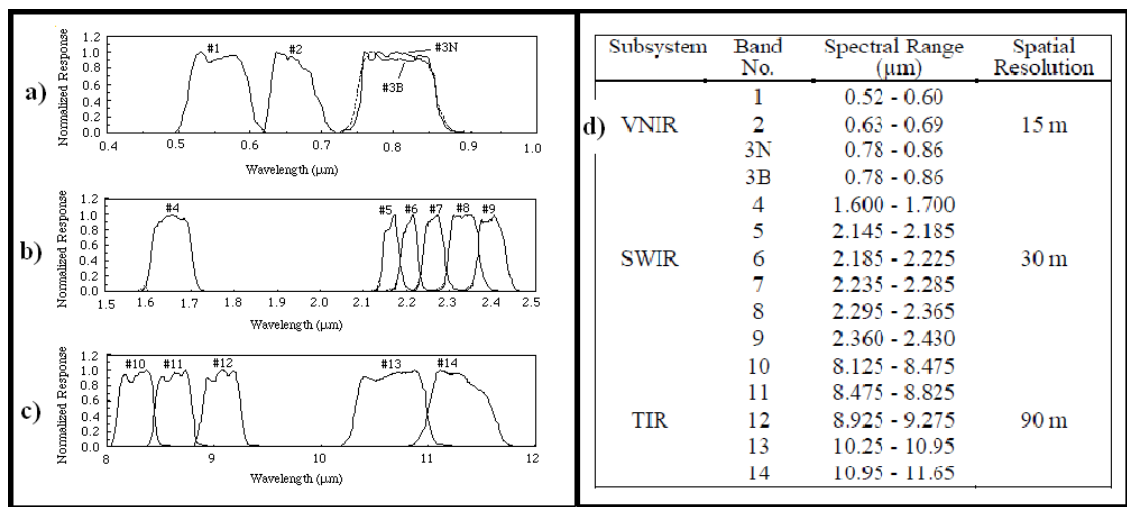


**Figure 5.4** Spectral signs of ASTER bands, a) VNIR, b) SWIR, c) TIR, d) Spectral passbands and spatial resolutions of ASTER bands (ASTER User's Guide, 2007).

ASTER level 3A image showing a scene of the study area is gathered. The image has already been registered and orthorectified. Before preprocessing of the image, firstly VNIR and SWIR bands are combined. For combining the two band sets, ENVI's Layer Stacking function is used (Figure 5.5.). This function enables the user to merge the band sets on a constant pixel size. In order to combine VNIR and SWIR bands, 15 meters of pixel size is used. Bilinear type resampling is selected since it performs a linear interpolation using four pixels to resample the warped image. The appropriate projection, datum and zone are selected before stacking the nine bands.

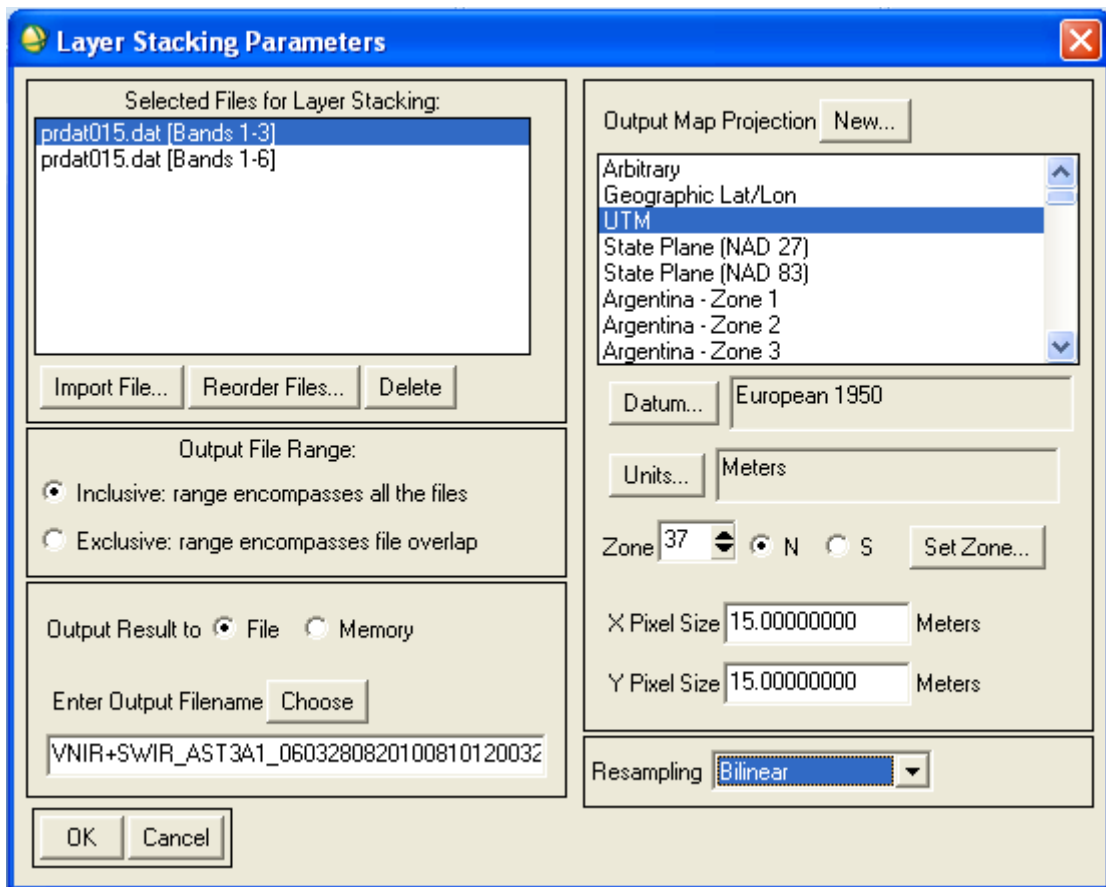


**Figure 5.5** Layer stacking window of ENVI 4.5 and the selected parameters to combine the two band sets.

Preprocessing of image, on the other hand, includes atmospheric correction. Common atmospheric correction functions are ENVI's FLAASH and PCI Geomatica's ATCOR2 AND ATCOR3 (depending on terrain attributes) but this time ENVI's Log Residuals function is used. The new Log Residuals calibration tool is designed to remove solar irradiance, atmospheric transmittance, instrument gain, topographic effects, and albedo effects from radiance data. This transform creates a pseudo reflectance image that is useful for analyzing mineral-related absorption features which is the strongest side for selecting this tool considering the aim of this thesis (Figure 5.6).

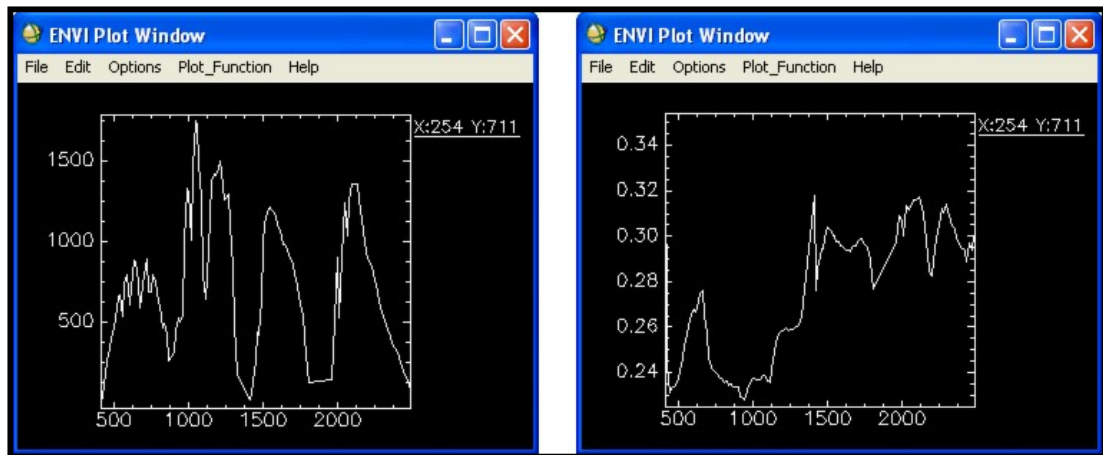


**Figure 5.6** Comparison of Input Spectra from Original Image (left) and Output Spectra from Log Residual Calibrated Image (right) (ENVI User's Guide, 2008).

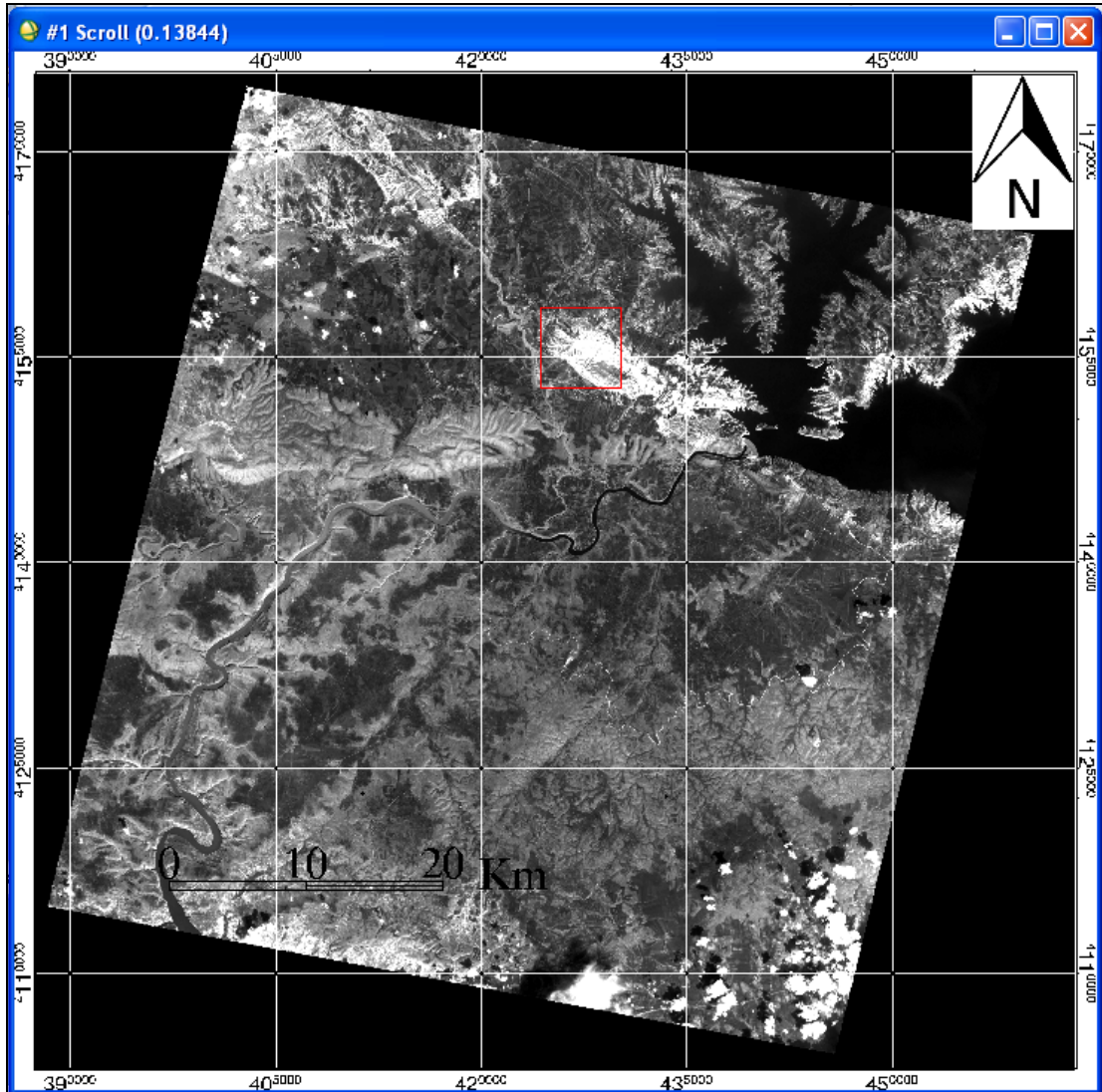
The logarithmic residuals of a dataset are calculated by dividing the input spectrum by the spectral geometric mean and then divided by the spatial geometric mean. The geometric mean is used because the transmittance and other effects are considered multiplicative; it is calculated using logarithms of the data values. The spectral mean is the mean of all bands for each pixel and removes topographic effects. The spatial mean is the mean of all pixels for each band and accounts for the solar irradiance, atmospheric transmittance, and instrument gain (ENVI User's Guide, 2008).

Table 5.1 shows the properties of ASTER scene covering the study area. The VNIR and SWIR bands of the ASTER image are used throughout the thesis. TIR band, however, is not used since the wavelength of TIR band is not necessary in mapping the HC microseepages and the alteration minerals.

**Table 5.1** ASTER image properties used in mapping the study area.

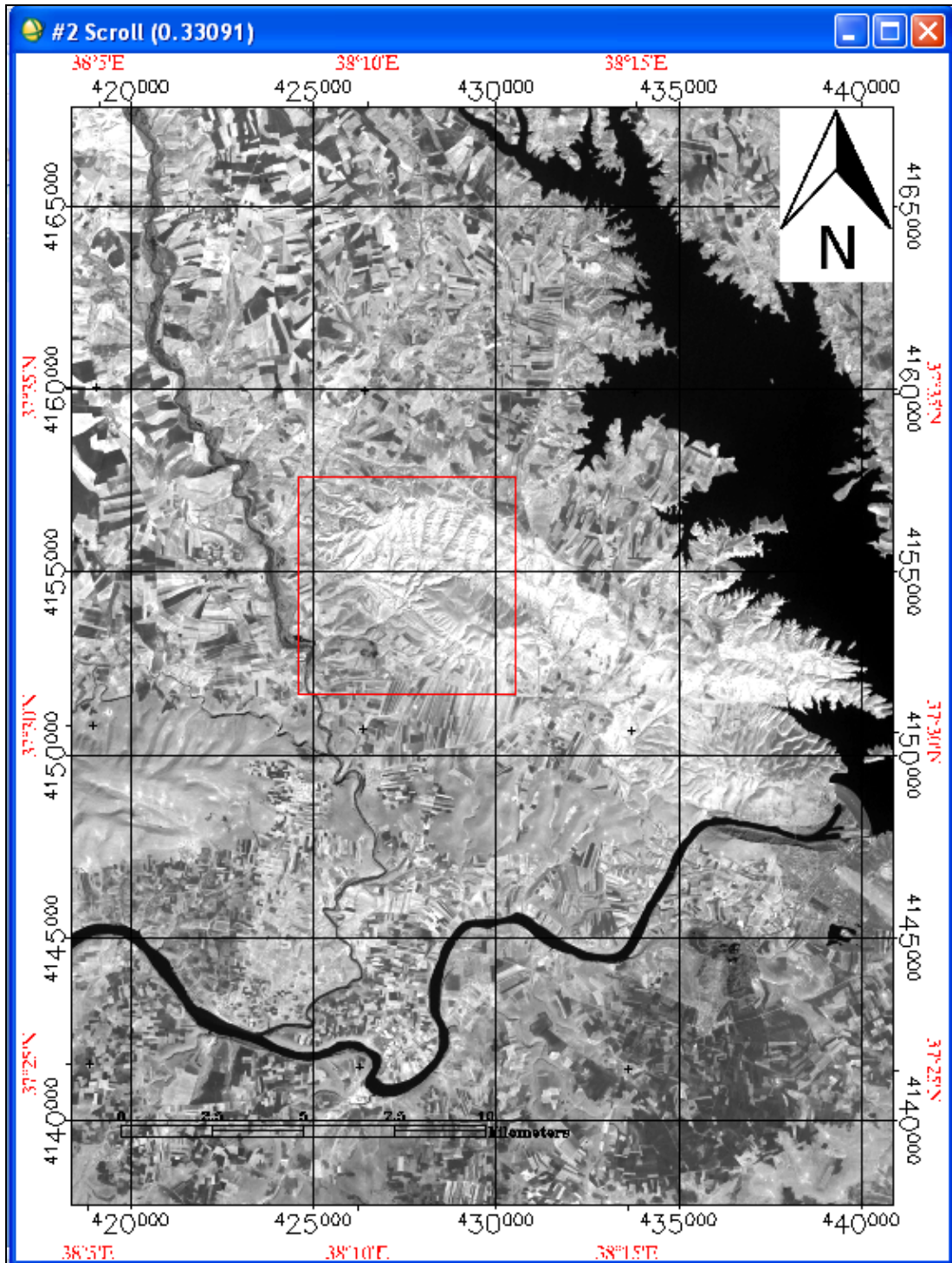
<b>Granule ID</b>	AST3A1_0603280820100810120032
<b>Processing Level</b>	3
<b>Acquisition Date</b>	2006-03-28
<b>Source data Product</b>	ASTL1A 0603280820100603310789
<b>Scene Upper Left</b>	402 934.9440 E, 4 174 937.7000 N
<b>Scene Upper Right</b>	460 384.9440 E, 4 164 167.7000 N
<b>Scene Lower Right</b>	445 834.9440 E, 4 104 392.7000 N
<b>Scene Lower Left</b>	388 414.9449 E, 4 115 132.7000 N
<b>Map Projection Name</b>	Universal Transverse Mercator (UTM)
<b>Datum</b>	European 1950
<b>UTM Zone Code</b>	37 N

Figure 5.7 shows the ASTER image after georeferencing, orthorectification and atmospheric correction. The red box shows Gemrik Anticline.



**Figure 5.7** ASTER image showing the study area. Red box indicates Gemrik Anticline.

In order to simplify the analysis and the studies, the image is cropped and a 1500x2000 pixel image is generated (Figure 5.8.).



**Figure 5.8** The final image over study area illustrating Gemrik Anticline.

### ***5.2.2 Crosta Technique Applied to ASTER Image***

Two main issues are covered within this section. Firstly, the masking operations on the image are explained. Secondly, Principle Component Analysis (PCA) to perform Crosta Technique is explained. This is a technique developed by Crosta and Moore (1989). Also maps generated are illustrated.

#### **5.2.2.1 Building the Masks**

Initially, NDVI (Normalized Difference Vegetation Index) is generated. NDVI is a simple numerical indicator that can be used to analyze remote sensing measurements, typically but not necessarily from a space platform, and assess whether the target being observed contains live green vegetation or not. For this study, band two is selected for NDVI value and band three is selected for NIR value since ASTER is not being recognized by ENVI 4.5. After that, minimum value of -0.077 and maximum value of -0.073 are selected to perform interactive stretching operation in order to produce NDVI of the area (Figure 5.9.). In the region of interest window, minimum threshold value -0.077 and maximum threshold value 100 is selected to create class image.

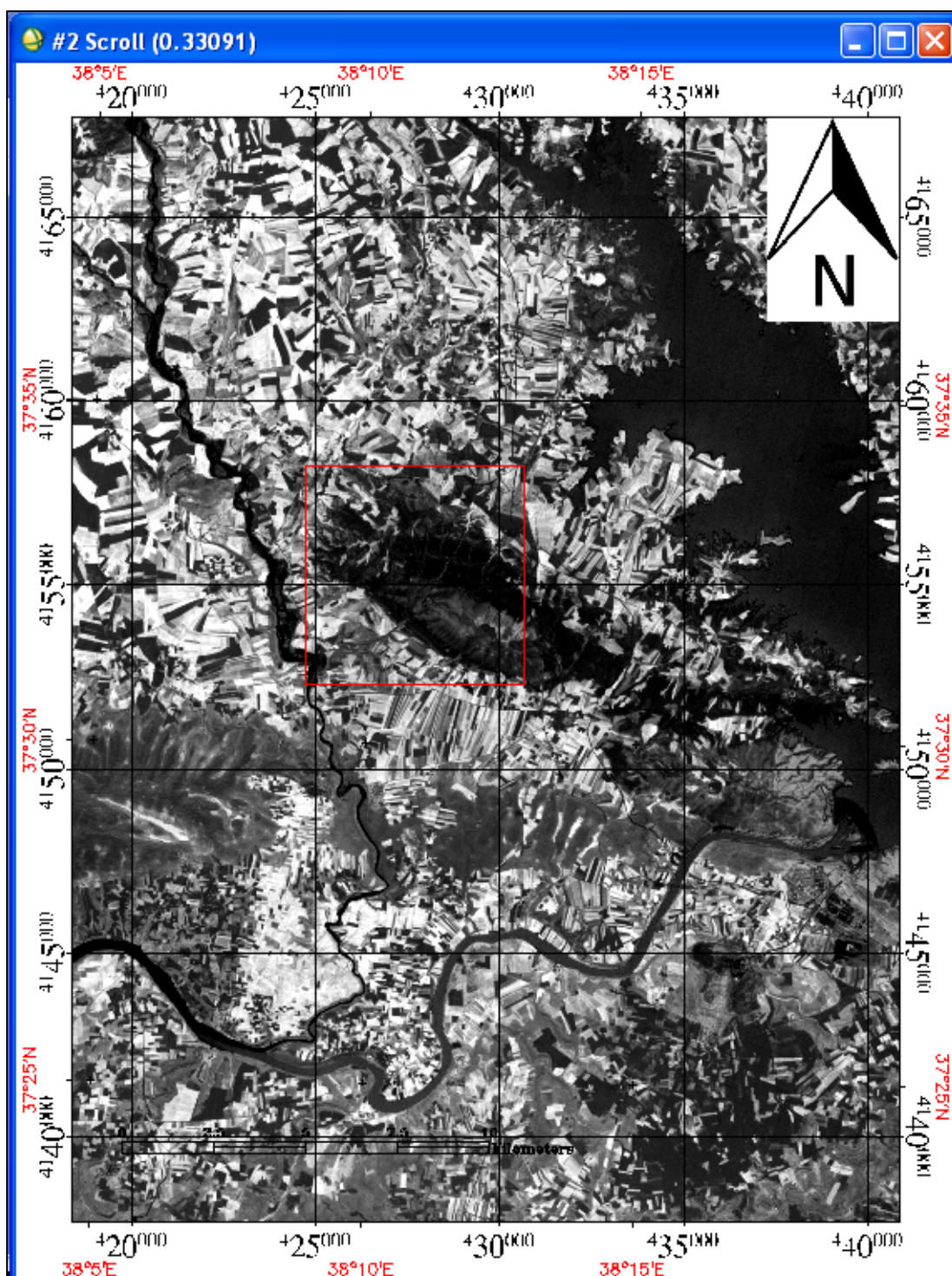


**Figure 5.9** NDVI applied to the study area. The red box shows north-west to south-east trending Gemrik Anticline in which the anticline is not affected by any vegetation cover.

For masking clouds and water bodies on the image, minimum and maximum thresholds used are 0.620 and 0.628, respectively. The water+cloud (blue) mask is illustrated in Figure 5.10.

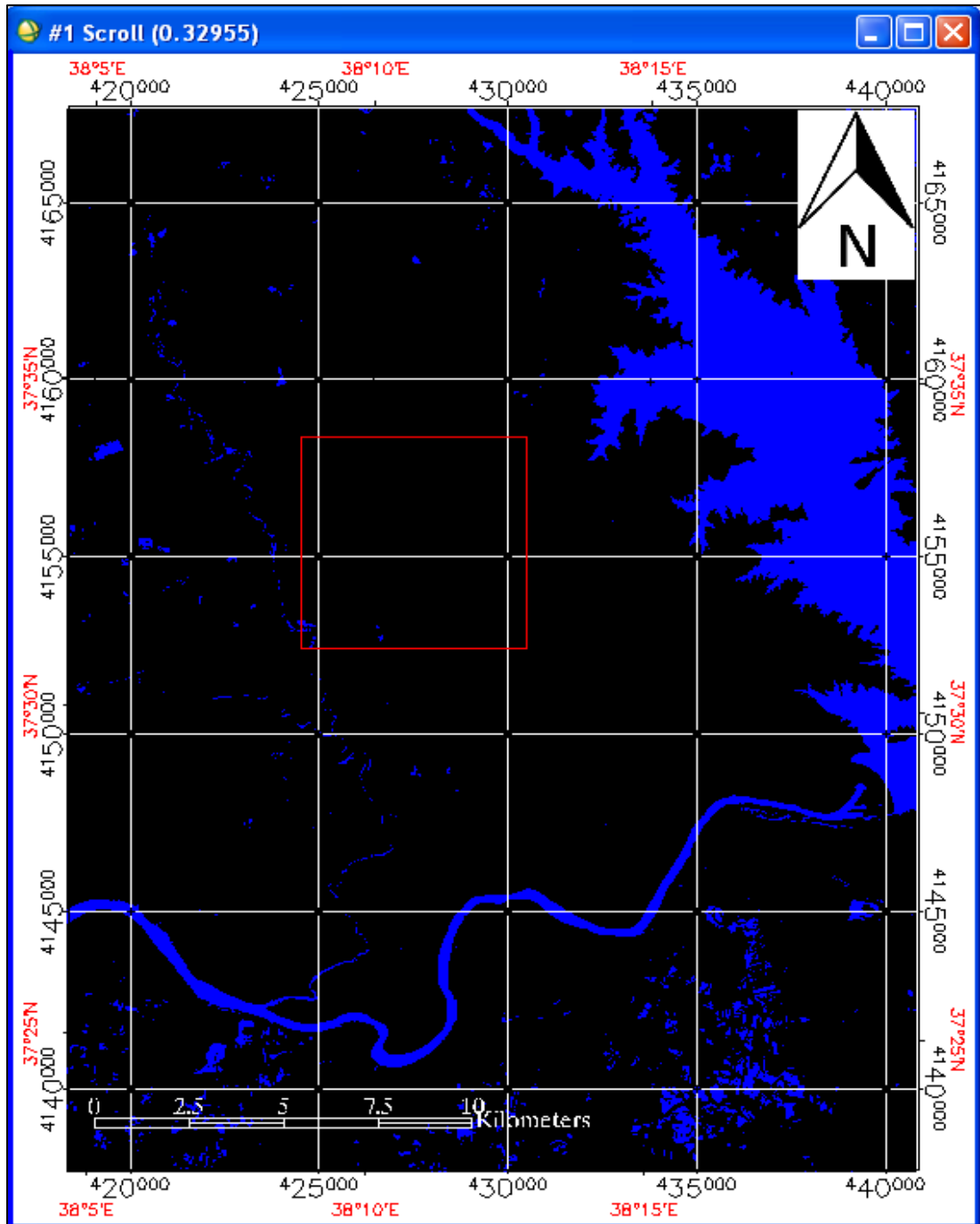


**Figure 5.10** Water+cloud (blue) mask applied to the study area. The red box shows the place of Gemrik Anticline.



All of the three analyses showed that the study area is not affected from any vegetation or cloud cover due to geobotanical effects resulted from HC seepage and the local climatic attributes of Adiyaman despite the March taken ASTER image.

#### **5.2.2.2 Crosta Technique**

PCA is an image processing method used to locate hydrothermally altered zones mostly coupled with Landsat Thematic Mapper (TM) data. The benefit of this technique has greatly been increased with the invention of Advanced Spaceborne Thermal Emission and Reflection Radiometer (ASTER), a 14-band multispectral sensor operating onboard the Earth Observation System (EOS)-Terra satellite. Another to say, the spectral information availability in shortwave infrared (SWIR) portion of the electromagnetic spectrum has been enhanced.

This enhancement supplies a detailed characterization on spectral properties of targets, especially in minerals with diagnostic spectral signatures covering the clay minerals, sulphades and carbonates, among others (Crosta et al., 2003). The spectral resolution provided by the (ASTER), detection of particular alteration assemblages becomes feasible, since it has six spectral bands in the SWIR (bands 4–9), a region where many clay and carbonate minerals show discriminant spectral characteristics (Abrams, 2000).

In this section, PCA was applied as a step of Crosta Technique to ASTER bands. The bands are covering the VNIR and SWIR portion with the objective of mapping HC microseeps and related alteration mineral endmembers in Gemrik Anticline, Adiyaman. Crosta technique is based on the examination of eigenvector values to determine the Principle Components (PC) that concentrate spectral information about specific target materials. Besides, it predicts whether the target materials are represented by bright or dark pixels in the PC images according with the magnitude and sign of the eigenvectors.

It should be reminded that this technique was used for mineral exploration on four and six selected bands of Landsat TM data (Crosta and Moore, 1989; Loughlin, 1991; Ruiz-Armenta and Prol-Ledesma, 1998; Tangestani and Moore 2001; Carranza and Hale, 2002). The technique has also been applied to ASTER data as previously stated (Crosta et al, 2003).

In order to generate maps via Crosta Technique, certain steps were applied. These are;

- 1- The resultant endmember feature is selected and its spectral reflectance is displayed via USGS Library. Note that natural HC spectral reflectance curve is not included in libraries offered by ENVI 4.5. So, the HC microseepage map has been generated using the information from literature and its unique absorption characteristics.
- 2- Based on absorption features of the target mineral, suitable ASTER bands are selected.
- 3- Principle Component Analysis (PCA) is applied and the appropriate PC is selected.
- 4- A threshold is determined using  $(\text{Mean}) + (2 \times \text{Standard Deviation})$  formula.
- 5- Interactive stretching is performed according to the threshold value gathered.
- 6- Masking is applied if it is necessary.
- 7- Feature maps are generated.

All of the above processes are illustrated in the following figures respectively. As an initial step, mineral endmembers offered by SPECMIN software are Illite<sup>3</sup>, Kaolinite<sup>5</sup>, Desert Varnish<sup>3</sup>, Dipyre and Montmorillonite<sup>9</sup>. These minerals are loaded as inputs to USGS Library and the analyses were completed covering these features (Figure 5.12).

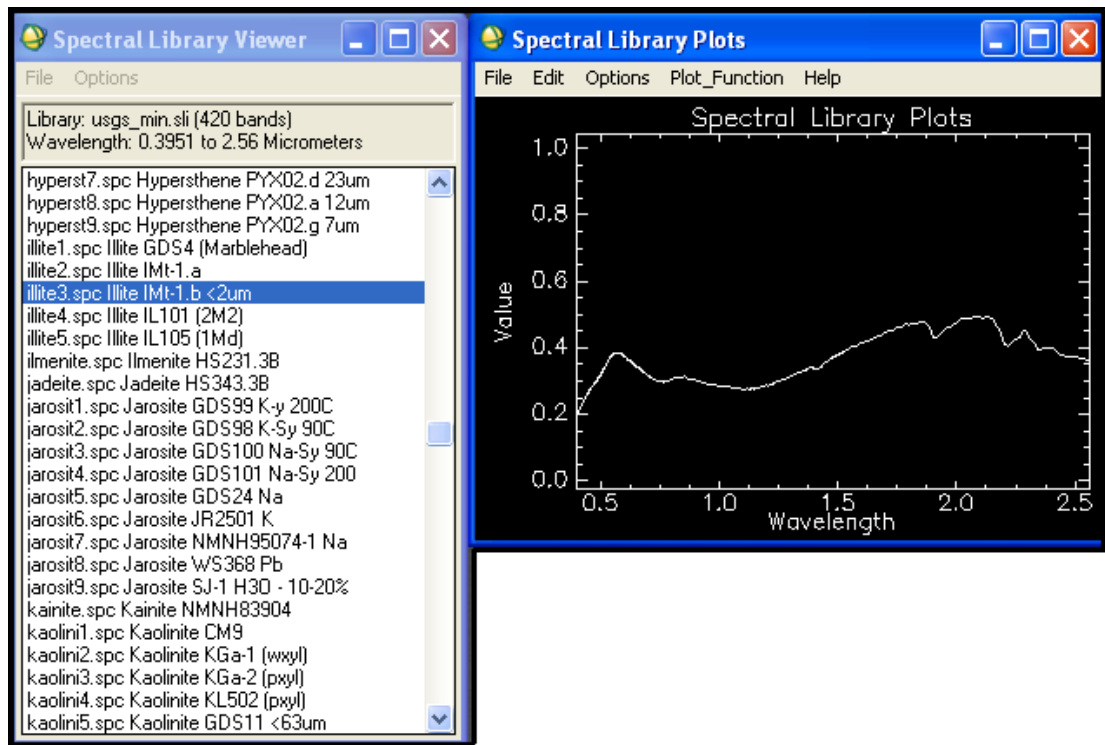


**Figure 5.12** Spectral Library Viewer in ENVI 4.5 and the particular plot for the specific endmember.

After the display of the specific target mineral, ASTER bands are determined considering the spectral characteristics, especially the absorption maxima of the curves. The spectral signatures of ASTER bands and the selected bands to map illite3 endmember are shown in Figure 5.13. The selection of bands is determined considering reflectance features of illite as well as its absorption characteristics. ASTER bands 1, 3, 5, 6 are selected to map illite3 (Crosta, 2003).

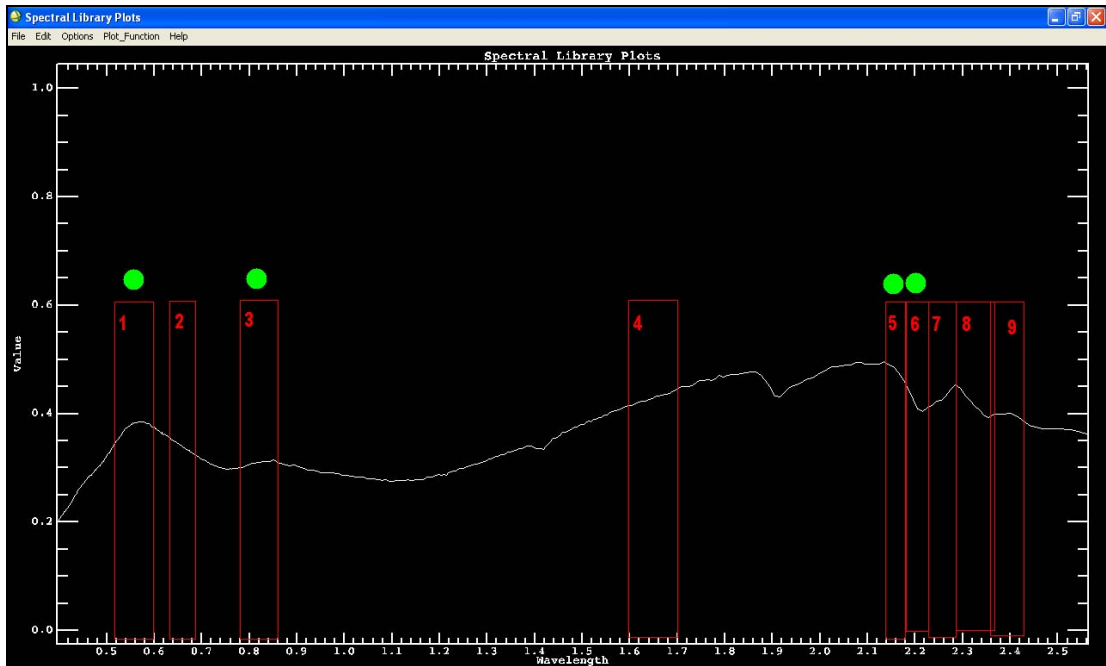


**Figure 5.13** ASTER bands shown on the spectral characteristic of illite3 endmember. Green balls illustrate the selected bands considering the spectral properties of illite3.

In order to get the results of PCA, the bands to map illite3 endmember are selected from the spectral subset (Figure 5.14).

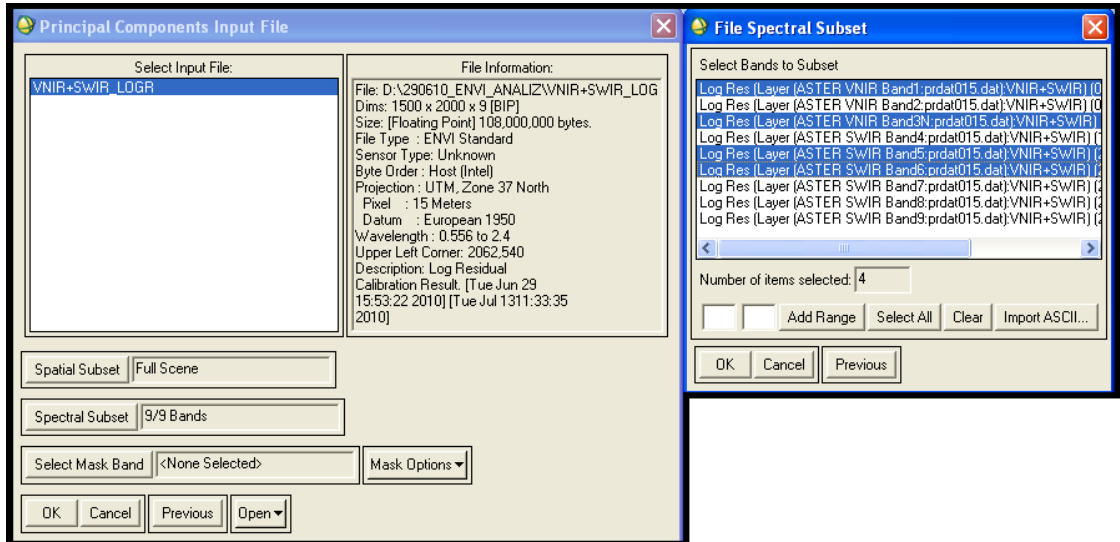


**Figure 5.14** Selection of appropriate bands to perform PCA.

The next step is viewing the statistics file which gives the eigenvector values calculated and illustrated at the bottom of this file (Figure 5.15). These eigenvector values are used to determine the PC will generate Illite3 endmember map.

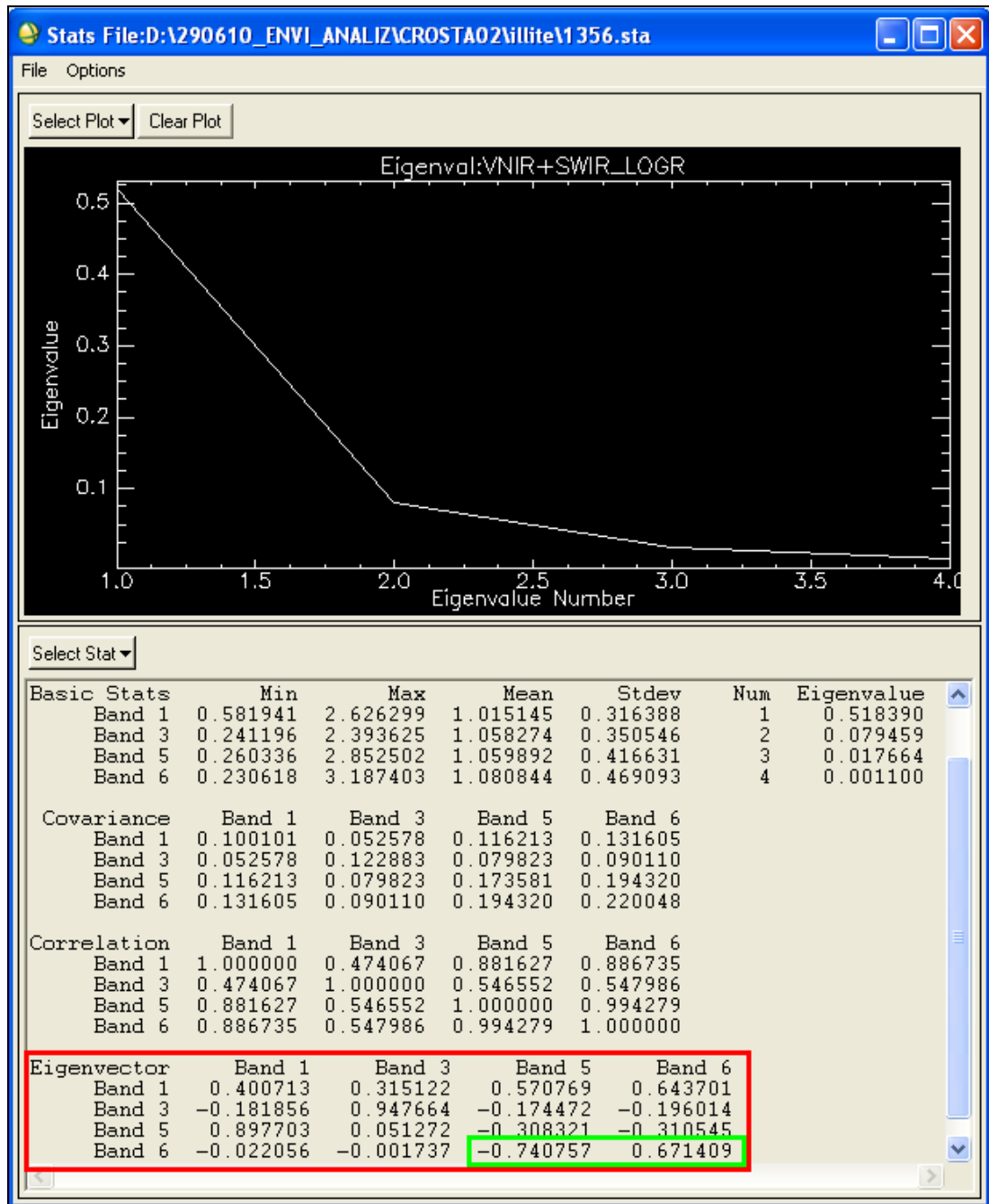


**Figure 5.15** The statistics file showing the eigenvalues is displayed. This statistics allow selecting the appropriate PC. Green rectangle shows the highest opposite standings.

In order to select the PC, an examination of the magnitude and sign of the eigenvectors is required. The statistics data of eigenvectors indicates that PC4 have high and opposite magnitudes which must be selected as the PC for Illite3 (Figure 5.16). Note rows refer to the PCs whereas columns to the selected bands.

The appropriate threshold is computed using  $(\text{Mean}) + (2 \times \text{Standard Deviation})$  formula as stated. Displaying the statistics file (Figure 6.11.) for the selected PC, i.e., PC4, this formula can be calculated. According to the values, the threshold value becomes  $(0) + (2 \times 0.033) = 0.66$ .

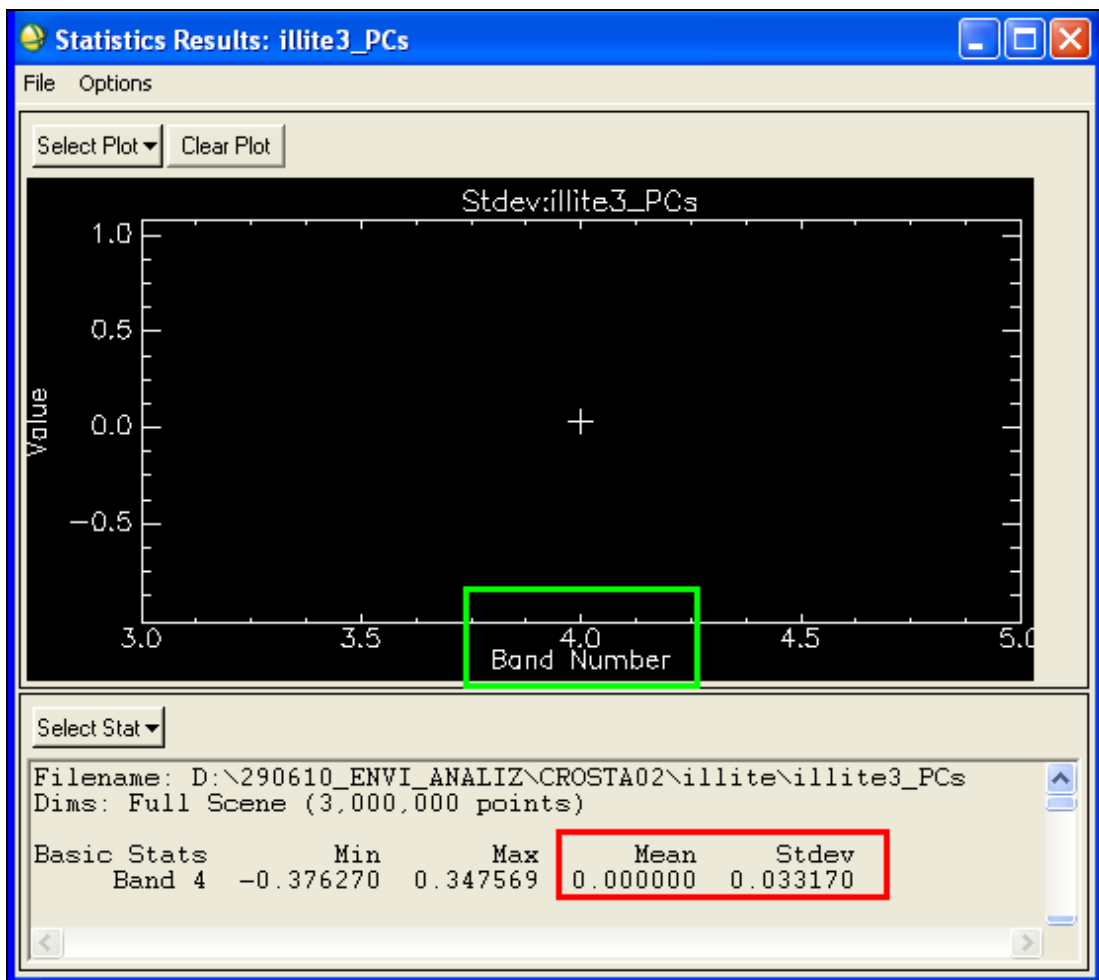


**Figure 5.16** Mean and standard deviation values of PC4.

This threshold value is used for interactive stretching application on the generated image (Figure 5.17). Obviously the image file is displayed previously.

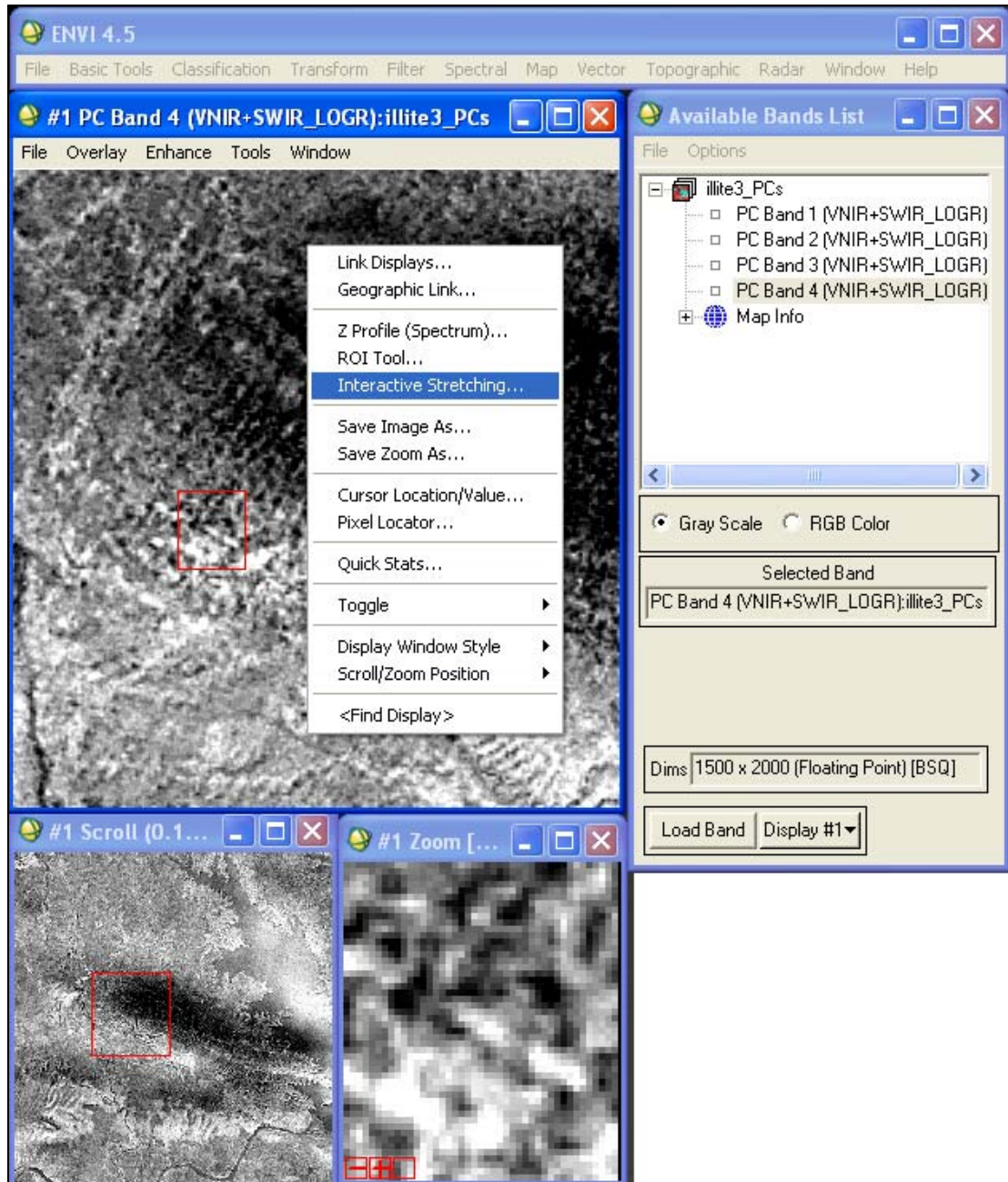


**Figure 5.17** Interactive stretching operation which allows to apply the threshold value to the generated image before mapping the particular feature.

PC transformation for illite3 is shown in Figure 5.17. Eigenvector statistics of input bands show that PC4 shows a high negative value in band 8 (-0.7407) and high positive value in band 9 (0.6714). The positive sign of band 8 and negative sign of band 9 indicate that an illite3 mineral is mapped as dark pixels. By using band math function, PC4 image is multiplied by minus 1 (negation), so that illite3 is displayed by bright pixels in the image (Figure 5.18).

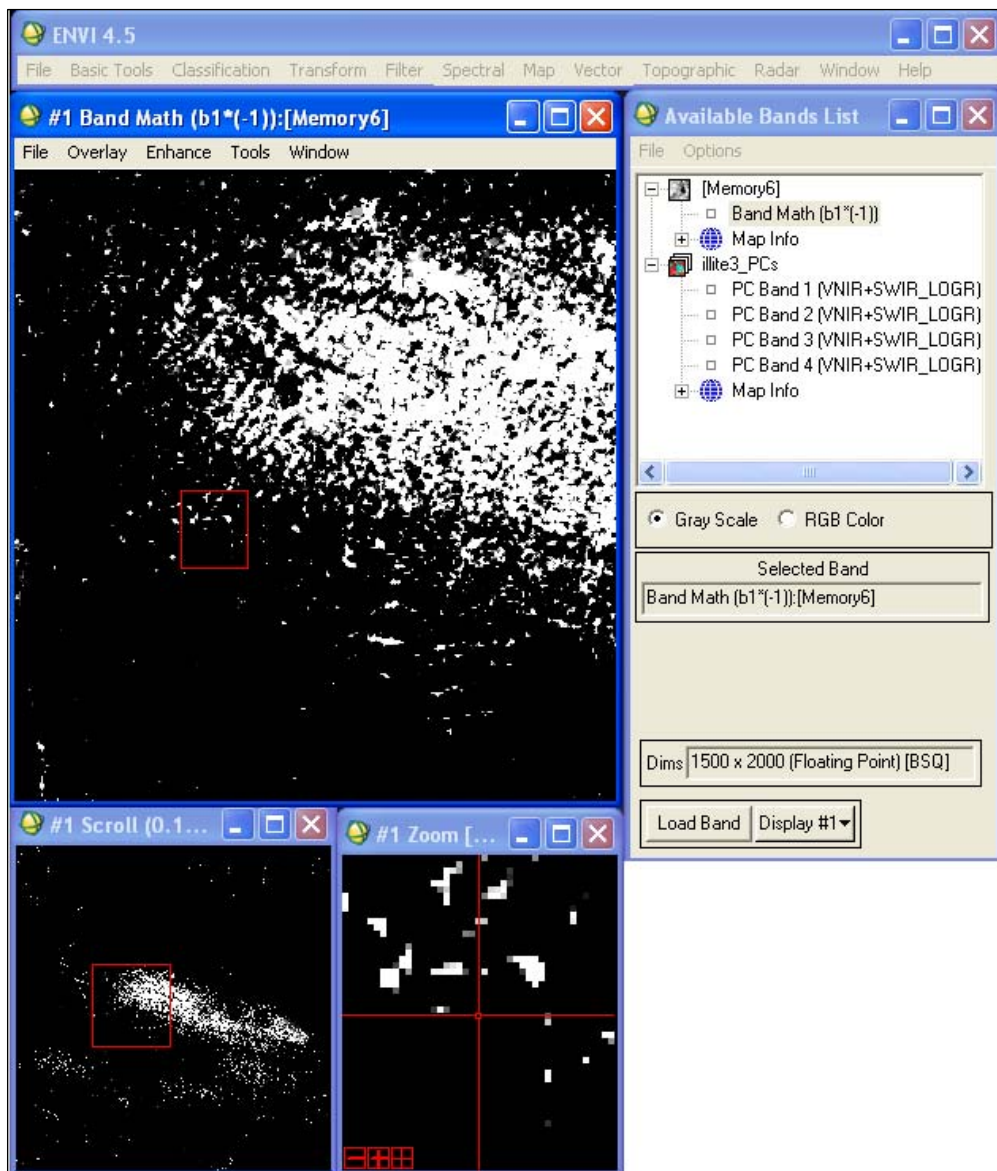


**Figure 5.18** This map shows the distribution of Illite3 endmember over Gemrik Anticline. The red boxes show the vicinity of, whereas the cross points the reference valley.

Applying all the steps listed, the illite map of Gemrik Anticline is generated (Figure 5.19.). The same steps were applied and the maps are generated for kaosmectite, desert varnish, dipyre and montmorillonite, respectively. HC microseepage map is shown finally.

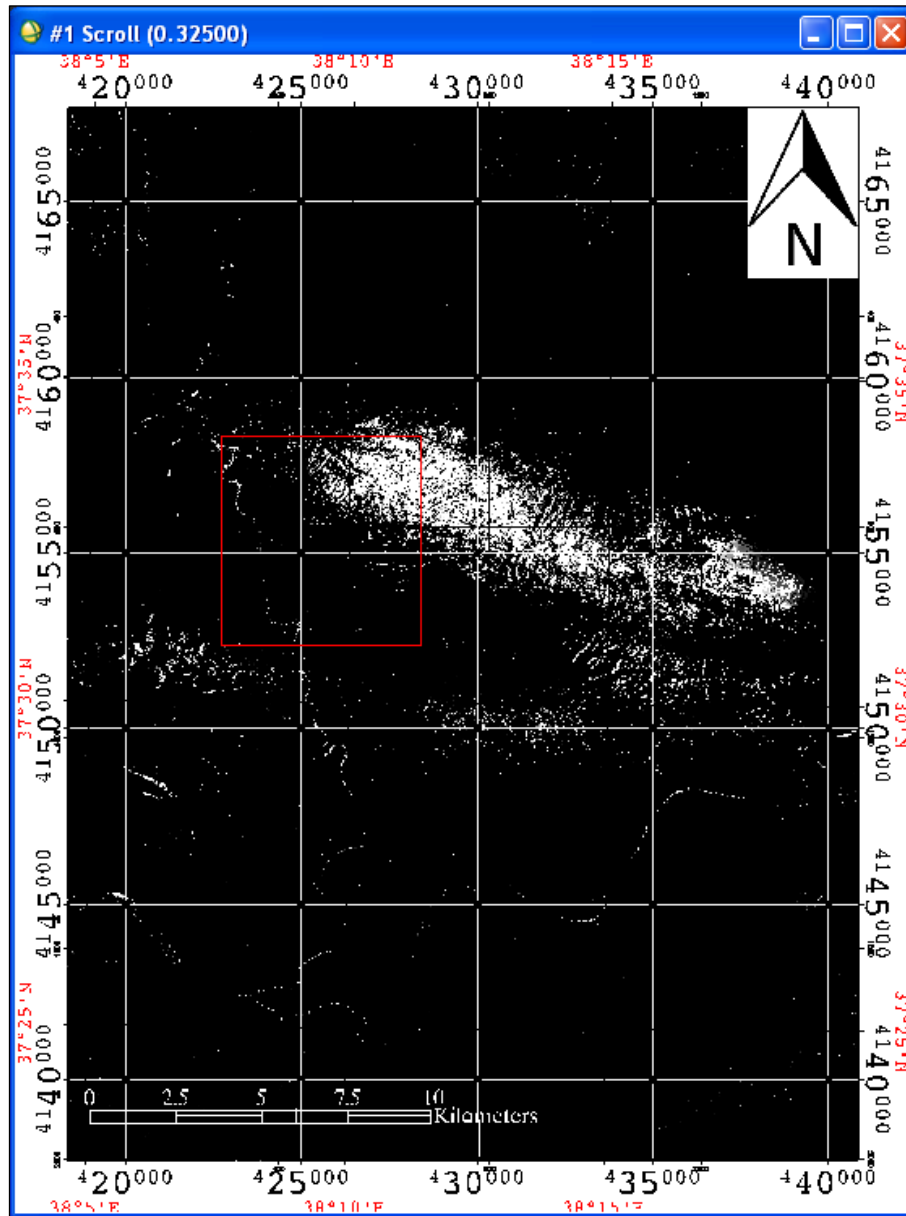


**Figure 5.19** The Illite map of Gemrik Anticline with the necessary parameters. Illite is more abundant especially in the north-east flank of Gemrik Anticline, which supports HC microseepage phenomena of illite accumulation in non-anomalous regions.

Kaomectite5 is another endmember gathered after the analyses. Kaomectite (kaolinite+smectite) is a known endmember acquired after analyses considering previous studies on HC microseepage detection (Kahn, 2008). They found that the samples contain up to 27 % of kaomectite throughout the analyses. In order to map kaomec5 endmember, its reflectance-wavelength graph is overlapped with ASTER bands to select appropriate band combination. ASTER bands 1,3,6,7 are selected. To define the principle component, statistic file is displayed which illustrates the eigenvectors (Figure 5.20). After an examination through the magnitudes and signs of the eigenvectors, PC4 shows highest and opposite magnitudes which must be selected to map Kaomec5 endmember.

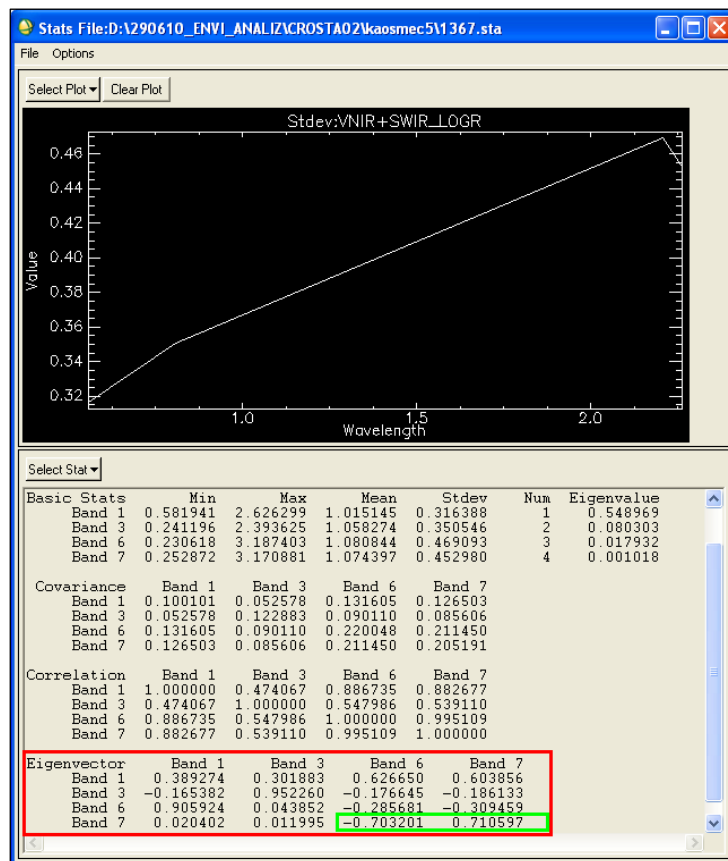


**Figure 5.20** Eigenvalues for Kaomec5. Green rectangle shows the highest opposite standings. PC4 is selected to map Kaomec5 endmember.

To compute the threshold value, the statistics file is illustrated for PC4 (Figure 5.21.). The threshold value is  $((0) + (2 \times 0.0319)) = 0.0638$ .

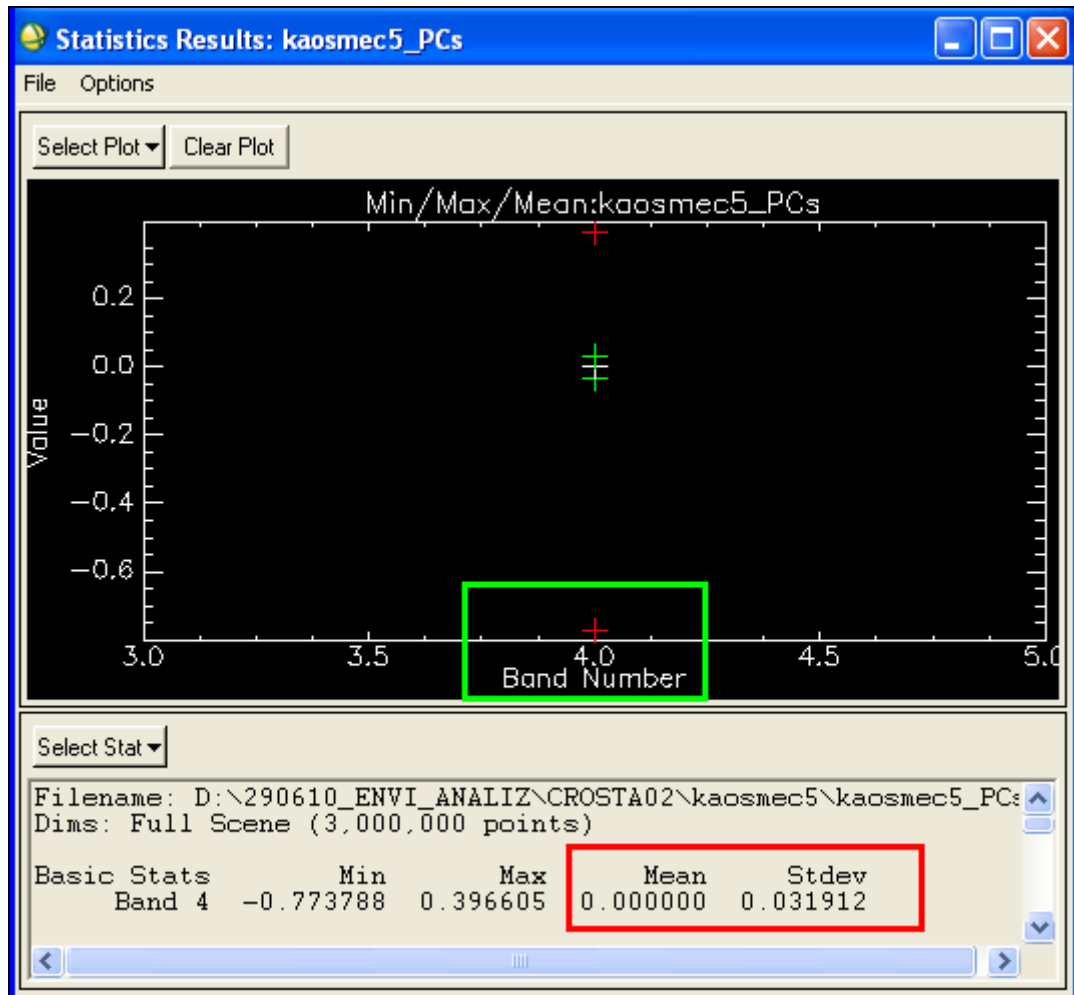


**Figure 5.21** Statistics file of PC4 showing mean and standard deviation values belonging to kaosmec5 endmember.

To stretch the image, threshold value is applied to PC4 image. The kaosmectite map generated for Gemrik Anticline is shown in Figure 5.22. It is important to state that kaosmectite accumulation is observed within the square which supports kaolinite occurrence over the HC microseepage zones.

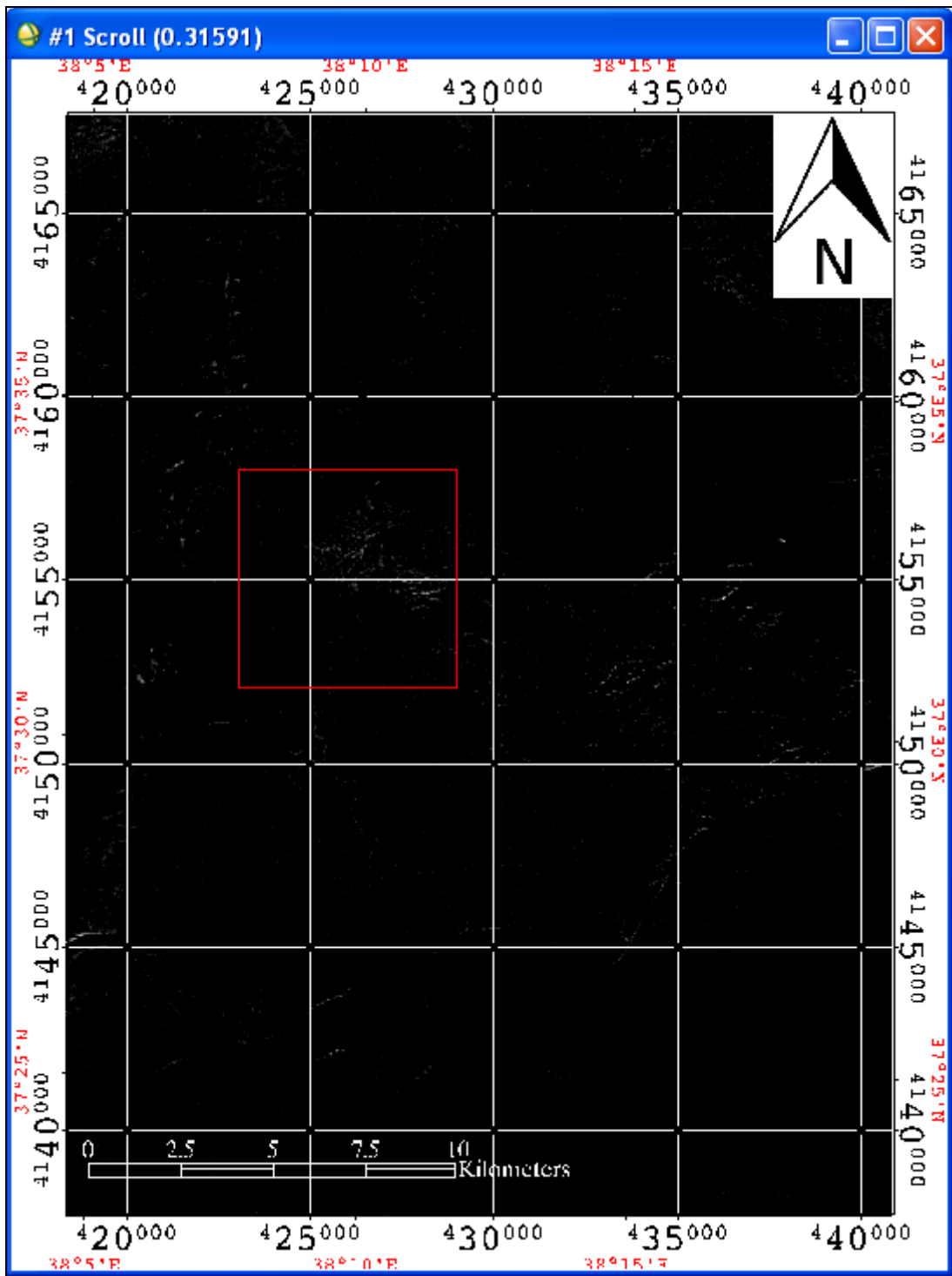


**Figure 5.22** Kaosmectite map. Red square shows the study area. Note the series of accumulation on the reference valley where HC microseepage is known.

"Desert varnish invariably consists of birnessite in intimate mixture with hematite and large amounts of clay minerals. The clays are generally of the illite-montmorillonite type with minor kaolinite, but in several samples this concentration ratio is reversed." ([http://speclab.cr.usgs.gov/spectral.lib06/ds231/DESCRIPT/C/des\\_varnish\\_entrada.html](http://speclab.cr.usgs.gov/spectral.lib06/ds231/DESCRIPT/C/des_varnish_entrada.html)). Desert varnish is clay in dominant. The clay minerals represent the clays found locally in the region where the varnish develops. In the clay layer, black manganese oxide (the mineral birnesite) and red iron oxide (the mineral hematite) add color. Desert varnish is a dark coating material in arid regions (Figure 5.23). The coating is composed dominantly of fine-grained clay minerals. Well-developed coatings can form in the splash zone of rivers in arid regions (<http://minerals.caltech.edu/files/varnish/index.html>).

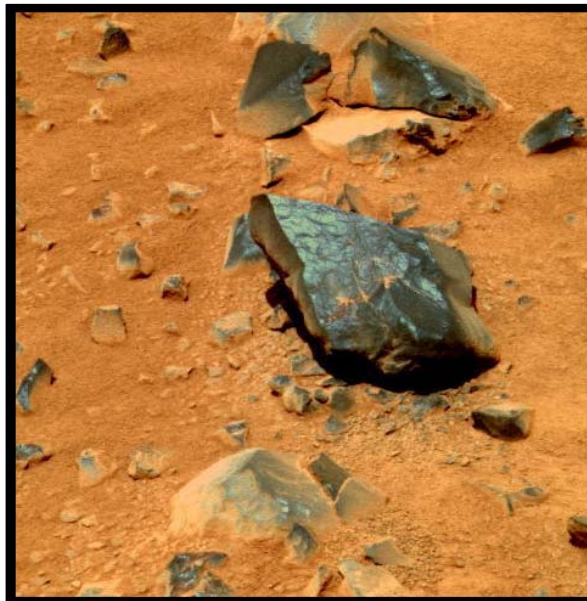


**Figure 5.23** Desert Varnish is a coating material which is not present in the plane of separation.

To map the distribution of Desert Varnish3 endmember throughout Gemrik Anticline, its reflectance curve is analyzed with ASTER bands together. After the analyses, ASTER bands 4,5,6,8 are selected to perform PCA. The statistics file showing the mean and standard deviation values to calculate the threshold value is given in Figure 5.24. Considering the high and negative standings, PC4 is selected to map desert varnish3 endmember.

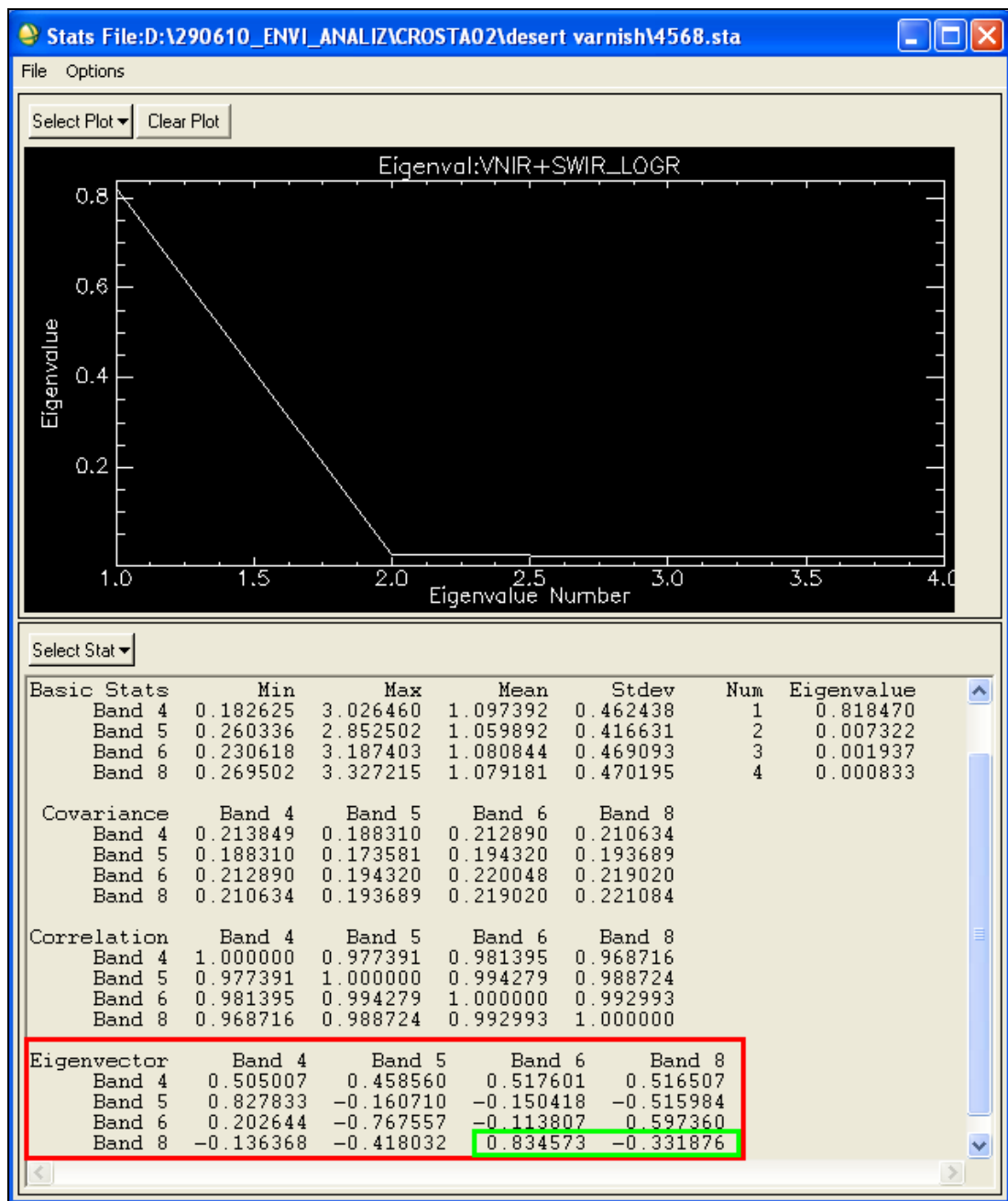


**Figure 5.24** Statistics show that PC4 has to be selected since it has the highest and negative values.

PC4 statistics file illustrate that the threshold value is 0.056. Applying interactive stretching to the PC4 image, the map of desert varnish3 over the anticline is generated as shown in Figure 5.25. The south-west flank of Gemrik Anticline shows

HC microseepage and this portion is extending in the south-east part of the red box. Indeed, the reference valley locates in the south-west end of the anticline.

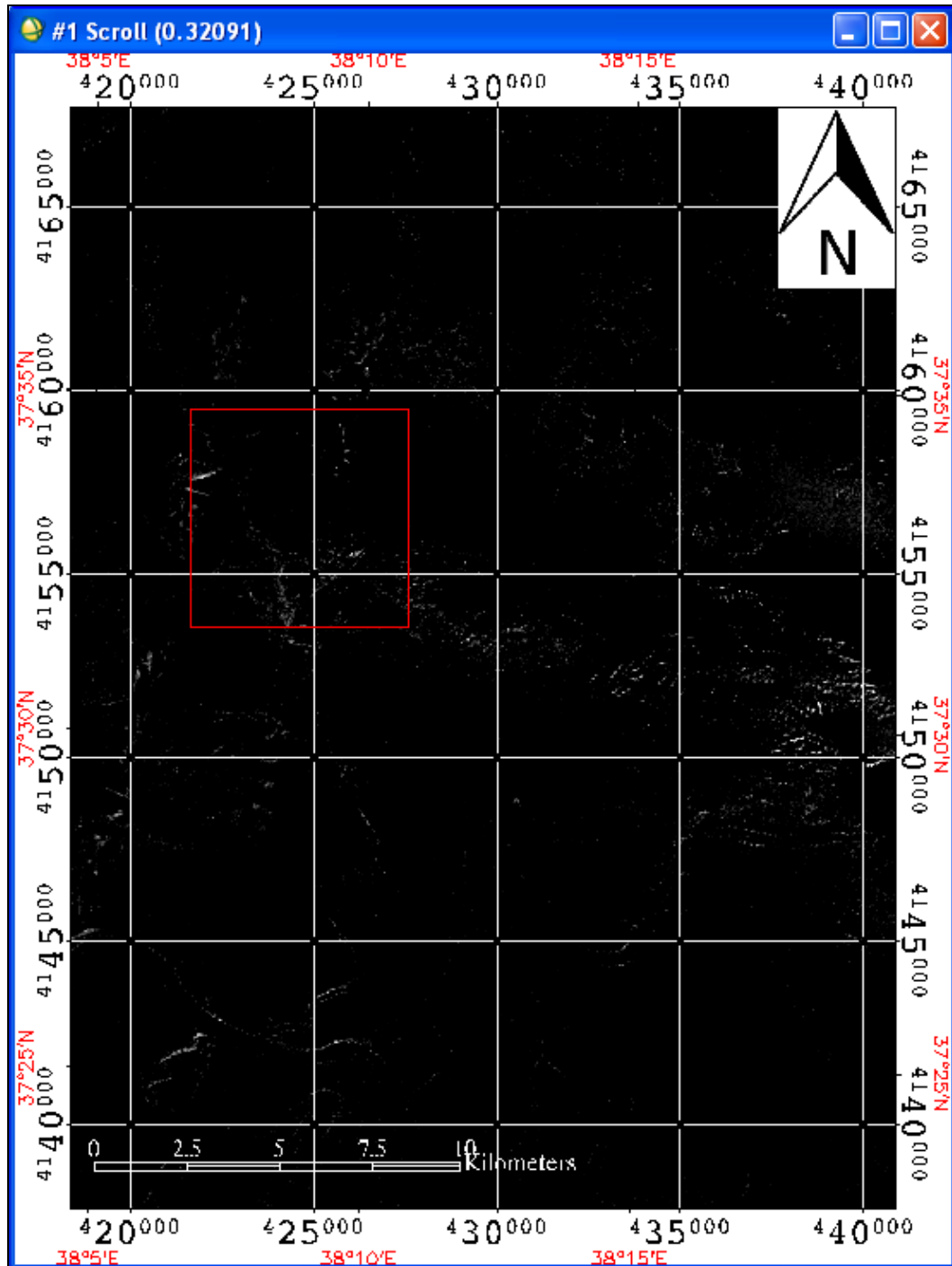


**Figure 5.25** The distribution of desert varnish3 endmember over Gemrik Anticline. Previous studies showed that desert varnish is found more in anomalous regions than it does in non-anomalous locations.

Dipyre is another mineral offered by SPECMIN Software during the analyses. It is not stated in the literature as a surface indicator linked to HC microseepages but it is documented in this thesis since results contain dipyre in a considerable amount. Dipyre can simply be defined as “*a mineral of the scapolite group; - so called from the double effect of fire upon it, in fusing it, and rendering it phosphorescent*” (<http://www.encyclo.co.uk/webster/D/71>).

The distribution of Dipyre mineral over Gemrik Anticline is mapped using ASTER bands 1,5,6,8. According to the statistics file shown in Figure 5.26, PC4 is selected due to the loadings. The image is negated considering the absorption and reflectance characteristics in band 6 and 8, respectively. At this point, although PC3 looks preferring as the principle component image for that it has the highest and opposite loadings, that image is not selected. The reason is that the three negative and one positive PC3 loadings are not overlapping with the reflectance (high) and absorption (low) order of the spectral curve belonging to Dipyre mineral.

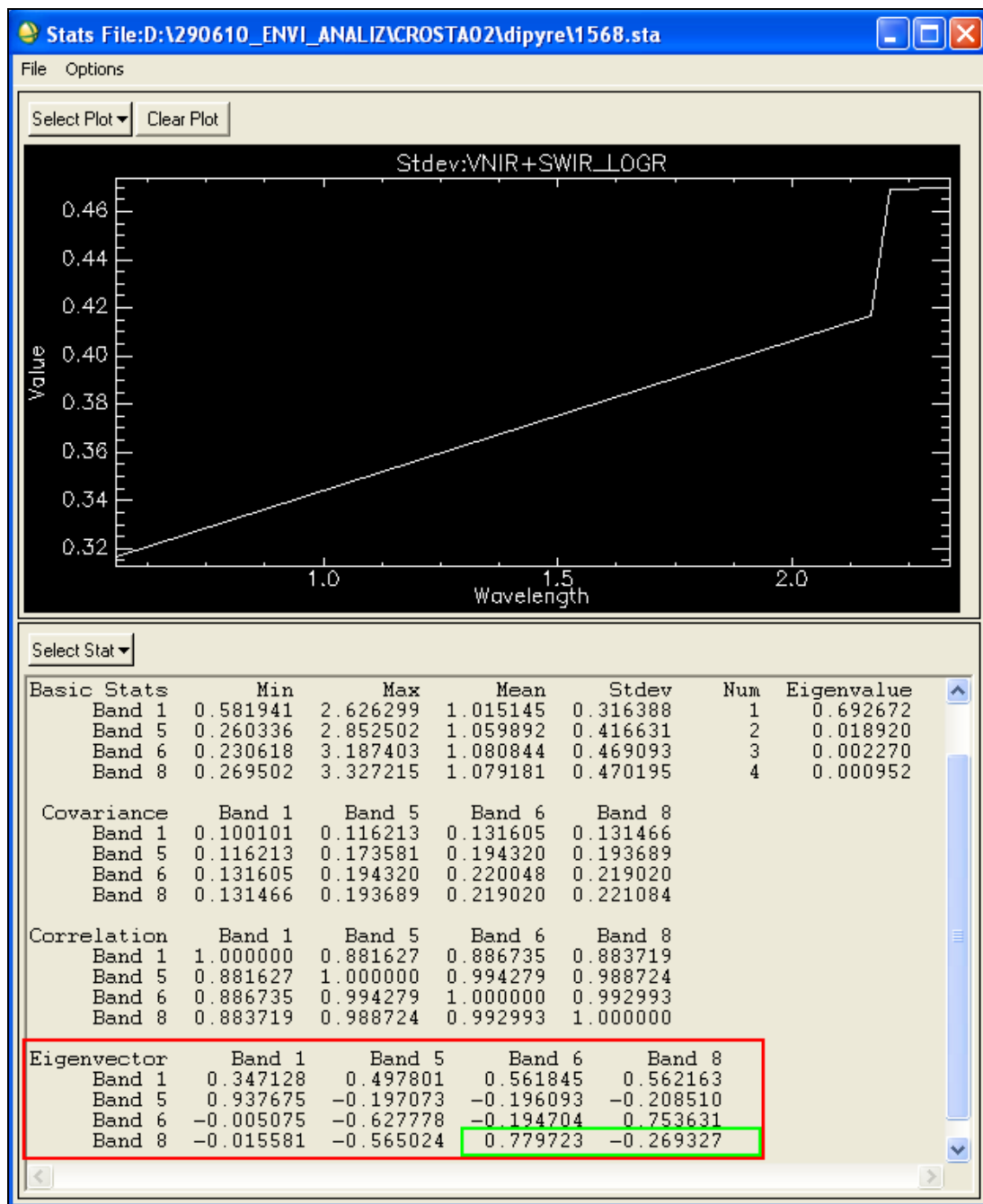


**Figure 5.26** PC4 is chosen to map Dipyre Mineral for the indicated loadings.

The threshold value applied in the stretching operation is 0.0616. The final image showing the prospect points for Dipyre mineral is shown in Figure 5.27.

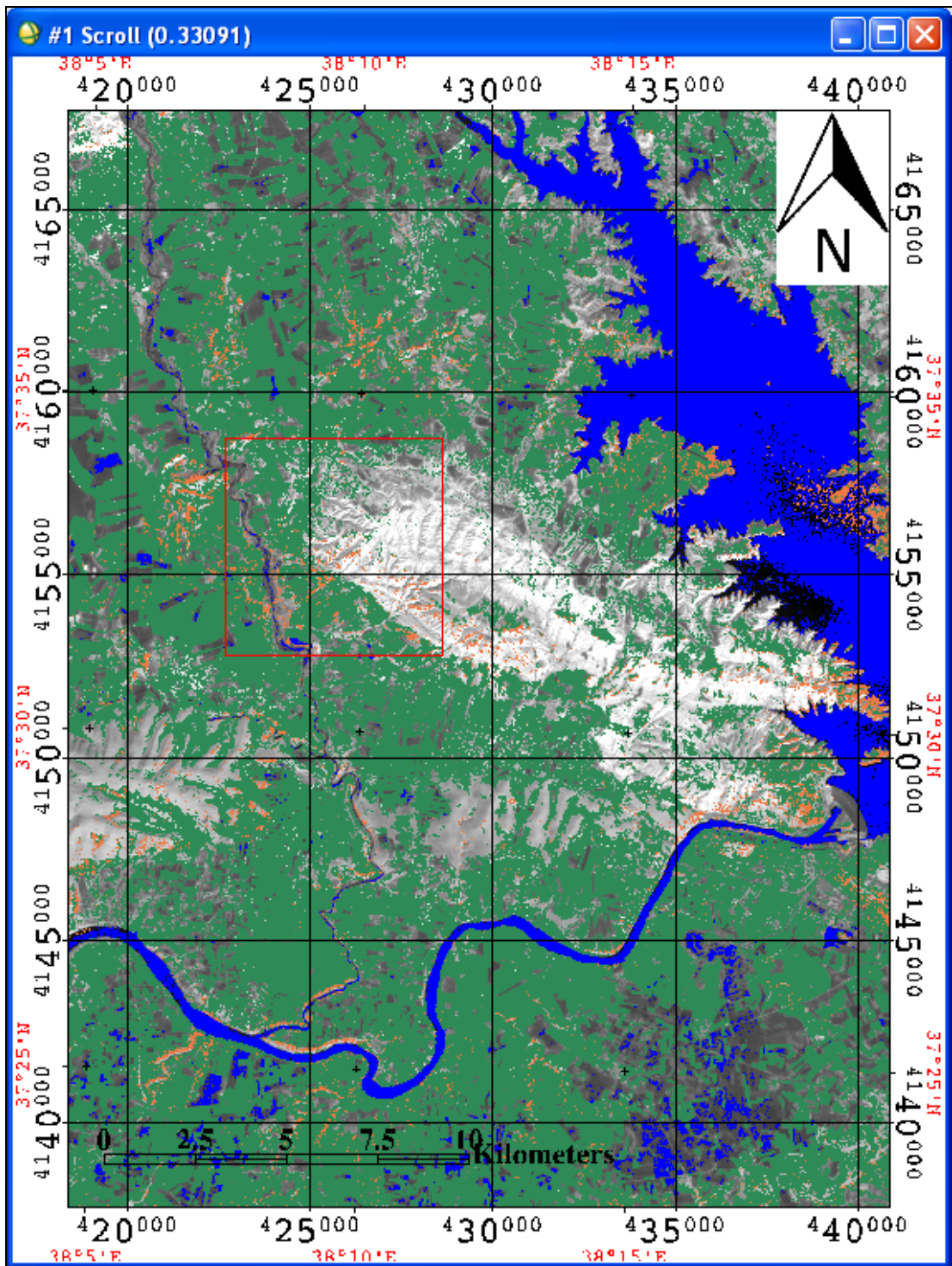


**Figure 5.27** The Dipyre map over Gemrik Anticline with vegetation (green), water+cloud (blue) masking. Its distribution shows similarity to that of HC anomalous regions.

The relation between distributions of Dipyre and HC microseepage has not been documented. However, results in this study shows that Dipyre mineral abundance increases with the presence of HC microseepage. When vegetation (green), water+cloud (blue) masks are applied, Dipyre prospects in the south west flank of Gemrik Anticline which is also the HC anomalous region as previously stated.

Montmorillonite is smectite clay which is an alteration product of mafic igneous volcanic rocks, particularly tuffs and volcanic ash (Grim and Güven, 1978). Montmorillonite (pure smectite) map is generated using ASTER bands 4,6,7,8. Loading the statistics file for the selected bands, PC3 becomes the principle component representing the eigenvectors comprehensively (Figure 5.28). The spectral characteristics show high, low, high, high order.

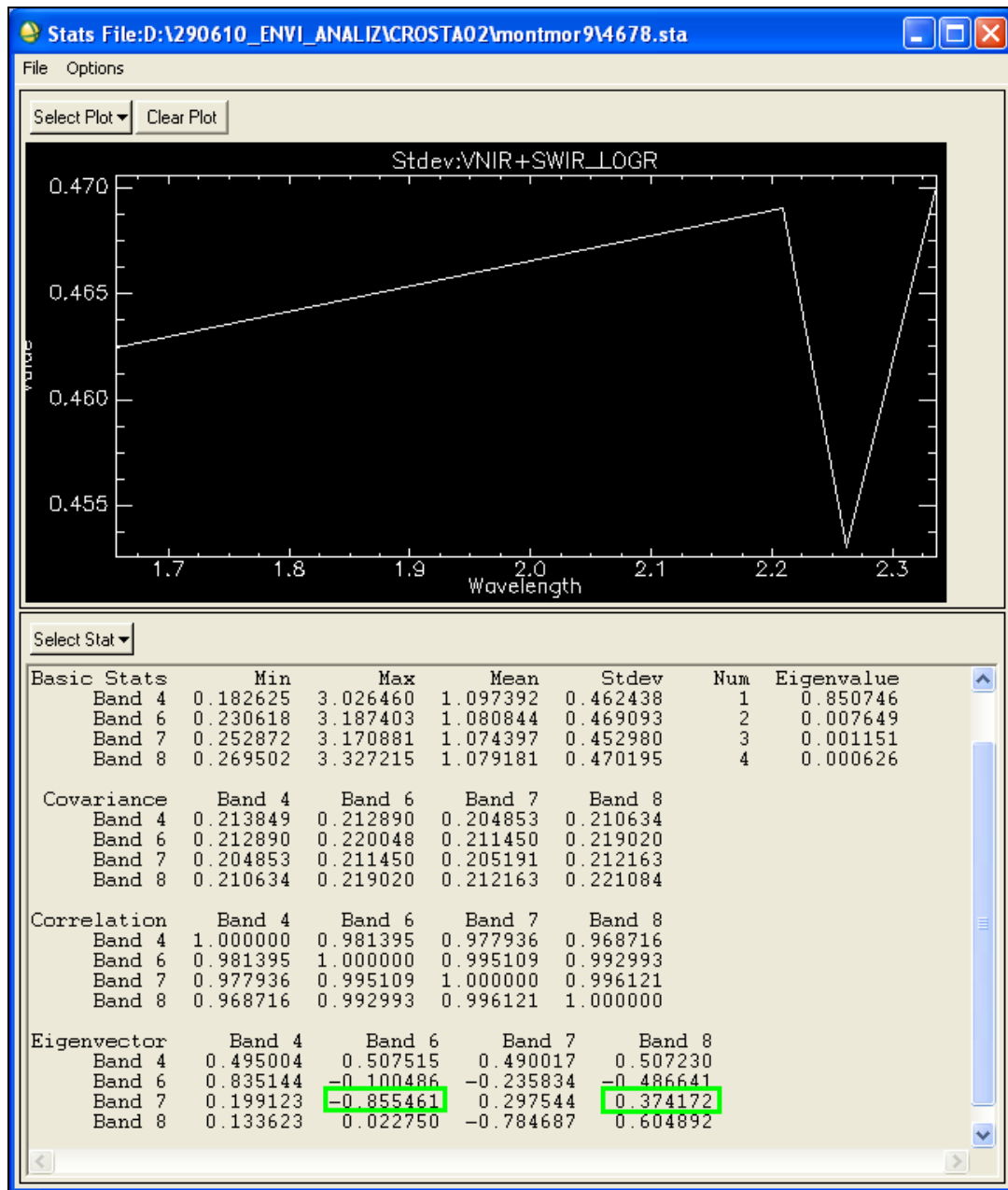
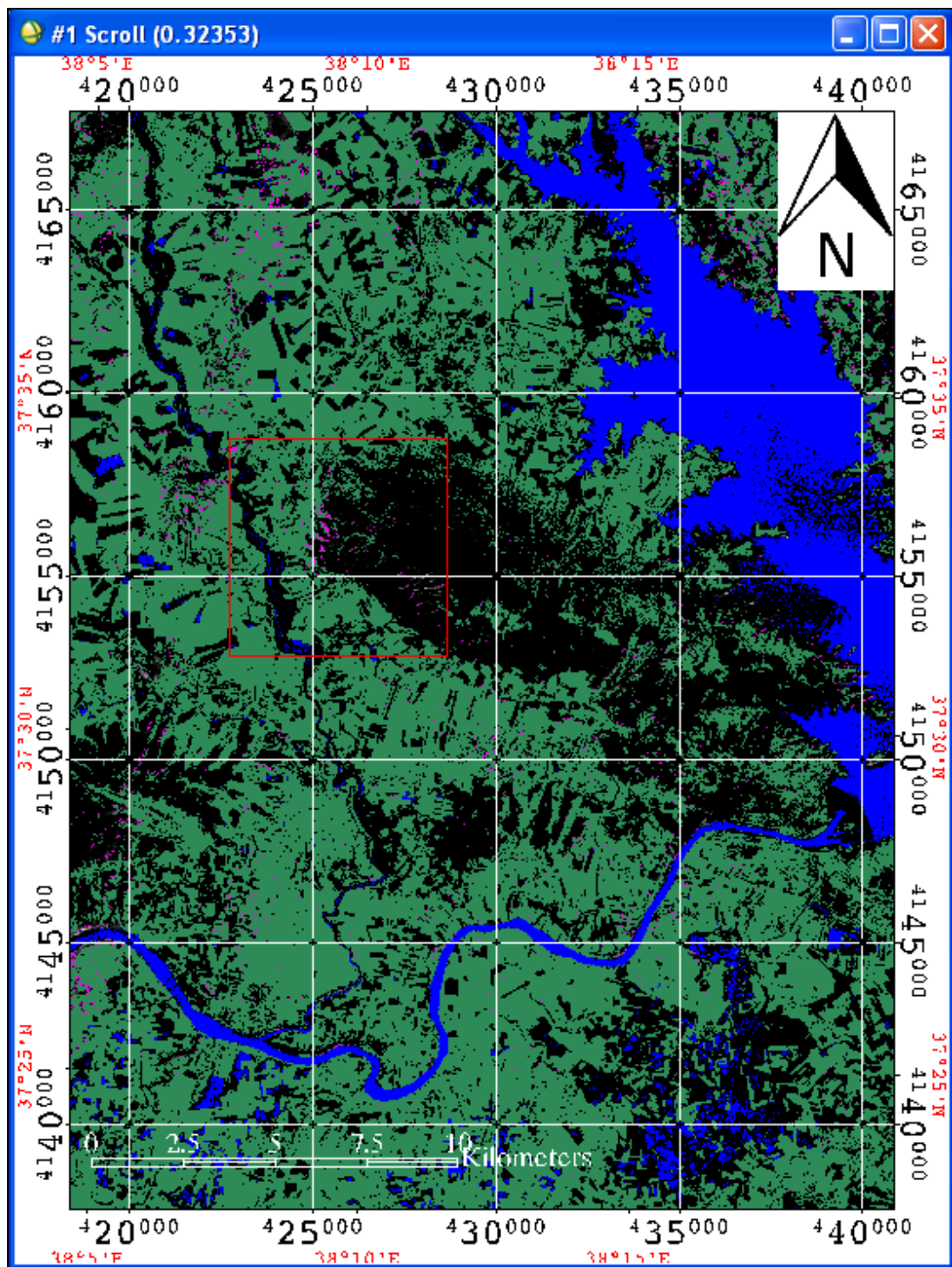


Figure 5.28 Statistics file of Montmor9 endmember.

Threshold value becomes 0.0678 and the resultant map for Montmor9 endmember on Gemrik Anticline is illustrated in Figure 5.29. Besides, vegetation (green), water+cloud (blue) masks are applied to the image. It is also documented that montmorillonite is more abundant in anomalous regions than places without HC microseepage (Kahn, 2006).



**Figure 5.29** Montmorillonite mineral (pink) distribution over Gemrik Anticline with vegetation (green), water+cloud (blue) masking. The extent of the Montmor9 endmember shows similarity to that of anomalous regions.

Maps generated showed that the distributions of particular minerals are supportive clay mineral alterations for HC microseepage. From this point, the map of HC microseepage over Gemrik Anticline is generated based on the spectral characteristics of hydrocarbons and data gathered from field since there is no direct offering by any of the spectral libraries. Previous studies have shown that hydrocarbon bearing materials demonstrate absorption maxima at 1.73 $\mu\text{m}$  and 2.31 $\mu\text{m}$  (Kühn et al., 2003). Moreover, hydrocarbon material shows reflectance characteristic at 2.145 $\mu\text{m}$ . and additional absorption features are documented at 1.155  $\mu\text{m}$  and 1.190 $\mu\text{m}$  (Cloutis, E.A., 1989, Smailbegovic et al., 2009). An important feature is flattening of clay-mineral absorption at 2200 $\mu\text{m}$  due to HC pollutant.

Based on the spectral characteristics of hydrocarbons, ASTER bands 1,4,5,8 are selected to display reference valley whose HC content is known and hence to generate the map over Gemrik Anticline. The threshold value is 0.164 when PC3 image is selected. The HC microseepage map of Gemrik Anticline is shown in Figure 5.30. The image is masked to avoid confusion.

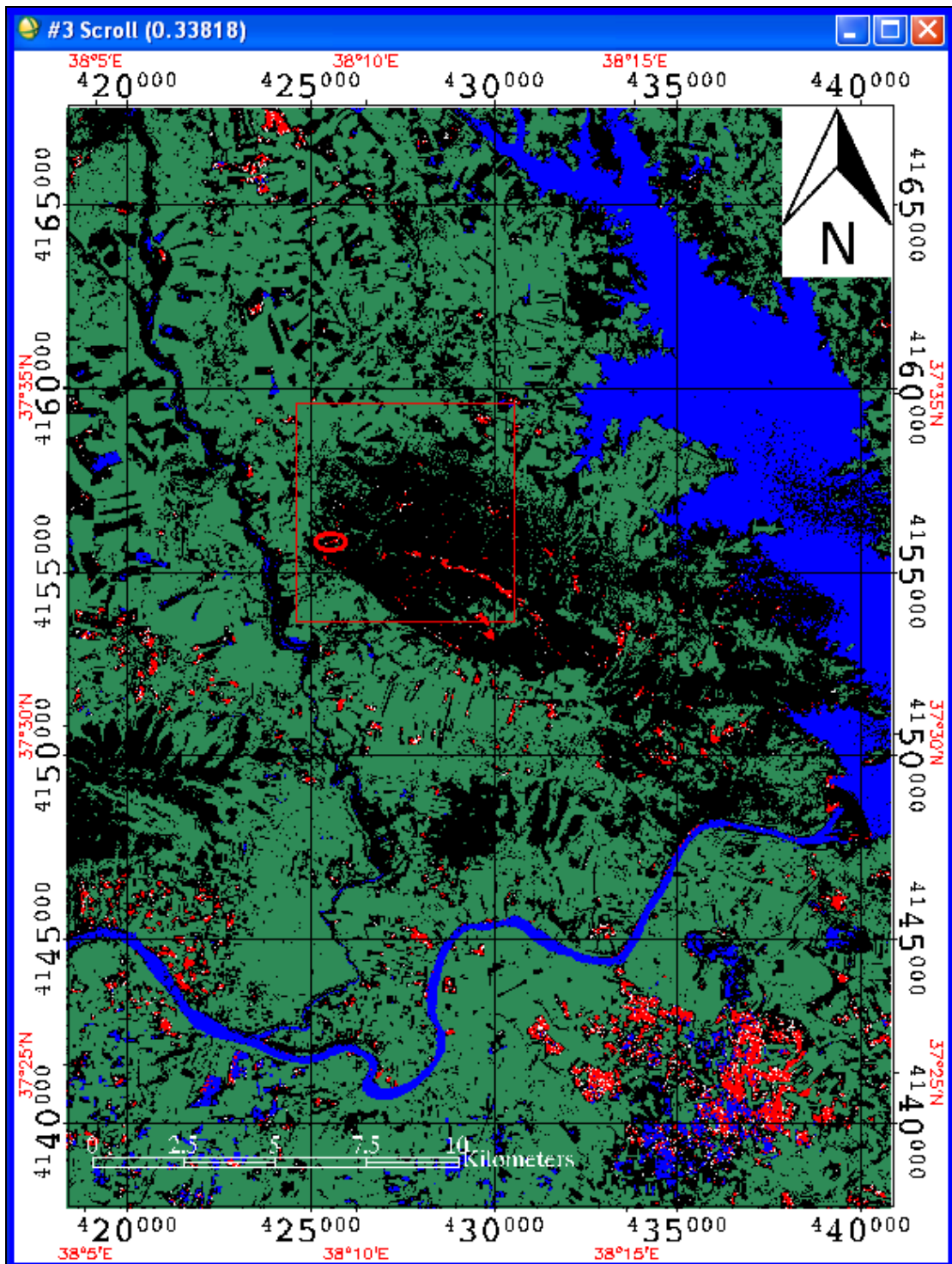


**Figure 5.30** Hydrocarbon microseepage map of Gemrik Anticline with vegetation (green), water+cloud (blue) masking. Red ellipse pin point indicates the reference valley.

### 5.2.3 Field Data

This section explains the data gathered from field. In detail, the issues of sample collection with their pyrolysis measurements and the spectral analysis of the collected samples in SPECMIN Software are explained.

#### 5.2.3.1 Sample Collection and RockEval Pyrolysis

Locations of the samples are shown in Figure 5.31. They were collected along the reference valley considering spatial distribution of HC microseepages.

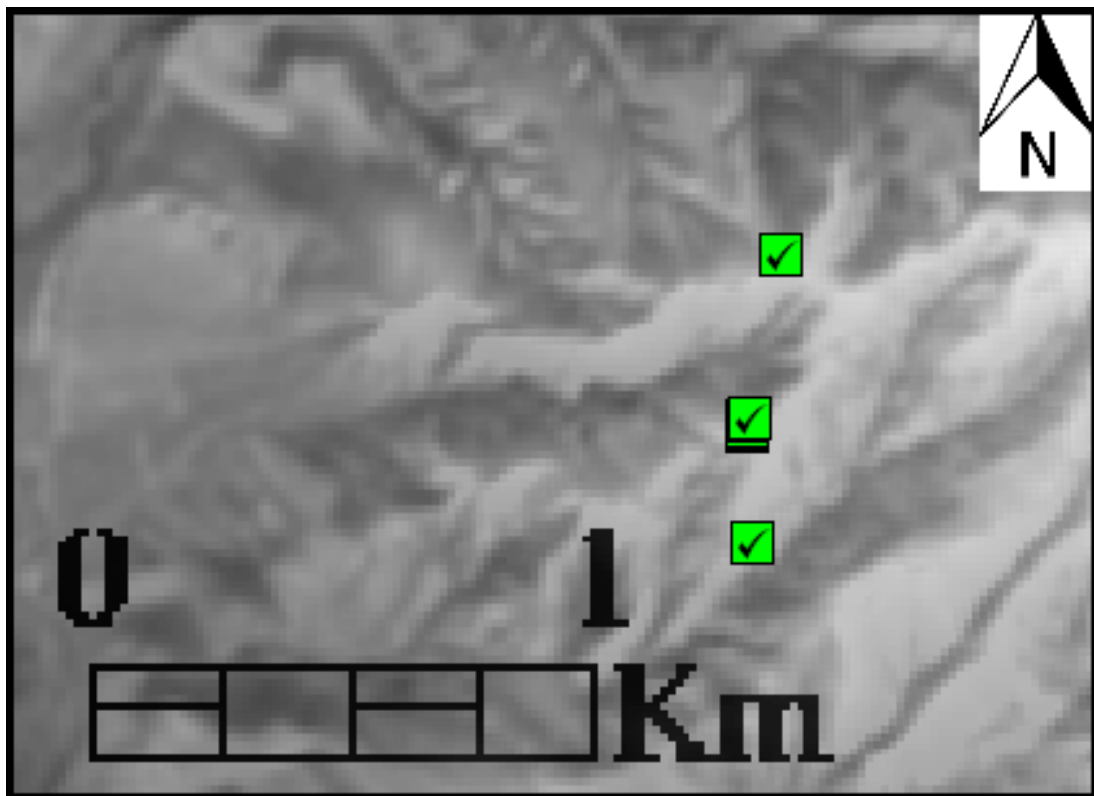


**Figure 5.31** ASTER Band 3 Image of study area is overlain by the generated DEM with 60% transparency. Placemarks show the HC-bearing samples. Note that the accumulated check signs in the middle show the reference valley.

The positions of samples are measured using Magellan SporTrak Color GPS (Global Positioning System). Table 5.2 shows the positions and descriptions of samples taken from the study valley.

**Table 5.2** The positions of samples collected from the reference valley

Place No	Northing	Easting	Description	Formation
1	4155800	425706	Weathered	Germav
2	4155806	425708	Fresh	Germav
3	4155813	425707	Fresh	Germav
4	4155824	425708	Weathered	Germav
5	4155826	425711	Weathered	Germav
6	4155582	425719	Fresh	Germav
7	4156147	425771	Weathered	Germav
8	4156147	425771	Weathered	Germav

The performed pyrolysis analyses were conducted using RockEval device. Rock Eval pyrolysis is used to identify the type and maturity of organic matter and to detect petroleum potential in sediments. Rock Eval pyrolysis is done using the Delsi-Nermag Rock Eval II Plus Total Organic Carbon (TOC) module. The Rock Eval (RE) pyrolysis method consists of a programmed temperature heating (in a pyrolysis oven) in an inert atmosphere (helium) of a small sample (~100 mg) to quantitatively and selectively determine;

1. The free hydrocarbons contained in the sample
- 2 The hydrocarbon- and oxygen-containing compounds (CO<sub>2</sub>) that are volatilized during the cracking of the unextractable organic matter in the sample (kerogen).

In summary, the four basic parameters obtained by pyrolysis are as follows:

**S<sub>1</sub>** = The amount of free hydrocarbons (gas and oil) in the sample (in milligrams of hydrocarbon per gram of rock). If  $S_1 > 1$  mg/g, it may be indicative of an oil show.

**S<sub>2</sub>** = The amount of hydrocarbons generated through thermal cracking of nonvolatile

organic matter.  $S_2$  is an indication of the quantity of hydrocarbons that the rock has the potential of producing should burial and maturation continue. This parameter normally decreases with burial depths  $>1$  km.

$S_3$  = The amount of  $CO_2$  (in milligrams  $CO_2$  per gram of rock) produced during pyrolysis of kerogen.  $S_3$  is an indication of the amount of oxygen in the kerogen and is used to calculate the oxygen index (Figure 5.32). Contamination of the samples should be suspected if abnormally high  $S_3$  values are obtained. High concentrations of carbonates that break down at lower temperatures than  $390^\circ C$  will also cause higher  $S_3$  values than expected.

**Tmax** = the temperature at which the maximum release of hydrocarbons from cracking of kerogen occurs during pyrolysis (top of  $S_2$  peak). Tmax is an indication of the stage of maturation of the organic matter.

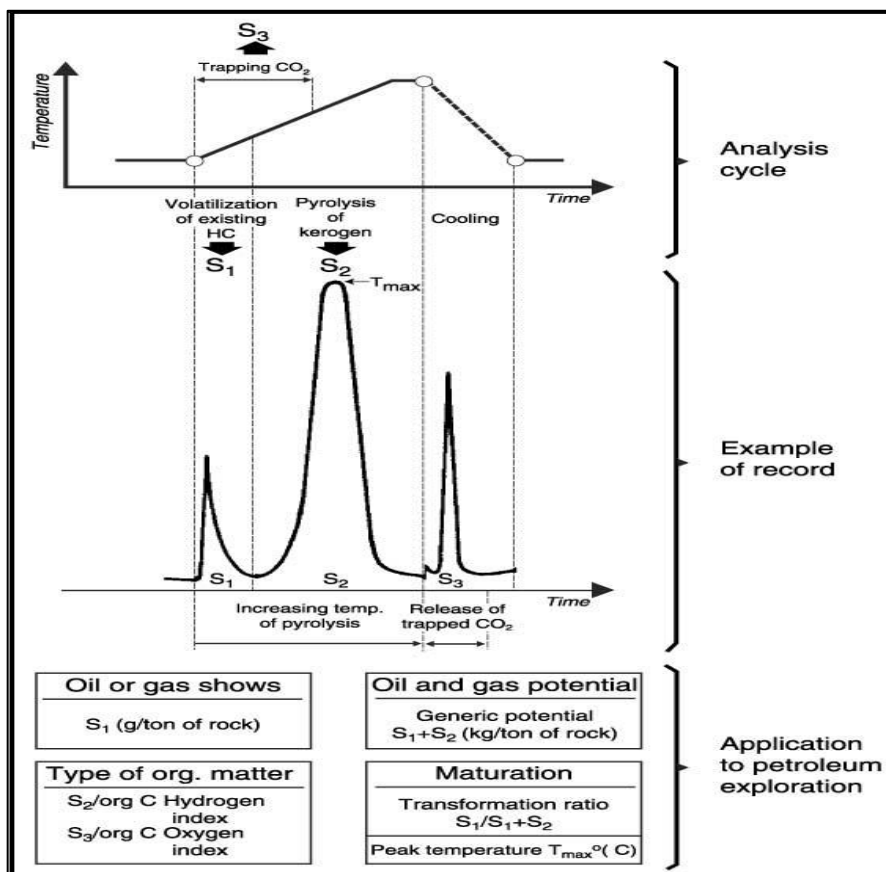


Figure 5.32 Basic parameters obtained by pyrolysis.

The type and maturity of organic matter in petroleum source rocks can be characterized from Rock Eval pyrolysis data using the following parameters:

**HI** = hydrogen index ( $HI = [100 \times S2]/TOC$ ). HI is a parameter used to characterize the origin of organic matter. Marine organisms and algae, in general, are composed of lipid- and protein-rich organic matter, where the ratio of H to C is higher than in the carbohydrate-rich constituents of land plants. HI typically ranges from ~100 to 600 in geological samples.

**OI** = oxygen index ( $OI = [100 \times S3]/TOC$ ). OI is a parameter that correlates with the ratio of O to C, which is high for polysaccharide-rich remains of land plants and inert organic material (residual organic matter) encountered as background in marine sediments. OI values range from near 0 to ~150.

**PI** = production index ( $PI = S1/[S1 + S2]$ ). PI is used to characterize the evolution level of the organic matter.

**PC** = pyrolyzable carbon ( $PC = 0.083 \times [S1 + S2]$ ). PC corresponds to carbon content of hydrocarbons volatilized and pyrolyzed during the analysis.

Maturation of the organic matter can be estimated by Tmax range. Tmax = 400°-430°C represents immature organic matter; Tmax = 435°-450°C represents mature or oil zone; Tmax > 450°C represents the overmature zone.

Rock Eval pyrolysis is not normally used to make real-time drilling decisions because of the lengthy sample preparation, running, and interpretation time ([http://www-odp.tamu.edu/publications/tnotes/tn30/tn30\\_11.htm](http://www-odp.tamu.edu/publications/tnotes/tn30/tn30_11.htm)).

These samples were then analyzed in geochemical point of view. Pyrolysis results prove that all of the samples are possessing HC. Table 5.3 shows geochemical analysis results of the samples.

**Table 5.3** RockEval results showing TOC\_RE, S1 and TMAX values.

Sample No	Type	Formation	TOC_RE	S1	S2	S3	TMAX	HI	OI	PI
1	Hand Spec.	Germav	5,74	3,95	34,25	0,76	426	597	13	0,1
2	Hand Spec.	Germav	2,99	1,07	16,15	0,52	429	540	17	0,06
3	Hand Spec.	Germav	3,19	0,99	16,48	0,7	428	517	22	0,06
4	Hand Spec.	Germav	3,29	1,2	17,54	0,6	427	533	18	0,06
5	Hand Spec.	Germav	3,7	2,02	21,22	0,52	426	574	14	0,09
6	Hand Spec.	Germav	2,92	1,47	15,53	0,48	426	532	16	0,09
7	Hand Spec.	Germav	6,51	2,33	38,25	1,53	425	588	24	0,06
8	Hand Spec.	Germav	5,98	1,23	32,48	2,39	422	543	40	0,04

Considering the TOC (Total Organic Carbon) values shown in table 5.3., it can be inferred that the all samples have HC content since every TOC value is more than 1. S1 values, on the other hand, indicate oil show since the measurements are bigger than 1 mg/g. Tmax°(C) results are indicators of the stage of maturation for the organic matter. If the temperature value is equal or bigger than 430°(C), it is an indicator of a mature stage. At this point, Tmax°(C) values range between 422 and 429 which are close to mature oil stage boundary.

### 5.2.3.2 Analyses of Samples in SPECMIN Software

The spectral signatures of eight collected samples are measured using ASD Field Spectrometer in MTA laboratory. All of the surfaces that show difference are spectrally measured. ASD spectrometer uses a directional light source and fiber optic probe to collect light. ASD FieldSpec® Pro is a portable spectrometer designed for field use with a sampling interval 2 nm and a spectral resolution of 10 nm. It covers a spectral range from 350 to 2500 nm (VIS-SWIR region). Raw radiance data are corrected to reflectance by reference to a Spectralon® (barium sulfate – BaSO<sub>4</sub>) reflectance standard (Pekesin, 2005).

The spectral curves generated by the spectrometer are first viewed in ViewSpec Pro software to verify the curves (Figure 5.33.).

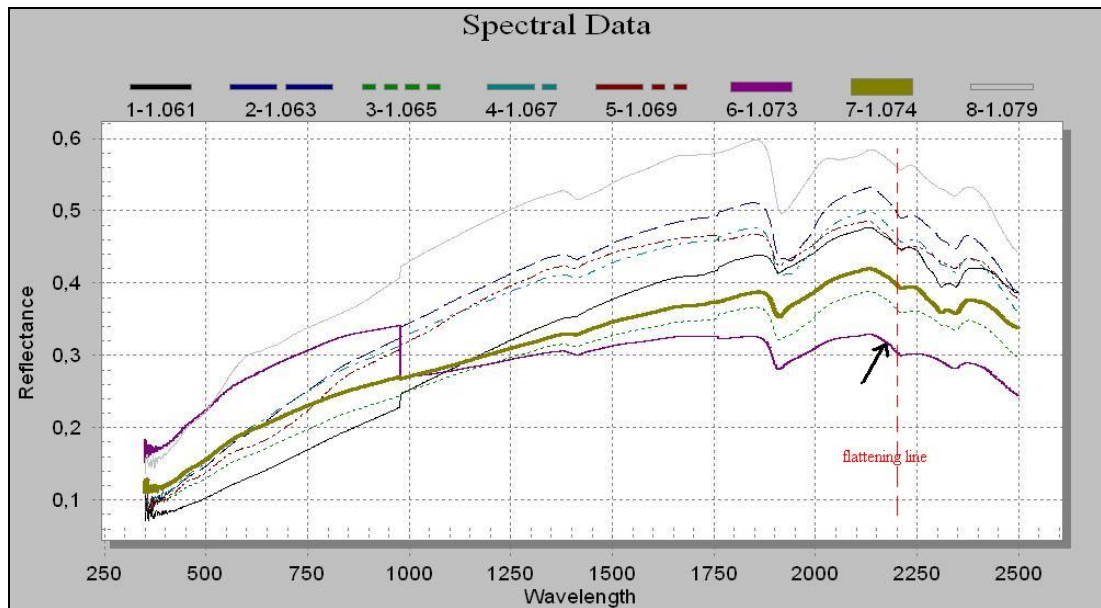


**Figure 5.33** Display of spectral data of eight samples generated from ASD Field Spectrometer in ViewSpec Pro Software.

Additional information here is a previous study which evaluates HC occurrences on the samples. It shows flattening characteristics of clay mineral absorption at 2200 nm on samples possess more than 30% of HC content by volume (Smailbegovic et al., 2009). Dashed line shows the flattening of clay mineral absorption at 2200 nm (Figure 5.11).

Resulting spectral curves are the input files for SPECMIN PRO 3.0 Software (Figure 5.34.). This program utilizes spectral curves of field data and overlaps (offers) some new curves from a defined library according to the absorption characteristic features. Before starting analyses, the user must select the library (Usgs, Jpl, ASD or Pima) that the software will use during the processes. The most likely curves are determined and taken into consideration as a constitutional mineral percentage belonging to that specific rock sample.

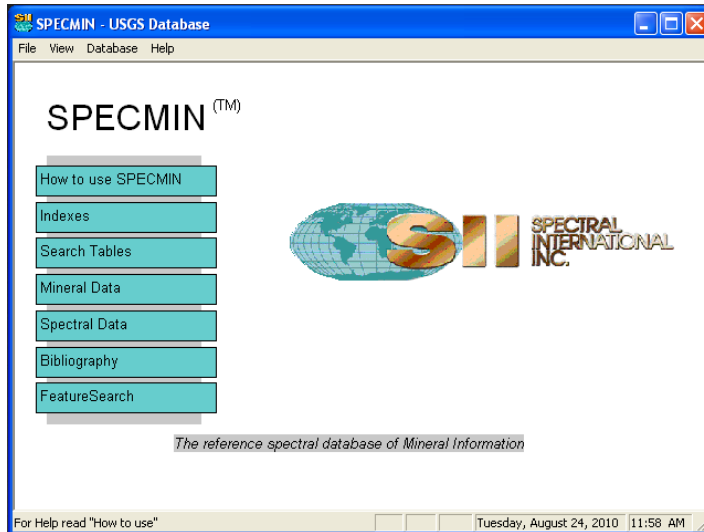


**Figure 5.34** The SPECMIN PRO 3.0 user interface.

FeatureSearch function allows the user to define the directory of curve data. After that, the analyses can be done as it is indicated in Figure 5.35. This figure shows the loaded sample and discriminant absorption features in the left, SPECMIN offerings regarding the selected spectral library in the middle and the results of unmixing analysis in the right bottom which gives the proportions of the content minerals based on selected mineral offerings by the software.

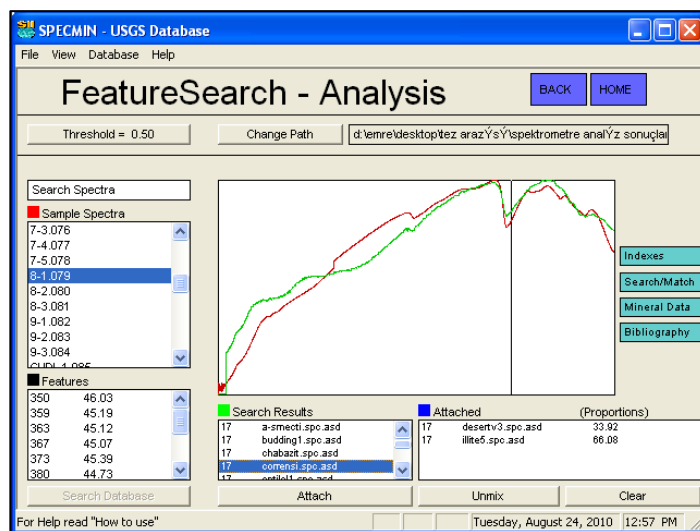


**Figure 5.35** Feature Search window of SPECMIN.

All of the collected samples are analyzed in this software. Firstly, the appropriate end member for that specific mineral is selected. Secondly, preferred end members which have values more than 15% is considered as a content mineral. Lastly, resultant end members are taken as reflectance spectra of that specific sample and are loaded as inputs for ENVI software for mapping and other analyses. Table 5.4 lists SPECMIN analysis results for each sample collected. After completing the analyses, Kaosmec5, Illite3, Montmorillonite9, Desert Varnish3 and Dipyre minerals are selected as end members to be mapped in ENVI Software. The analyses performed in SPECMIN software is presented in Appendix A.

**Table 5.4** SPECMIN Analysis for 8 samples. Bold prints are selected end members after the analyses.

Sample #	Surface	Endmember	%	Sample #	Surface	Endmember	%	
<b>1</b>	1st	Chlorite5	35	<b>7</b>	1st	<b>Illite2</b>	60	
		Dipyre	35			Corrensi	26	
		Siderite	30			<b>Montmorillonite9</b>	8	
<b>2</b>	1st	<b>Illite 3</b>	82			Dipyre	6	
		<b>Montmorillonite9</b>	18	2nd	Desert Varnish2	38		
					Dipyre	24		
<b>3</b>	1st	<b>Desert Varnish3</b>	58			<b>Kaosmec5</b>	16	
		Chlorite6	40			Illite5	13	
		<b>Montmorillonite9</b>	2	3rd	Desert Varnish3	9		
	2nd	<b>Desert Varnish3</b>	60		Desert Varnish1	44		
		Dipyre	18		<b>Desert Varnish3</b>	40		
		<b>Kaosmec5</b>	12		Illite5	16		
			Chlorite6	6	4th	<b>Illite2</b>	42	
		<b>Montmorillonite9</b>	4		Chlorite6	30		
					Corrensi	28		
<b>4</b>	1st	Dipyre	91	5th	Corrensi	30		
		Illite 3	9		<b>Desert Varnish3</b>	22		
	2nd	<b>Desert Varnish3</b>	84		Illite5	18		
<b>5</b>	1st	Dipyre	16			<b>Dipyre</b>	16	
		<b>Desert Varnish3</b>	50			Kaosmec3	7	
		Desert Varnish1	45			Kaosmec1	7	
	2nd	<b>Desert Varnish3</b>	48	<b>8</b>	1st	Desert Varnish1	50	
		Illite 5	42			<b>Desert Varnish3</b>	13	
		Dipyre	10			Dipyre	13	
	3rd	<b>Illite 3</b>	42			Illite5	12	
Mizzoni3		36			Corrensi	12		
Illite 5		22	2nd	<b>Illite3</b>	100			
				3rd	Illite5	65		
4th	<b>Kaosmec5</b>	82			<b>Kaosmec5</b>	20		
	Illite3	18			Dipyre	15		
<b>6</b>	1st	Kaosmec3	52					
		Kaosmec5	14					
		<b>Desert Varnish3</b>	12					
			Corrensi	7				
			Illite5	6				
			Illite1	5				
			<b>Montmorillonite9</b>	4				

#### ***5.2.4 The AdaBoost Algorithm***

AdaBoost, the so-called Adaptive Boosting, is a machine learning algorithm, formulated by Yoav Freund and Robert Schapire (Freund and Schapire, 1995). It can be used in conjunction with many other learning algorithms to improve their performance. “AdaBoost is adaptive in the sense that subsequent classifiers built are tweaked in favor of those instances misclassified by previous classifiers. AdaBoost is sensitive to noisy data and outliers. However in some problems it can be less susceptible to the overfitting problem than most learning algorithms.” (<http://en.wikipedia.org/wiki/AdaBoost>).

Initially, all patterns have the same weight and the classifier C1 is the same as the base classifier in AdaBoost. If the classification error is greater than 0.5, then the method does not work and the procedure is stopped. A minimum accuracy is needed for the base classifier, which can be considerable disadvantage in multiclass problems. Iteration by iteration, the weight of the samples which are correctly classified goes down. The algorithm consequently concentrates on the difficult samples. At the end of the procedure, T weighted training sets and T base classifiers have been generated.

In most cases, the overall accuracy is increased. Many practical classification problems include samples which are not equally difficult to classify. AdaBoost is suitable for such problems. It tends to exhibit virtually no over fitting when the data is noiseless (Benediktsson et al., 2007)

In this study, the generated HC microseepage map using Crosta Technique becomes the input for AdaBoost algorithm. A 200x200 pixel image from map is cropped in order to test the efficiency of Crosta Technique in mapping HC microseepages. Initially, the digital number (DN), DN-Average and DN-Standard Deviation images are prepared for nine ASTER bands covering the same area. Hence, twenty seven images are generated totally. The DN image is the image itself. DN-Average image is prepared with the 5x5 kernel size filter operation. In particular, ENVI's low pass filter is used to yield these images.

Low pass filter can be defined as it preserves the low frequency components of an image, which smooths it. ENVI's low pass filter contains the same weights in each kernel element, replacing the center pixel value with an average of the surrounding values. For the calculation of standard deviation images, Gaussian methodology is used since its processes are based on standard deviation calculations. A type of stretch based on a Gaussian curve, centered on a mean DN value that you specify. The range of data values that fall within a given standard deviation (that you specify) of the mean are stretched from 0 to 255. (ENVI User's Guide, 2008). So, Gaussian Low Pass operation of ENVI is selected to generate standard deviation images. Based on the results of Crosta Technique HC microseepage distribution, twenty eight positive features whose HC content is known and twenty five negative features (training samples for AdaBoost) representing the non-anomalous areas are selected via Feature Selection Program (FSP) designed for this issue (Figure 5.36).

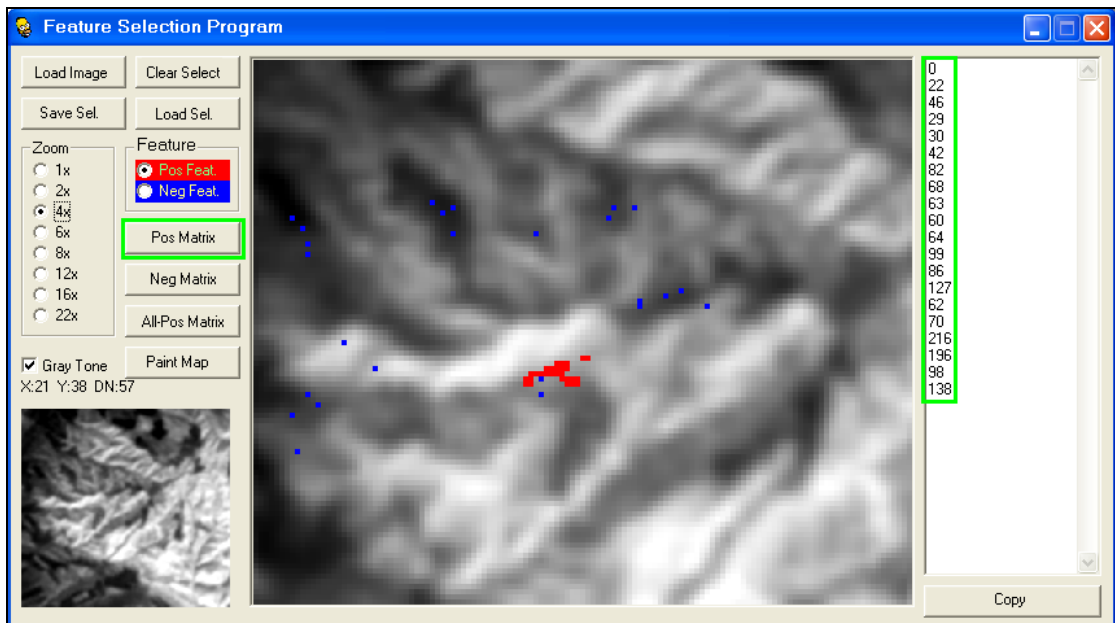


**Figure 5.36** Feature Selection Program (FSP) which is created for selecting training data for AdaBoost Algorithm.

Initially, red dots showing the anomalous and the blue dots illustrate the non-anomalous regions are selected. These selections are saved in order to load the same selection inputs for the other images. The green rectangle on the right of FSP window shows the positive feature output numbers for the selected ASTER band. Then, all the selected DN, DN-Average and DN-Standard Deviation images are analyzed and their output is calculated. These three outputs are the inputs for Matlab's AdaBoost Algorithm.

Loading all of the positive and negative features to AdaBoost interface and executing the generated algorithm for selected ASTER bands, error value and the feature selection matrix which shows the weight value is calculated. Provided that the error value is less than 0.5, all of the weights are gathered for nine ASTER bands after 150 iterations (Figure 5.37). ASTER bands' weight values were generated by AdaBoost algorithm which explains the most appropriate band that possesses much information about the particular target. Hence, bands having the highest weight value must be selected. This selection and related outputs are documented in Chapter 6.

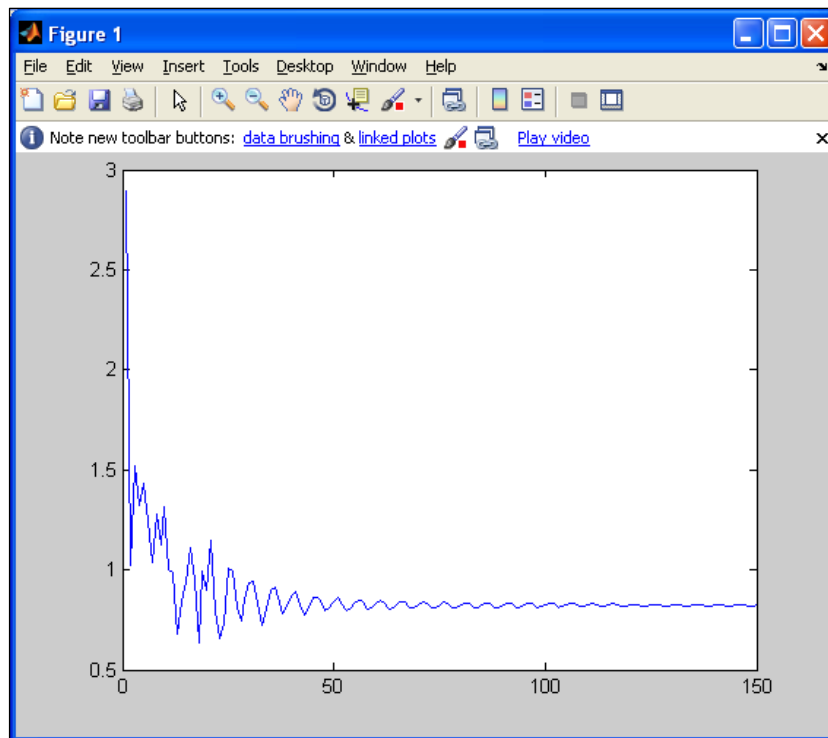


**Figure 5.37** Weight values gathered for band 4 after 150 iterations. After 100 iterations, the weight value becomes stable.

## CHAPTER 6

### RESULTS

This chapter focuses on the results of feature classification techniques, Crosta Technique and AdaBoost Algorithm together with supportive information. Also, the results are compared and accuracy between these two are documented.

Mapping HC microseeps has many difficulties since it is hard to find a place where HC microseepage is present. Besides, there is no specific reflectance curve generated for mapping natural HC microseepages. But there are studies that focus on hydrocarbon related surface alterations and specific anomalies indicating its presence. HC microseepage is dominantly composed of methane (CH<sub>4</sub>), ethane (C<sub>2</sub>H<sub>6</sub>), propane (C<sub>3</sub>H<sub>8</sub>), butane (C<sub>4</sub>H<sub>10</sub>) and pentane (C<sub>5</sub>H<sub>12</sub>). These hydrocarbons can interact with the stratigraphic column and produce an ample variety of physical, chemical, mineralogical, botanical, and microbiological alterations at the surface (Lammoglia et al., 2008). Schumacher (1996) also listed these manifestations, as stated previously.

Microbiological, anomalous non-hydrocarbon gases, altered acoustical, electrical, and magnetic properties, radiation, geothermal and hydrologic anomalies are not detailed in this study since they are not included within the scope of this thesis. The rest of the anomalies, however, are documented. Anomalous hydrocarbon concentrations in sediments and soil can be observed in the vicinity of the reference valley (Figure 6.1).



**Figure 6.1** An anomalous HC accumulation in soil observed in meandering side of the river basin, close to Uğurca Village.

Mineralogical changes such as the formation of calcite and pyrite is present in the area considering the results of SPECMIN analysis. Especially calcite is common among Germav Formation (Figure 6.2.). No analyses available on uranium, elemental sulfur, and certain magnetic iron oxides and sulfides.



**Figure 6.2** A layered structure with HC content and calcite in Germav Formation. Circles show calcite infillings.

Clay mineral alterations are one of the strongest evidences for HC microseepages. Development of clay minerals occurs when the production of  $\text{CO}_2$ ,  $\text{H}_2\text{S}$  and organic acids related to the oxidation of hydrocarbons close to the surface can generate a reducing, slightly acid environment capable of promoting diagenetic alterations of feldspars to clay-minerals, such as kaolinite, illite, and chlorite (Schumacher 1996, 2002). In addition, kaolinite, desert varnish and montmorillonite minerals are found as constitutional clay minerals in anomalous regions. But results indicate that illite is abundant in non-anomalous regions than it does in anomalous regions (Kahn, 2006 and 2008). The reason might be that the conditions above promote diagenetic weathering of feldspars to produce clays and may lead to the conversion of normally stable illitic clays to kaolinite. Segal et al. (1984, 1986) reported that bleached portions (which is another surface indicator for HC seeps) of a formation of study

area directly overlying the field contain primarily kaolinite clays, whereas the unbleached areas located away from the field contain fresh plagioclase and muscovite. The bleached rock contains more than three to five times kaolinite than the unbleached formation. Documentation also indicates that the distribution of the bleached outcrops of the formation approximates the geographic limits of the oil and gas reservoirs at depth. The geographic distribution of the kaolinite is inversely related to that of the mixed-layer illite-smectite clays, suggesting that the enrichment of kaolinite is also linked to the depletion of other clay (Conel and Alley, 1985). Clay mineral diagenesis has also been documented where kaolinite and mixed-layer illite-smectite clays of late origin have replaced detrital illite in red beds (Lilburn and Al-Shaieb, 1983, 1984). Another occurrence of HC-related formation of kaolinite has been described by Reid et al. (1992) which is a site of an oxidation-reduction front that developed in the outcrop of the sand due to active oil seepage. Coarse-grained authigenic kaolinite in concentrations up to 2 % is present in the altered rocks of the outcrop.

Bleaching of red beds is another important surface manifestation indicating HC microseepages (Figure 6.3.). Bleaching forms whenever acidic, reducing fluids dissolve the ferric oxide (hematite) which gives the red bed its characteristic color (Scholte et al., 2003). The reducing environment due to the microseepage phenomenon can convert ferric-bearing minerals to the soluble ferrous state, which cause bleaching of former “red beds” and soils (e.g., Donovan 1979, 1986, Oliveira 1998). Donovan (1974) also reported that the color of a studied unit grades from reddish-brown for unaltered formation to the field to pink, yellow, and white where maximum bleaching and iron loss occur. The ferric iron shows an absorption feature at 0.9  $\mu\text{m}$  and the visible spectrum drops sharply producing a maximum near 0.80  $\mu\text{m}$  (Hunt et al., 1973; Hunt, 1977). Under ideal laboratory conditions, the ferrous iron in non-transparent minerals such as pyrite and magnetite shows a low total reflectance, while in transparent mineral such as siderite, shows a broad shallow band at 1.0-1.1  $\mu\text{m}$  (Hunt and Salisbury, 1970).

These characteristics can be used in remote sensing data processing and separating bleached red beds from the unbleached ones.



**Figure 6.3** Bleached red beds close to possible oil seepage zone which discovered during ground checking studies. Note that bleaching of the red bed is continuous towards possible oil seeps.

Geobotanical anomalies are changed where HC microseepage creates a chemical reduction zone in the soil column at depths shallower than expected in the absence of seepage. Such leakage stimulates the activity of hydrocarbon-oxidizing bacteria, which reduces soil oxygen concentration whereas the concentration of CO<sub>2</sub> and organic acids increase. These changes can affect pH and Eh in soils, which results in the solubility of the trace elements and as a result their availability to plants (Schumacher, 1996).

The above mentioned issues illustrate those minerals especially kaolinite, kaolinite+smectite (kaolinite+smectite) and desert varnish are present where HC microseepage occurs.

Illite and montmorillonite, however, can be recognized in especially non-anomalous regions. Bleaching occurs in anomalous places due to the reduction characteristic created by HC. Geobotany, on the other hand, reduces on the HC seepage zone due to the reduction in soil oxygen concentration and increase in CO<sub>2</sub> and organic acid content which changes pH and Eh equilibrium of soils. Two classification methods, Crosta Technique and The AdaBoost Algorithm below are used in order to detect and map HC microseepages and its related surface manifestations in Gemrik Anticline.

So far, HC microseepage and its surface indicators were mapped using Crosta Technique. It is concluded that Illite mineral accumulates basically in the north east flank of Gemrik Anticline which HC microseepages are not present. On the other hand, kaolinite, desert varnish, montmorillonite and dipyrre minerals mostly dense in south west side of anticline axis which is the also the anomalous regions close to Bozova Fault. The endmember minerals and band combinations to map them are tabulated in table 6.1.

The thematic map of Gemrik Anticline is finalized showing all of the features in one scene (Figure 6.4). The reason explaining this would be the production of CO<sub>2</sub>, H<sub>2</sub>S and organic acids linked to hydrocarbon oxidation close to the surface produces a reducing, slightly acid environment which leads to diagenetic alterations of feldspars to clay-minerals, such as kaolinite, illite, and chlorite (Schumacher 1996, 2002). Chlorite was also gathered during the analyses but due to its low overall percentage, this mineral is not taken into account. Besides, study based on evaluation of hydrocarbon occurrences showed that majority of clay minerals are kaolinite and montmorillonite (Pomeroy et al., 1965). Also it can be stated that the mineral maps were produced to further support HC microseepage map, indeed.

Table 6.1 Endmembers and related band combinations to map them.

<b>ENDMEMBER</b>	<b>BAND COMBINATION</b>
HYDROCARBON	1,4,5,8(Crosta) & 1,5,6,8 (AdaBoost)
ILLITE3	1,3,5,6
MOTMORILLONITE	4,6,7,8
KAOSMEC5	1,3,6,7
DIPYRE	1,5,6,8
DESERT VARNISH	4,5,6,8

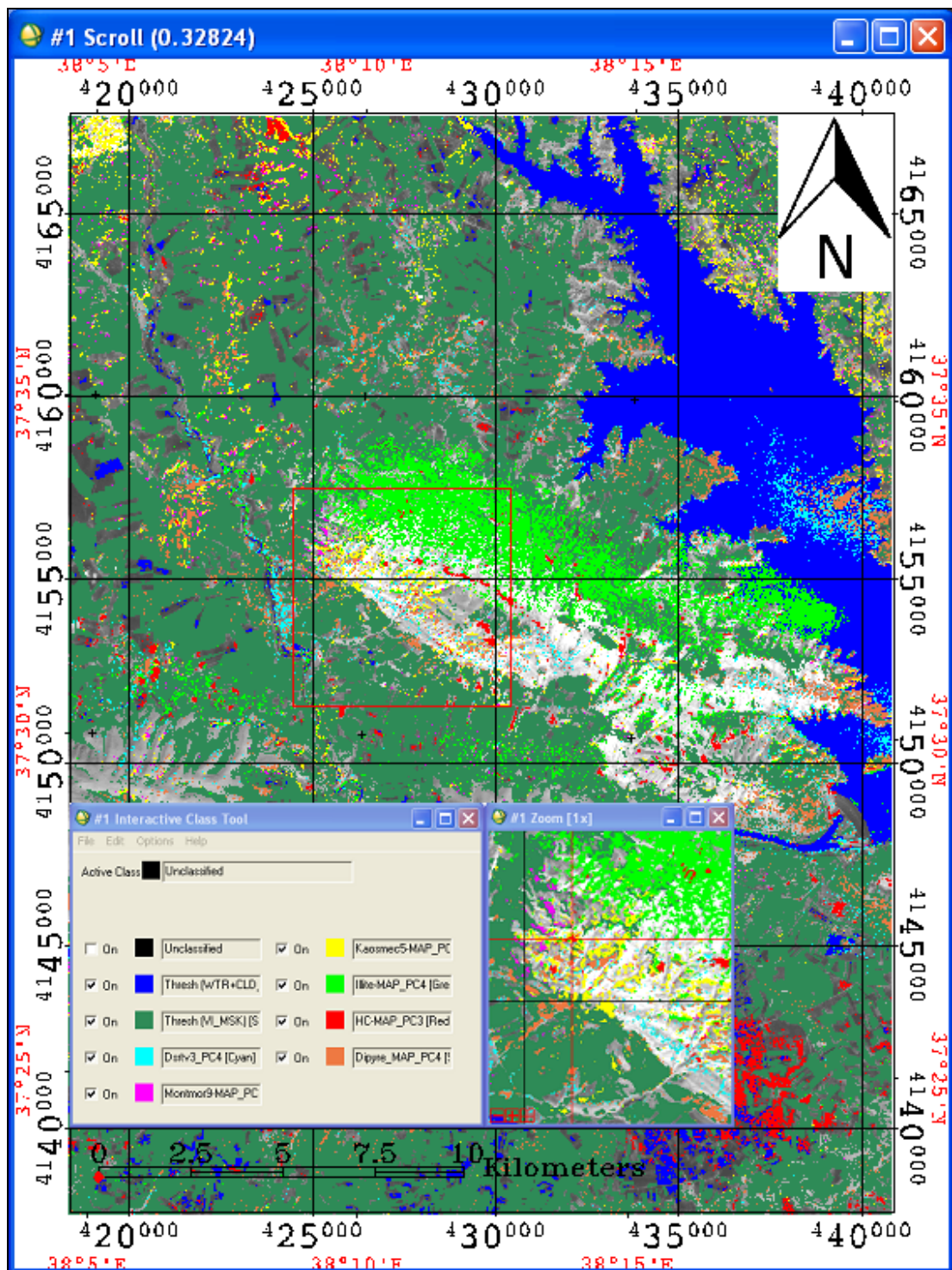


**Figure 6.4** Thematic map of Gemrik Anticline. The Red Cross in the zoom window shows Uğurca Village surroundings and the HC related clay mineral alteration.

Figure-Chart below shows the abundance of clay minerals over anomalous and non-anomalous regions (Figure 6.5.).

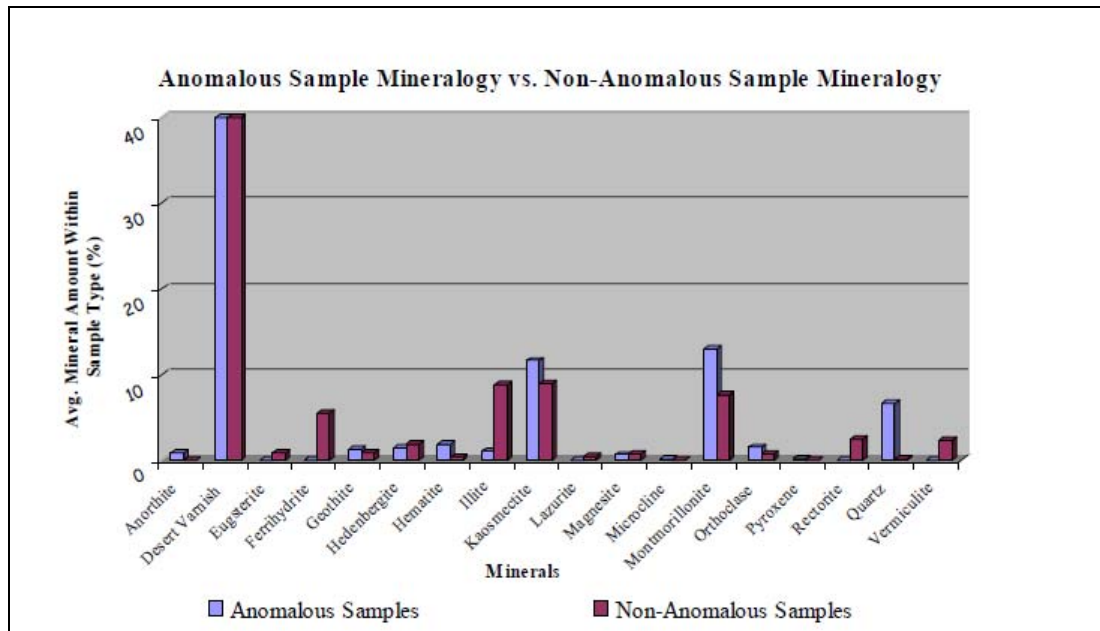


**Figure 6.5** Mineral distributions on anomalous and non-anomalous regions (Kahn, 2006).

According to Kahn’s study conducted based on laboratory spectroscopy, kaolinite and montmorillonite are more abundant in anomalous regions. Illite, on the other hand, is abundant in non-anomalous regions. Desert varnish shows an equal distribution. Considering the thematic map produced as a result of this thesis, results show consistency. But it must be noted that Dipyre, is a new output which shows dominant distribution on anomalous regions like desert varnish does for this thesis study.

Of course; the prospect points offered by Crosta Technique application are visited. Five out of seven coordinates showed similar anomalous characteristics to that of reference valley in which its HC content is known. It must be noted that none of the stops visited are analyzed in geochemical aspect, yet. Figures 6.6, 6.7, 6.8, 6.9, 6.10 and 6.11 below show the anomalous and non-anomalous locations visited.



**Figure 6.6** Anomalous regions in the first stop of ground truth study. The bleached parts are separated by a red line from red beds which probably occurs as a result of reduction zone created by HC microseepage.

Figure 6.6 clearly illustrates red bed bleaching over the study area. Probably iron is removed from the media due to reduction zone which gives reddish color to soil. As a result, bleaching occurs over HC microseepage zones.



**Figure 6.7** A river bed towards the second stop showing a probable HC seepage outcropped due to river erosion.



**Figure 6.8** A non-anomalous location which was supposed to be an anomalous zone regarding HC microseepage map.



**Figure 6.9** Another anomalous location was explored as one of the ground checking points visited.



**Figure 6.10** A location showing prospect close to reference valley, i.e., close to Uğurca Village.



**Figure 6.11** An outcropped layer in the location shown in the previous image. Note the active oil seepages indicated.

AdaBoost algorithm, on the other hand, was executed and the weight values were gathered. The resultant weight values and the selected bands are shown in table 6.2. This table separately shows the results for (DN) and (DN+DN-Avg.+DN-St.Dev.) sum. All the error values are less than 0.5. According to these results, ASTER bands 1,5,6,8 seem the most suitable combination in order to map the target mineral (Figure 6.12).

**Table 6.2** AdaBoost weights computed.

		Weight Val	Error Val
band1	dn	0.067662048	0.483090939
	dn+av+sd	<b>1.443635475</b>	0.190983006
band2	dn	0.822162139	0.305304891
	dn+av+sd	0.822162139	0.305304891
band3	dn	0.161130627	0.459804273
	dn+av+sd	0.736728883	0.323719861
band4	dn	0.155710012	0.461150959
	dn+av+sd	0.823192093	0.305086487
band5	dn	0.822162876	0.305304734
	dn+av+sd	<b>1.443635475</b>	0.190983006
band6	dn	0.069981995	0.482511638
	dn+av+sd	<b>1.443635475</b>	0.190983006
band7	dn	0.822161217	0.305305086
	dn+av+sd	0.822159121	0.305305531
band8	dn	0.823192093	0.305086487
	dn+av+sd	<b>1.443635475</b>	0.190983006
band9	dn	0.579276681	0.359099046
	dn+av+sd		

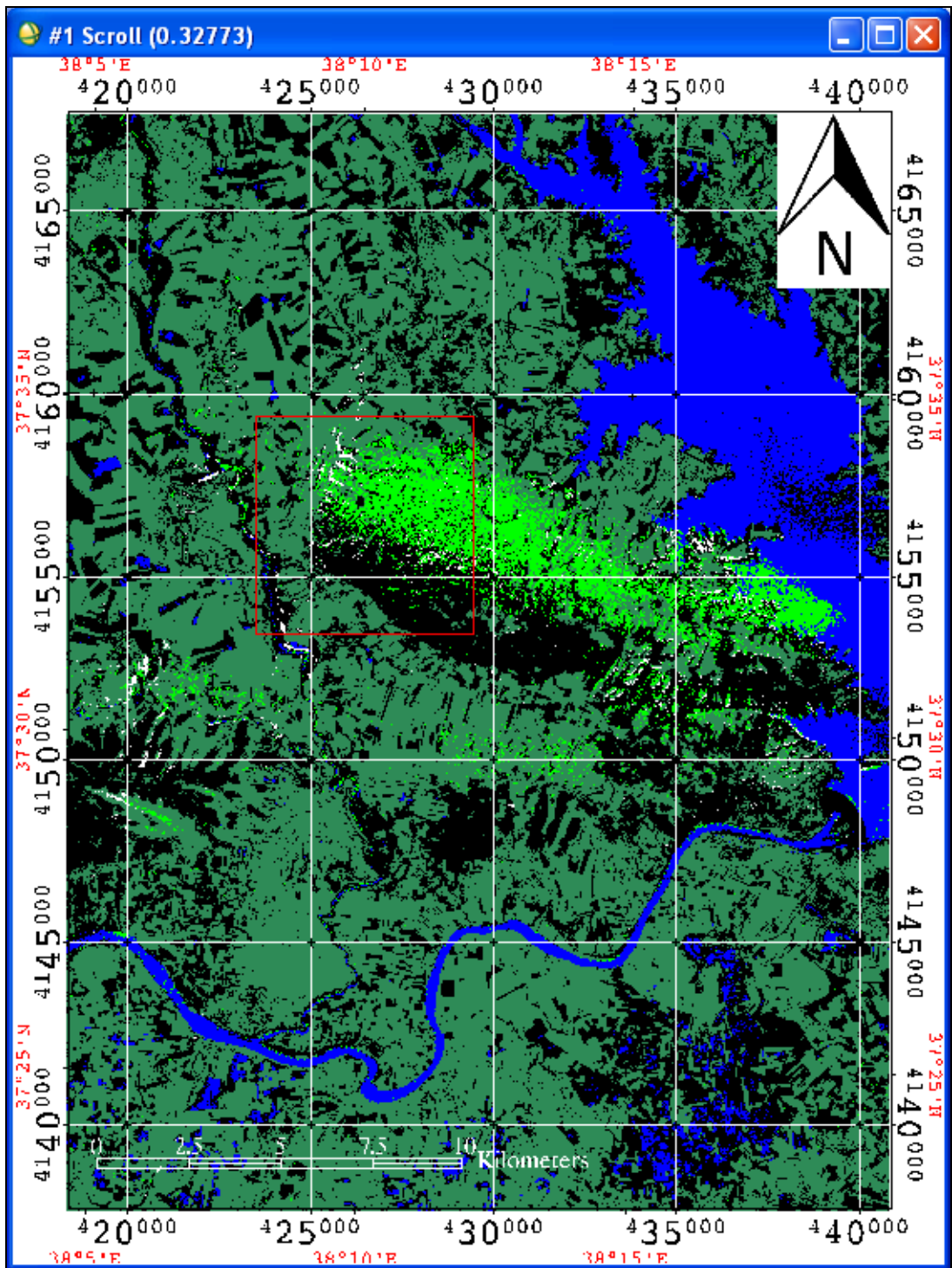


**Figure 6.12** AdaBoost offered HC microseepage map. Whites are HC microseepage.

Results show that Crosta Technique and Adaboost Algorithm outputs are close. Crosta offers ASTER bands 1,4,5,8 to map seepages whereas AdaBoost Algorithm analysis indicates ASTER bands 1,5,6,8. The zoom image of AdaBoost results to the reference valley is shown in Figure 6.13 where whites are indicating HC microseepages.



**Figure 6.13** Zoom image to reference valley showing the HC map according to AdaBoost analysis.

The accuracy assessment of this study is performed considering the outputs of Crosta Technique and the AdaBoost Algorithm. In order to do that, band combinations (hence the maps) are correlated. As it is stated, Crosta idea is based on principle component analyses which inputs the bands selected. Using the literature and field spectrometer measurements (in the last field reconnaissance) the absorption features and other spectral characteristics of hydrocarbon bearing materials have been gathered. As a result, using ASTER band combination 1, 4, 5 and 8, HC microseepage map of Gemrik Anticline is generated. AdaBoost, on the other hand, is an image processing algorithm used to enhance the results of Crosta Technique generated HC microseepage map further.

In order to do that, average and standard deviation images are generated from digital number image, i.e., the image itself. Knowing the coordinates of anomalous and non-anomalous locations, training data pixels were selected from these areas as positive and negative features, respectively. The selected digital numbers are carried to the AdaBoost Algorithm which outputs weight and error values depending on positive and negative features selected. This process is completed for nine ASTER bands. Weight value represents data possession for a particular feature in that band. Hence, four bands having the highest weight values have been selected. The reason why four bands were selected is to keep the methodology fixed in analysis so that the results would be compared conveniently. After the algorithm executed, band combination 1, 5, 6 and 8 were found to have the highest weights that are bearing HC feature.

Comparing the two results, 75 % of overlap success has been found. They became 1,4,5,8 for Crosta and 1,5,6,8 for AdaBoost to map HC microseepage over the anticline. The output maps of two methods are illustrated in figure 6.14.

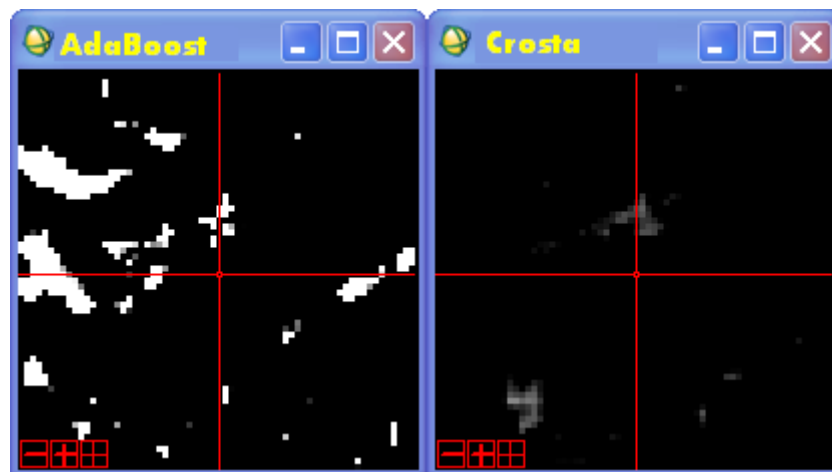


**Figure 6.14** Crosta Technique generated HC microseepage map versus AdaBoost Algorithm outputs showing the reference valley in the cross point.

## CHAPTER 7

### DISCUSSIONS AND CONCLUSIONS

Mapping HC microseepages became an issue of consideration for oil exploration facilities in the last few decades. For that reason, it is important to map it and its surface manifestations since they can be direct indicators of possible oil reservoirs. Previous studies put many ideas forward on the issue but overall success rate might have been increased. Common suggestions on improving the accuracy of the HC maps mainly focus on usage of image processing algorithms that make use of spatial information. Crosta technique mapped HC microseepages in Gemrik Anticline (Adiyaman) in a considerable extent. The HC map is generated on the basis of absorption and reflectance features of oil bearing materials. Field reconnaissance showed that more than 65 % of suggested anomaly points were similar to that of reference valley.

During the ground checking work, it has been found that HC microseepages have distinctive absorption features at  $1.41\mu\text{m}$  and  $1.89\mu\text{m}$ . Hence HC microseepages have distinct absorption values at  $1.41\mu\text{m}$  and  $1.89\mu\text{m}$  additionally to that of  $1.73\mu\text{m}$  and  $2.31\mu\text{m}$  as stated in literature. These measurements are illustrated in Appendix C.

Although geochemistry results of the ground truth samples have still not been gathered, some of the ground check points are close to bleached red beds. Indeed, the band combination offered for mapping HC microseepages mapped also bleached zones in this study. Crosta technique is already capable of mapping certain clay minerals such as illite, montmorillonite, smectite and kaolinite. According to

literature information, kaolinite, illite and montmorillonite are surface alteration minerals indicating HC microseepage.

This study also showed that desert varnish and dipyrre minerals can be added to the list considering HC microseepage surface alteration minerals. Hence, it could be stated that ASTER data is capable of mapping HC microseepages and related surface manifestations.

Geophysics, on the other side, can be charged with this study in order to increase the contribution to oil exploration studies. Particularly, interpreted seismic profiles would be combined with remote sensing HC microseepage map. Normally, oil wells spud in order to test the prospect traps that are detected after seismic profile interpretation. But, knowing the surface locations of oil seepages by remote sensing yielded maps and combining these with underground information coming from seismic data, it can be inferred that the prospect trap structure observed in seismic profile is most probably oil possessing.

Adaboost algorithm, which is a MATLAB software code, is used to improve the performance of Crosta technique in generating HC map. Firstly, digital number, average and standard deviation images were prepared and cropped over HC seepage zone. Secondly, training samples of AdaBoost were chosen from these twenty seven (DN, average and standard deviation images for nine bands) HC maps by using Feature Selection Program. Then, executing these selected positive (anomalous regions) and negative (non-anomalous) features in AdaBoost code, weight values are gathered for nine ASTER bands as the output of the algorithm. Lastly, four highest weights for corresponding bands are selected and these bands were analyzed using PCA analyses. This analysis showed that results of Crosta generated HC map and AdaBoost offered band offerings are similar. Crosta technique band combination is 1,4,5,8 whereas AdaBoost offerings to map HCs are 1,5,6,8. Besides, suggested band combination for AdaBoost is the same as the one for mapping dipyrre mineral, which is another outcome of this study. Indeed, AdaBoost not only helps to improve HC map but also presents a methodology for mapping any preexisting or undefined features.

This study showed that feature classification technique Crosta and image processing algorithm AdaBoost can be used together in order to map HC microseepages and related clay mineral alterations successfully.

The success rate of mapping HC microseepages would be increased by further considerations. Thermal infrared bands of ASTER would be charged in order to detect soil gas over HC microseepage zone which will support the idea further. AdaBoost algorithm can be improved by supplying more training samples from the feature map.

But this time inconsistency, error values and duplicate pixel avoidance would be a problem since selected pixels for negative and positive features might overlap with each other. In order to solve this problem, high resolution hyperspectral images must be in charge. In addition, the MATLAB can not compile larger images due to file size. So, further studies would be developed for testing larger images. On the other hand, additional types of separation classifiers can be used in order to map the area in a detailed manner.

## REFERENCES

Abrams, M., 2000, The Advanced Spaceborne Thermal Emission and Reflection Radiometer (ASTER): data products for the high spatial resolution imager on NASA's Terra platform, *International Journal of Remote Sensing*, **21**, pp. 847–859.

ASTER User's Guide, 2007, Data Products, Earth Remote Sensing Data Analysis Center, **5.1**, Part 2, 1p.

Benediktsson, J.A., Chanussot, J., and Fauvel, M., 2007, Multiple Classifier Systems in Remote Sensing: From Basics to Recent Developments, **4472**, pp.502, 503.

Carranza, E. J. M., and Hale, M., 2002, Mineral imaging with Landsat Thematic Mapper data for hydrothermal alteration mapping in heavily vegetated terrain. *International Journal of Remote Sensing*, **23**, pp.4827-4852.

Clarke, R.H. and Cleverly, R.W., 1991, Petroleum seepage and post accumulation migration. In: W. A. England e A. J. Fleet, (eds.) Petroleum Migration, *Geological Society Special. Publication*, Geological Society of London, **59**, pp. 265-271.

Cloutis, E. A., 1989, Spectral reflectance properties of hydrocarbons: remote sensing implications, *American Association for the Advancement of Science*, **245**, pp.165-168.

Conel, J. E. and Alley, R. E., 1985, Lisbon Valley, Utah uranium test site report, in M. J. Abrams, J. E. Conel, H. R. Lang, and H. N. Paley, eds., The Joint NASA/Geosat Test Case Project: final report, *AAPG Special Publication*, pt. 2, **1**, pp. 8-1–8-158.

Çoruh, T., 1991, Adıyaman civarında yüzeyleyen Kampaniyenistifinin biyostratigrafisi ve paleocoğrafik evrimi: TPAO Araştırma Merkezi, Rapor no.16656, 101 s.

Crosta, A. P., and Moore, J. McM., 1989, Enhancement of Landsat Thematic Mapper imagery for residual soil mapping in SW Minas Gerais State Brazil: a prospecting case history in greenstone belt terrain. *Proceedings of the 9th Thematic Conference on Remote Sensing for Exploration Geology, Calgary*, pp1173-1187.

Crosta, A.P., De Souza Filho, C.R., Azevedo, F. and Brodie, C., 2003, Targeting key alteration minerals in epithermal deposits in Patagonia, Argentina, using ASTER imagery and principal component analysis, *International Journal of Remote Sensing*, **24**, n.21, 4233 p.

De Jong, S.M. and Van der Meer, F.D., 2004, Remote Sensing Image Analysis: Including the Spatial Domain, pp.201-210.

Donovan, T.J., 1974, Petroleum microseepage at Cement, Oklahoma: evidence and mechanism, *AAPG Bulletin*, **58**, pp.429-446.

Donovan, T.J., Forgey, R.L., and Roberts, A. A., 1979, Aeromagnetic detection of diagenetic magnetite over oil field, *The AAPG Bulletin*, **63**: pp.245-248.

Donovan, T.J., O'Brien, D.P., Bryan, J.G., Cunningham, K.I., 1986, Near surface magnetic indicators of buried hydrocarbons: aeromagnetic detection and separation of spurious signals, *5th Thematic Conference Remote Sensing for Exploration Geology. Proceedings*, **1**, pp.219-232.

ENVI User's Guide, 2008, Preprocessing Utilities, Log Residuals, Low Pass.

Fu, B., Zheng, G., Ninomiya, Y., Wang, C., Sun, G., 2007, Mapping hydrocarbon-induced mineralogical alteration in the northern Tian Shan using ASTER multispectral data, *Terra Nova*, **19**, pp.228, 229.

Grim, R. E., and N. Güven, 1978, Bentonites: Geology, mineralogy, properties and uses, *Dev. Sediment*, **24**, 256 p.

Güven, A., Tuna, M. E., and Çoruh, T., 1991, Güney Doğu Anadolu Kampaniyen-Paleosen otokton istifinin stratigrafisi: TPAO Arama Grubu, Rapor No.2828, 133 s.

Hörig, B., Kühn, F., Oschütz, F., and Lehmann, F., 2001, Hyperspectral remote sensing to detect hydrocarbons, *International Journal of Remote Sensing*, **22**, pp. 1413-1422.

Horvitz, L., 1939, On geochemical prospecting: *Geophysics*, vol. 4, p. 210–228.

Hunt, G.R., 1977, Spectral Signatures of particulate minerals in the visible and near infrared, *Geophysics* , **42**, No.3, pp.501-513.

Hunt, G.R. and Salisbury, J.W., 1970, Visible and near-infrared spectra of minerals and rocks: I. Silicate minerals, *Modern Geology*, **1**, pp.283-300.

Hunt, G.R., Salisbury, J.W., and Lenhoff, C.J., 1973, Visible and near-infrared spectra of minerals and rocks: VI. Additional silicates, *Modern Geology*, **4**, pp.85-106.

Kahn, S.D., 2006, Mapping Alteration Caused by Hydrocarbon Microseepages in Patrick Draw area Southwest Wyoming Using Image Spectroscopy and Hyperspectral Remote Sensing, Grant/Cooperative Agreement No. DE-FG26-05NT42494, 15p.

Kahn, S.D. and Jacobson, S., 2008, Remote sensing and geochemistry for detecting hydrocarbon microseepages, *GSA Bulletin*, **120**, pp. 96, 99-104.

Kuhn, F., Opperman, K., and Höring, B., 2002, Hydrocarbon Index-an algorithm for hyperspectral detection of hydrocarbons, *International Journal of Remote Sensing*, **25**, No.12, pp. 2467-2473.

Lammoglia, T., Souza Filhoa, C.R., and Filho, R.A., 2008, Characterization of Hydrocarbon Microseepages in the Tucano Basin, (Brazil) Through Hyperspectral Classification and Neural Network Analysis of Advanced Spaceborne Thermal Emission and Reflection Radiometer (Aster) Data, *The International Archives of the Photogrammetry, Remote Sensing and Spatial Information Sciences*, **37**, Part B8., pp.1196, 1198.

Lilburn, R. A. and Al-Shaieb, Z., 1983, Geochemistry and isotopic composition of hydrocarbon-induced diagenetic aureole (HIDA), Cement, Oklahoma: Oklahoma City Geological Society Shale Shaker, pt. I, **34**, No. 4, pp. 40–56.

Lilburn, R. A. and Al-Shaieb, Z., 1984, Geochemistry and isotopic composition of hydrocarbon-induced diagenetic aureole (HIDA), Cement, Oklahoma: Oklahoma City Geological Society Shale Shaker, pt. II, **34**, No. 5, pp.57–67.

Løseth, H. et al., 2008, Hydrocarbon leakage interpreted on seismic data, *Marine and Petroleum Geology*, 14 p.

Loughlin, W. P., 1991. Principal Component Analysis for alteration mapping, *Photogrammetric Engineering and Remote Sensing*, **57**, pp.1163-1169.

Oliveira, W.J., 1998, Caracterização das emanações gasosas de hidrocarbonetos na região do Remanso do Fogo (MG), através do uso integrado de sensoriamento remoto, geoquímica, geofísica, geologia estrutural e espectrometria de reflectância. Dissertação de Doutorado, Instituto de Geociências, Universidade Estadual de Campinas-SP., 239 p.

Pekesin, B., 2005, Mineral mapping in Oymaağaç (Beypazari – Ankara) granitoid by remote sensing techniques, 38 p.

Petrovic, A., Khan, S.D., Chafetz, H.S., 2008, Remote detection and geochemical studies for finding hydrocarbon-induced alterations in Lisbon Valley, Utah, *Marine and Petroleum Geology*, **25**, 696 p.

Pomeroy, L.R., Smith, E.E., and Grant, C.M., 1965, The exchange of phosphate between estuarine water and sediment, *Limnology and Oceanography*, **10**, pp.167-172.

Reid, J. C., Campbell, B. S., and Ulrich, S. D., 1992, Hydrocarbon-induced mineralogic and geochemical alteration, Turkey Creek, *Colorado: Association of Petroleum Geochemical Explorationists Bulletin*, **8**, pp.64–95.

Ruiz-Armenta, J. R. and Prol-Ledesma, R. M., 1998, Techniques for enhancing the spectral response of hydrothermal alteration minerals in Thematic Mapper images of Central Mexico, *International Journal of Remote Sensing*, **19**, pp.1981-2000.

Saunders, D.F., K.R. Burson, J.J. Brown, and C.K. Thompson, 1999, Model for hydrocarbon microseepage and related near-surface alterations: *AAPG Bulletin*, **83**, pp. 170–185.

Scholte, K.H., Hommels, A., Van der Meer, F.D., Kroonenberg, S.B., Hanssen, R.F., Aliyeva, E., Huseynov, D. and Guliev, I., 2003, Preliminary ASTER and InSAR Imagery Combination for Mud Volcano Dynamics, Azerbaijan, 3<sup>rd</sup> EARSeL Workshop on Imaging Spectroscopy, Herrsching, 380p.

Schumacher, D., 1996, Hydrocarbon-induced alteration of soils and sediments, *Hydrocarbon migration and its nearsurface expression*, D. Schumacher and M. A. Abrams, eds., *AAPG Memoir* **66**, pp. 71–89.

Schumacher, D., 1996, Surface Geochemical Exploration for Petroleum, Principles of Surface Geochemical Exploration, Chapter 18, pp.6, 10.

Schumacher, D., 2002. Hydrocarbons Geochemical Exploration for Petroleum In D. Schumacher e M.A. Abrams (eds) *Hydrocarbon migration and its near-surface expression. AAPG, Memoir* **66**, pp.184-204.

Segal, D. B., Ruth, M. D., and Merin, I. S., 1986, Remote detection of anomalous mineralogy associated with hydrocarbon production, Lisbon Valley, Utah: *The Mountain Geologist*, **23**, No. 2, pp.51–62.

Segal, D. B., Ruth, M. D., Merin, I. S., Watanabe, H., Soda, K., Takano, O., and Sano, M., 1984, Correlation of remotely detected mineralogy with hydrocarbon production, Lisbon Valley, Utah: ERIM, *Proceedings of the International Symposium on Remote Sensing for Exploration Geology*, pp.273–292.

Şengüler, İ., 2007, Asfaltit Ve Bitümlü Şeylin Türkiye'deki Potansiyeli Ve Enerji Değeri, *TMMOB Türkiye VI. Enerji Sempozyumu*

Smailbegovic, A.; Gray, K.; Johnson, K.; Murphy, V.; Holbrook, R., 2009, *Hyperspectral Image and Signal Processing: Evolution in Remote Sensing*, pp.3-5.

Staskowski, R.J., 2004, Utility of Aster For Detecting Hydrocarbon, AAPG Annual Convention, pp.1-2.

Tangestani, M. H. and Moore, F., 2002, Porphyry copper alteration mapping at the Meiduk area, Iran, *International Journal of Remote Sensing*, **23**, pp.4815-4826.

Thompson, C.K., Saunders, D.F., Burson, K.R., 1994, Model advanced for hydrocarbon microseepage, related alterations. *Oil & Gas Journal*. ABI/INFORM Global, **84**, pp. 95-99.

Tok, N., 2003, Sismik Hız Tuzakları ve Derinlik Yaklaşımı, Sahanın Batıya Doğru Geliştirilmesi Yönündeki Öneriler, pp. 5-6.

Van Der Werff, H.M.A, Noomen, M.F., Van Der Meijde, M, .and Van Der Meer, F.D., 2007, Remote sensing of onshore hydrocarbon seepage: problems and solutions, *Geological Society, London, Special Publications*; **283**; pp. 131-132.

Yang, H., Van der Meer, F., Zhang, J., Kroonenberg, S.B., 2000, Direct detection of onshore hydrocarbon microseepages by remote sensing techniques, *Remote Sensing Reviews*, **18**, pp. 5-7, 13.

Yılmaz, E., 2000, Burç-1 Kuyusunda Kesilen Birimlerin Stratigrafi, Sedimantoloji, Reservuar ve Jeokimyasal özellikleri, TPAO Report No:4148, pp. 7-10.

Yılmaz, E., and Duran, O., 1997, Güneydoğu Anadolu Bölgesi Otokton ve Allohton Birimler Stratigrafi Adlana Sözlüğü "Lexicon". Türkiye Petrolleri A.O. Araştırma Merkezi grubu Başkanlığı, Eğitim Yayınları No. 31, pp. 213, 220-222, 235, 262.

Zhang, G., Shen, X., Zou, L., and Lu, S., 2007, Identifying hydrocarbon leakage induced anomalies using Landsat-7 /ETM+ data processing techniques in the west slope of Songliao basin, China, 1 p.

Zhang, J., 2006, Hyperspectral data analyzing for characterizing hydrocarbon microseepage at sandstone-type uranium deposits, IIEE, pp. 1557, 1558.

## **ONLINE RESOURCES**

California Institute of Technology, <http://minerals.caltech.edu/files/varnish/index.html>, last visited on September 2010.

Encyclo Online Encyclopedia, <http://www.encyclo.co.uk/webster/D/71>, last visited on September 2010.

The Ocean Drilling Program, [http://www.odp.tamu.edu/publications/tnotes/tn30/tn30\\_11.htm](http://www.odp.tamu.edu/publications/tnotes/tn30/tn30_11.htm), last visited on August 2010.

USGS, [http://speclab.cr.usgs.gov/spectral.lib06/ds231/DESCRIPT/C/des\\_varnish\\_entrada.html](http://speclab.cr.usgs.gov/spectral.lib06/ds231/DESCRIPT/C/des_varnish_entrada.html), last visited on September 2010

Wikipedia, the free encyclopedia, <http://en.wikipedia.org/wiki/AdaBoost>, last visited on September 2010.

## APPENDIX A

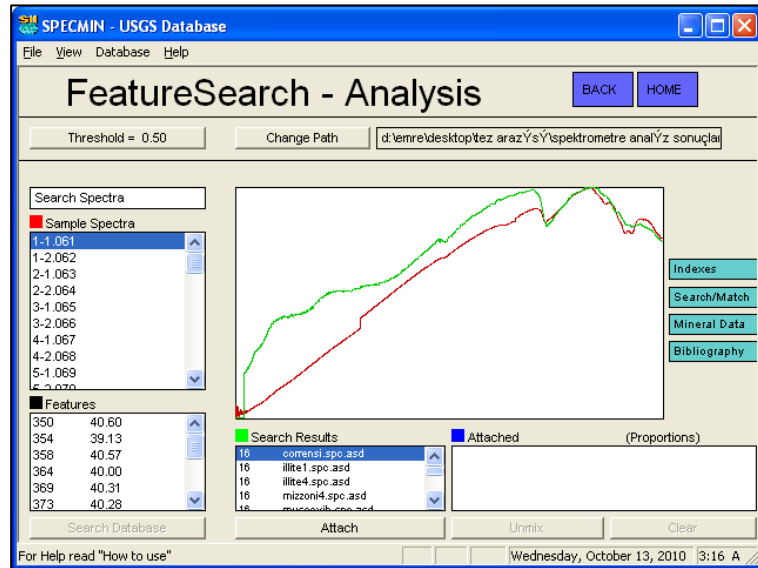


**Figure A.1.** Scene showing an instant while iterations are being analyzed.

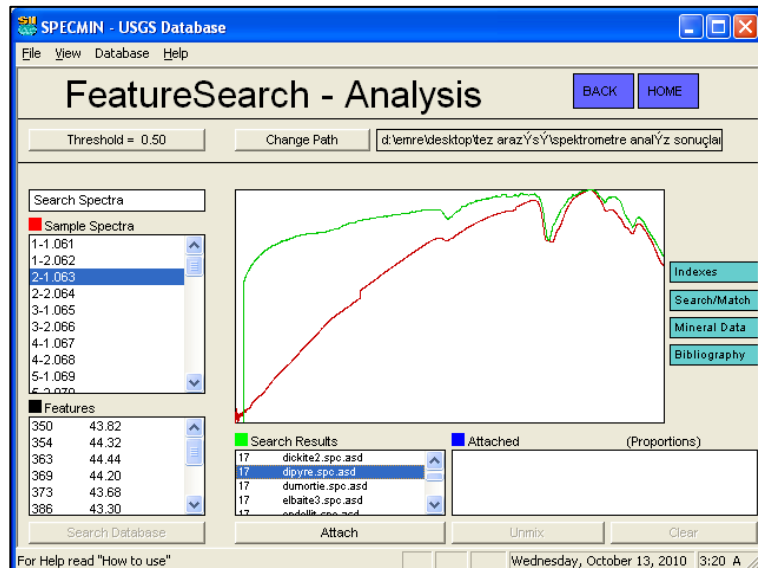


**Figure A.2.** Dipyre is a suitable iteration for this sample.

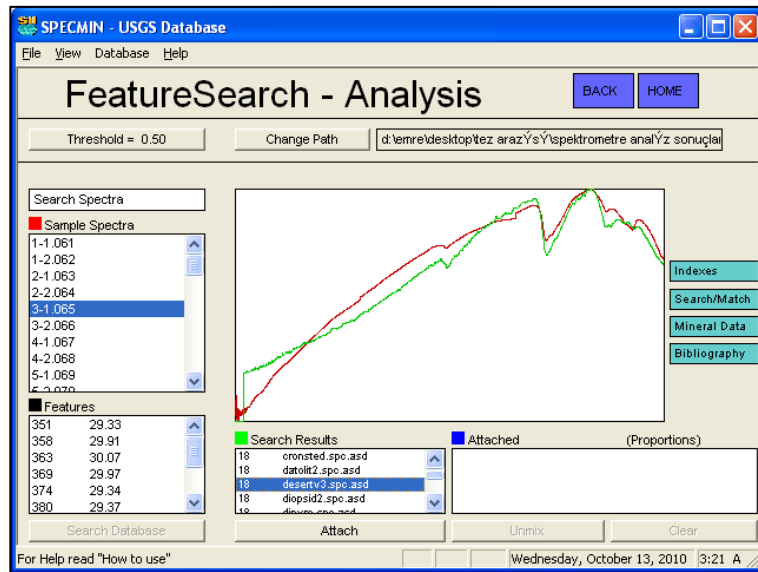


Figure A.3. Desert varnish is found as a constitutional mineral for this sample.

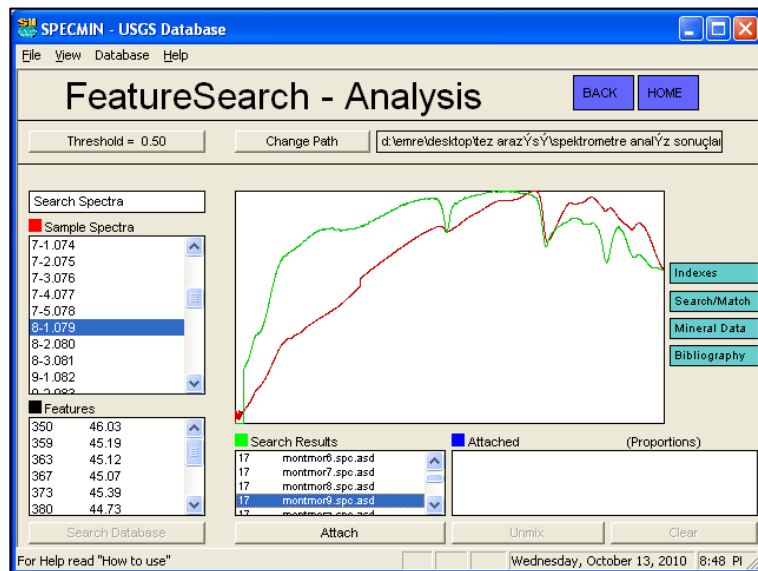
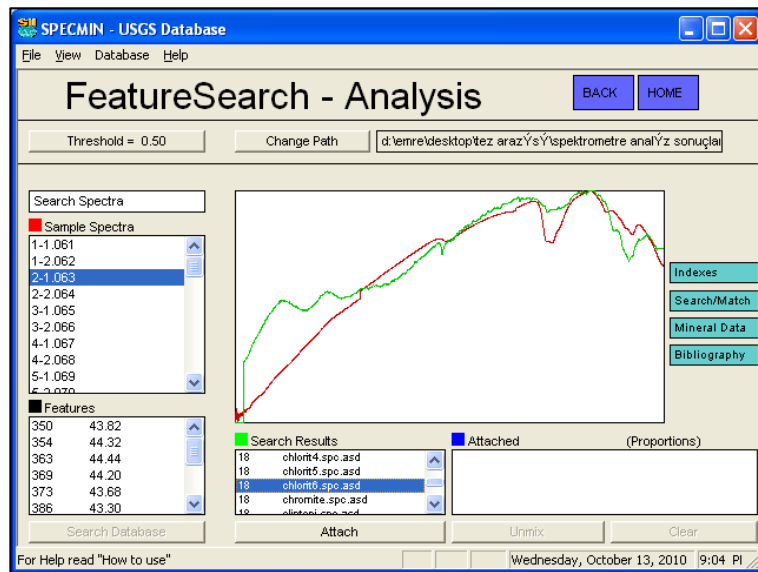
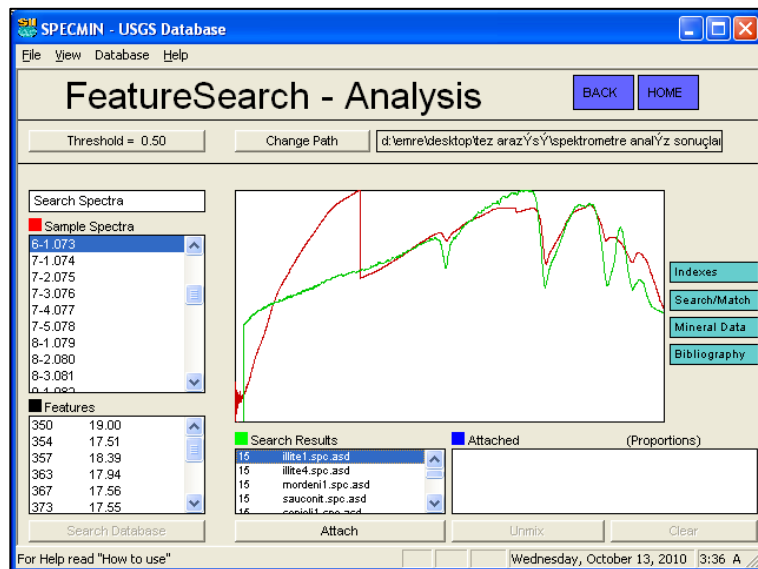


Figure A.4. Montmorillonite is another endmember chosen after analyses.



**Figure A.5.** Chlorite was another output but not taken into consideration due to its low containment.



**Figure A.6.** Illite absorption comparing with that of the sample's.

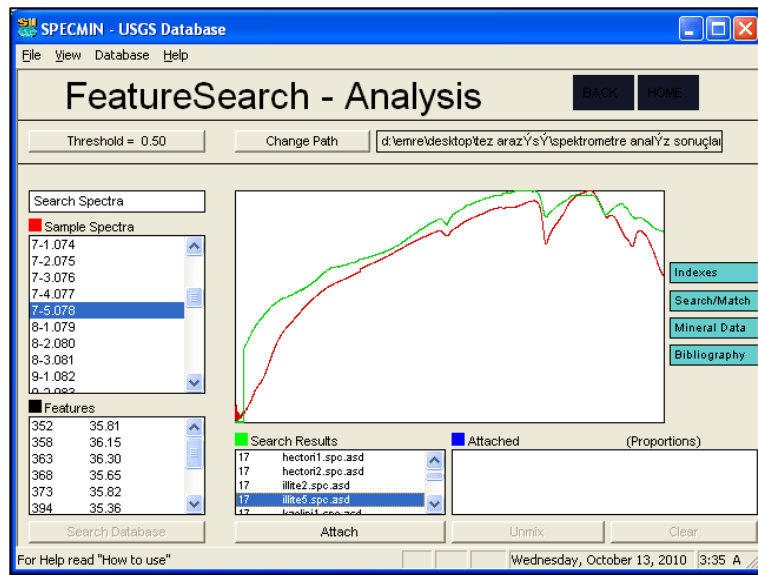


Figure A.7. Illite with seventh sample.

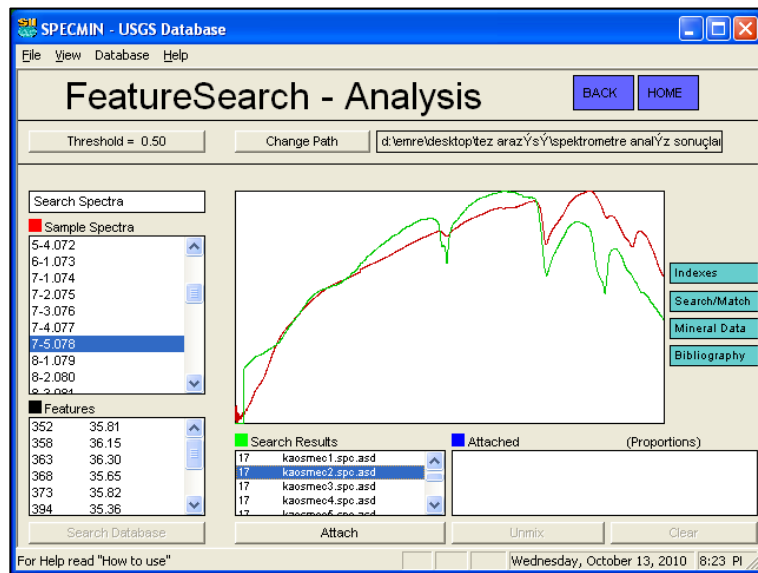


Figure A.8. Kaosmectite is another outcome offered by USGS library.

## APPENDIX B



**Figure B.1.** Sample taken from the close vicinity of 1<sup>st</sup> ground control point.



**Figure B.2.** Sample taken from the 1<sup>st</sup> ground control point.



**Figure B.3.** Sample taken from the 2<sup>nd</sup> ground control point.



**Figure B.4.** Sample taken from the 3<sup>rd</sup> ground control point.



**Figure B.5.** Sample taken from the 4<sup>th</sup> ground control point.



**Figure B.6.** Sample taken from the close vicinity of 4<sup>th</sup> ground control point.



**Figure B.7.** Another sample taken from the close vicinity of 4<sup>th</sup> ground control point.



**Figure B.8.** Additional sample taken from the close vicinity of 4<sup>th</sup> ground control point.



**Figure B.9.** Sample from Bozova Formation with a fossil shell.



**Figure B.10.** Hydrocarbon microseepage sample taken from the study area.



**Figure B.11.** Hydrocarbon microseepage sample with two non-anomalous samples on the right.



**Figure B.12.** Hydrocarbon microseepage and red bed sample



**Figure B.13.**Sample taken from red beds.



**Figure B.14.**Desert varnish sample (black portion).



**Figure B.15.** Sample taken from the east side of reference valley, inside the non-anomalous portions.



**Figure B.16.** Another sample with high clay concentration from the east part of reference valley.



**Figure B.17.** A fossiliferous marl from non-anomalous side of Bozova Formation.

## APPENDIX C

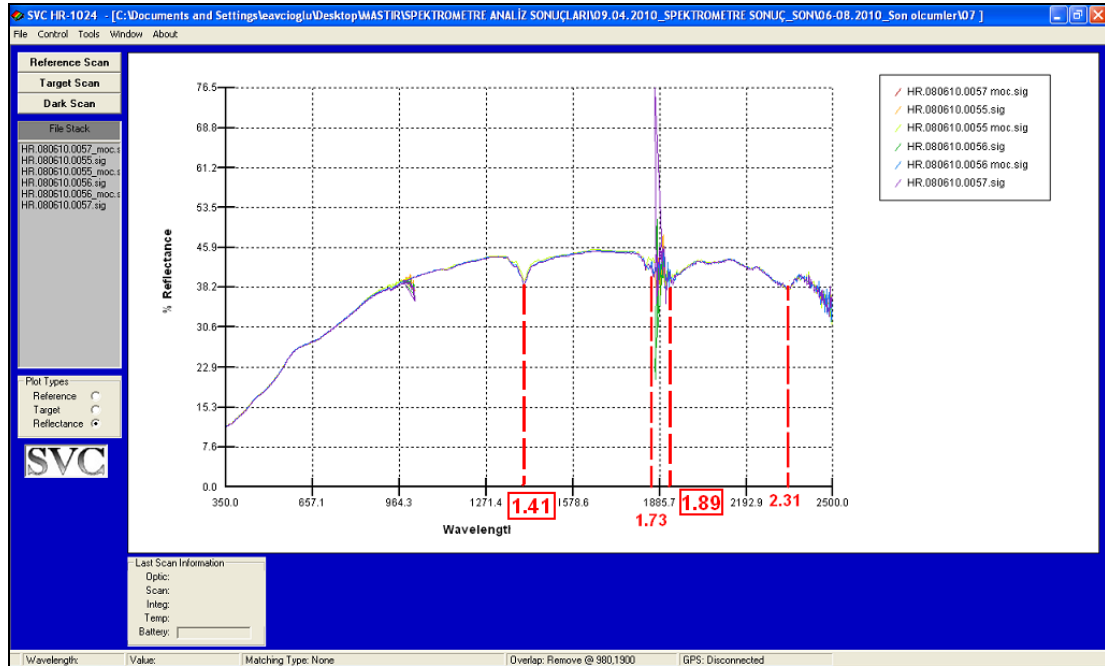


**Figure C.1.** Hydrocarbon spectral measurement with SVC Spectrometer. HC microseepages have distinct absorption values at 1.41 $\mu\text{m}$  and 1.89 $\mu\text{m}$  additionally to that 1.73 $\mu\text{m}$  and 2.31 $\mu\text{m}$  as stated in literature.